

12-2017

Modeling and Simulation of III-Nitride-Based Solar Cells using Nextnano®

Malak Refaei
University of Arkansas, Fayetteville

Follow this and additional works at: <https://scholarworks.uark.edu/etd>



Part of the [Electromagnetics and Photonics Commons](#), and the [Semiconductor and Optical Materials Commons](#)

Citation

Refaei, M. (2017). Modeling and Simulation of III-Nitride-Based Solar Cells using Nextnano®. *Graduate Theses and Dissertations* Retrieved from <https://scholarworks.uark.edu/etd/2616>

This Thesis is brought to you for free and open access by ScholarWorks@UARK. It has been accepted for inclusion in Graduate Theses and Dissertations by an authorized administrator of ScholarWorks@UARK. For more information, please contact scholar@uark.edu, uarepos@uark.edu.

Modeling and Simulation of III-Nitride-Based Solar Cells using Nextnano®

A thesis submitted in partial fulfillment
of the requirements for the degree of
Master of Science in Microelectronics-Photonics

by

Malak Refaei
Jazan University
Bachelor of Science in Physics, 2011

December 2017
University of Arkansas

This thesis is approved for recommendation to the Graduate Council.

Dr. Morgan Ware
Thesis Director

Dr. Hugh Churchill
Committee Member

Dr. Zhong Chen
Committee Member

Dr. Rick Wise
Ex-Officio Member

The following signatories attest that all software used in this thesis was legally licensed for use by Malak Refaei for research purposes and publication.

Mrs. Malak Refaei, Student

Dr. Morgan Ware, Thesis Director

This thesis was submitted to <http://www.turnitin.com> for plagiarism review by the TurnItIn company's software. The signatories have examined the report on this thesis that was returned by TurnItIn and attest that, in their opinion, the items highlighted by the software are incidental to common usage and are not plagiarized material.

Dr. Rick Wise, Program Director

Dr. Morgan Ware, Thesis Director

Abstract

Nextnano³ software is a well-known package for simulating semiconductor band-structures at the nanoscale and predicting the general electronic structure. In this work, it is further demonstrated as a viable tool for the simulation of III-nitride solar cells. In order to prove this feasibility, the generally accepted solar cell simulation package, PC1D, was chosen for comparison. To critique the results from both PC1D and Nextnano³, the fundamental drift-diffusion equations were used to calculate the performance of a simple p-n homojunction solar cell device analytically. Silicon was picked as the material for this comparison between the outputs of the two simulators as well as the results of the drift-diffusion equations because it is a well-known material in both software tools. After substantiating the capabilities of Nextnano³ for the simulation solar cells, an InGaN single-junction solar cell was simulated. The effects of various indium compositions and device structures on the performance of this InGaN p-n homojunction solar cell was then investigated using Nextnano³ as a simulation tool. For single-junction devices with varying bandgap, an In_{0.6}Ga_{0.4}N device with a bandgap of 1.44 eV was found to be the optimum. The results of this research demonstrate that the Nextnano³ software can be used to usefully simulate solar cells in general, and III-nitride solar cells specifically, for future study of nanoscale structured devices.

Acknowledgements

Firstly, I would like to thank “Allah Almighty” for giving me the strength, patience, and the ability to undertake this research and complete it successfully. This research would not have been achieved without his blessings.

I would like to express my sincere gratefulness and thankfulness to my research’s advisor Dr. Morgan Ware for providing his support, motivation, and guidance at all times throughout this research. He has given me the freedom to explore my research, but at the same time, he has always been there to assist me whenever I was stuck and to guide me to not deviate from the primary goals of my research. He has taught me the way to take this study and to present my research clearly. It was such an honor to work under his supervising. Also, I would like to thank him for his support, friendship, empathy, encouragement, and a great sense of humor.

I would like to thank Dr. Stefan Birner for answering my questions about the Nextnano software. He was accommodating and patient with me. I am very thankful for the useful information and advises in order to understand the software.

I would like to thank Dr. Rick Wise, my academic advisor, for his guidance and encouragements. He was always there to answer our questions, to advise, and to support us whenever we needed. I am very thankful to him for spending time reading my thesis.

In my journey towards my master’s degree, I have faced many obstacles and difficulties, and I would not have complete this degree without the support of my husband, Mr. Mohammed Reefai. I am deeply thankful for his love, friendship, support, encouragement, motivation, understanding, and prayers. I would also like to thank my children, Yazan and Abdulmajeed, for their patience and understanding when I could not be there with them to support them. I am very thankful to my parents, Amena and Ibrahim, for their love, support, motivation, prayers, caring

and preparing me to be successful in my life. Also, I express my thanks to my sister, Amwag, and my brothers.

Dedication

I dedicate this thesis to my husband Mohammed Reefai whose support made it possible for me to complete this degree. His friendship and love made my journey here remarkable and memorable. Also, I dedicate this thesis to my children, Yazan and Abdulmajeed. To my dear parents, Amena and Ibrahim, who encouraged me to pursue my education and prepared me to be successful in my life. Furthermore, to my sister, Amwag, and my brothers for the love, support, prayers, and encouragement.

Table of Contents

Chapter 1: Introduction	1
1.1 Harnessing Solar Energy	1
1.2 Economic Viability of High Efficiency	2
1.3 Motivation & Objectives	4
1.4 Organization of Thesis	5
Chapter 2: III-Nitride Materials for Photovoltaics.....	6
2.1 Basic Principles of Solar Cells	6
2.1.1 Solar Spectrum	6
2.1.2 p-n Junction	8
2.1.3 Operation of Solar Cells.....	12
2.1.4 Solar Cell Characteristics	14
2.1.5 Factors Limiting Conversion Efficiency in Photovoltaics	17
2.1.6 Strategies for Improving Efficiency in Photovoltaics	20
2.1.6.1 Tandem Solar Cells.....	20
2.1.6.2 Quantum Well Solar Cells	21
2.2 III-Nitride Materials System	22
2.2.1 Challenges in III-Nitride-Based Solar Cells	25
2.2.1.1 Lattice Mismatch	25
2.2.1.2 Phase Separation	26

2.2.1.3 P-type Doping and Ohmic Contacts	27
2.3 Conclusion.....	29
Chapter 3: Novel Method to Simulate III-Nitride Based Solar Cells	30
3.1 Introduction	30
3.2 Solving the Software Equations	31
3.2.1 Poisson Equation.....	31
3.2.2 Drift-Diffusion Current Equation and Continuity Equation	32
3.4 Program Flow	35
3.5 The Parameters of Nextnano ³	36
3.6 Conclusion.....	44
Chapter 4: Comparative study of Single-Junction Silicon Solar Cells within Nextnano ³ and PC1D.....	45
4.1 Introduction	45
4.2 PC1D Simulation Tool	45
4.2.1 Operation of PC1D.....	45
4.3 Differences Between Nextnano ³ and PC1D.....	47
4.4 Simulation of Single-Junction Silicon Solar Cells in Both Simulation Tools	50
4.4.1 Silicon Solar Cell Structure.....	50
4.4.2 Input Parameter	50
4.4.2.1 Optical Parameters in Nextnano ³ and PC1D	50
4.4.2.2 Electrical Parameters in Nextnano ³ and PC1D.....	54

4.4.3 Calculation of Si Solar Cell.....	54
4.4.4 Results	57
Chapter 5: Simulating III-Nitride Based Solar Cell within Nextnano ³	62
5.1 Structure.....	63
5.2 Input Parameters	63
5.3 Simulating Single-Junction In _x Ga _{1-x} N Solar Cells with Various Indium Contents	66
5.4 Simulating In _{0.5} Ga _{0.5} N Single-Junction Solar Cells.....	70
5.5 Simulating In _{0.6} Ga _{0.4} N Single-Junction Solar Cells.....	72
5.5.1 The effect of different thickness of each layer	73
5.5.2 The effect of different doping concentration of each layer	78
5.5.3 Using optimal thickness with different doping.....	81
5.6 Simulating In _{0.6} Ga _{0.4} N p-i-n Solar Cells.....	84
5.6.1 The effect of varying the thickness of i-region.....	85
5.6.2 The effect of varying the thickness of n-layer	88
5.6.3 The effect of varying the thickness of p-layer	88
5.6.4 The effect of varying the doping concentration of p-layer	90
5.6.5 The effect of varying doping concentration of n-layer	91
Chapter 6: Conclusions and Future Work.....	95
References.....	97
Appendix A: Nextnano ³ Input	102

Appendix B: Description of Research for Popular Publication	110
Appendix C: Executive Summary of Newly Created Intellectual Property	112
Appendix D: Potential Patent and Commercialization Aspects of listed Intellectual Property Items.....	113
Appendix E: Broader Impact of Research	114
Appendix F: Microsoft Project for MS MicroEP Degree Plan.....	115
Appendix G: Identification of All Software Used in Research and Thesis Generation	118

List of Figures

Figure 1: Efficiency as a function of cost for PV generations.....	3
Figure 2: Spectral irradiance for AM0, AM1.5G, and AM1.5D vs. wavelength	8
Figure 3: p-n junction before and after connection.....	9
Figure 4: Example of a) a homojunction structure, and b) a heterojunction structure under forward bias, respectively	12
Figure 5: Operation of solar cells.....	13
Figure 6: I-V curves under illumination and in the dark for an “InGaN/GaN p-i-n solar cell”	15
Figure 7: Maximum quantum efficiency curve of a silicon solar cell and the EQE effective mechanisms.....	17
Figure 8: Factors limiting solar efficiency: non-absorption of low-energy photons, thermalization mechanism, and recombination loss	18
Figure 9: Other factors limiting efficiency: (1) reflected some of the incident light, (2) shadowing losses, and (3) finite thickness of the absorber layer.....	19
Figure 10: Concept of multi-junction solar cells	21
Figure 11: Band diagram and structure of GaN/InGaN quantum-well solar cell.....	22
Figure 12: Bandgap of the InGaN materials	24
Figure 13: The most common metals used to achieve ohmic-contacts to p-type InGaN	28
Figure 14: Program flow scheme of Nextnano ³ software	35
Figure 15: Nextnano ³ command groups and primary keywords for solar cell devices.	37
Figure 16: Nextnano ³ window showing the 1D band-edges of a double heterostructure InGaN/GaN solar cell: gamma band-edges (red), heavy-hole (brown), light-hole (orange), the electron Fermi level (light green hidden under light blue), and the hole Fermi level (light blue).	43
Figure 17: An example of the operation interface of the PC1D software.	46

Figure 18: Finite element discretization	48
Figure 19: Finite difference discretization.....	49
Figure 20: Silicon solar cell structure.....	50
Figure 21: The used solar spectrum for AM1.5G.....	52
Figure 22: Absorption coefficient of silicon.....	52
Figure 23: The real and imaginary part of Si refractive index vs. wavelength.....	53
Figure 24: The computed reflectivity for silicon.....	53
Figure 25: Comparison of I-V curves for Si solar cells.....	58
Figure 26: Fixed parameters in Si solar cell structure varying the p-type thickness.....	59
Figure 27: Output I-V curves for different thickness of p-type emitter using PC1D.....	60
Figure 28: Output I-V curves for different thickness of p-type emitter using Nextnano ³	61
Figure 29: In _x Ga _{1-x} N solar cell structure.....	63
Figure 30: In _x Ga _{1-x} N absorption coefficient for various indium content.....	65
Figure 31: (a) Energy band diagrams, and (b) IQE of In _x Ga _{1-x} N single-junction solar cells for various indium compositions.....	67
Figure 32: J-V characteristics of In _x Ga _{1-x} N single-junction solar cells for different indium compositions.....	67
Figure 33: Efficiency versus indium content in the In _x Ga _{1-x} N single-junction solar cells.....	69
Figure 34: J-V characteristic of In _x Ga _{1-x} N single-junction solar cells with and without strain... ..	70
Figure 35: The reference In _{0.6} Ga _{0.4} N single-junction structure.....	71
Figure 36: (a) Energy band diagrams, (b) J-V characteristics, and (c) efficiency as a function of p-type thickness.....	72

Figure 37: In _{0.6} Ga _{0.4} N single-junction structure.	73
Figure 38: (a) Energy band diagrams, and (b) IQE of In _{0.6} Ga _{0.4} N single-junction solar cells for various p-type thicknesses.....	74
Figure 39: Output J-V characteristics of In _{0.6} Ga _{0.4} N single-junction solar cells with various p-type thickness.....	75
Figure 40: (a) Energy band diagrams, and (b) IQE of In _{0.6} Ga _{0.4} N single-junction solar cells for various n-type thicknesses.....	76
Figure 41: J-V characteristics for different n-type thicknesses of In _{0.6} Ga _{0.4} N single-junction solar cells.	77
Figure 42: Efficiency as a function of thickness for different n- and p-type thicknesses of In _{0.6} Ga _{0.4} N single-junction solar cells.....	77
Figure 43: Energy band diagrams of In _{0.6} Ga _{0.4} N single-junction solar cells for different p-type doping levels.	79
Figure 44: J-V characteristics of In _{0.6} Ga _{0.4} N single-junction solar cells with several p-doping levels.	79
Figure 45: Energy band diagrams of In _{0.6} Ga _{0.4} N single-junction solar cells for several n-doping levels.....	80
Figure 46: J-V characteristics for several levels of n-type doping of the In _{0.6} Ga _{0.4} N solar cells. 81	
Figure 47: Efficiency as a function of doping concentrations for several p- and n-type doping of the In _{0.6} Ga _{0.4} N solar cells.....	82
Figure 48: (a) Energy band diagrams, (b) J-V characteristics, and (c) efficiency as a function of doping concentrations using optimal thickness.	83
Figure 49: Efficiency as a function of thickness and doping concentration of single-junction In _{0.6} Ga _{0.4} N solar cells.....	84
Figure 50: Structure of the In _{0.6} Ga _{0.4} N p-i-n homojunction solar cell.....	85
Figure 51: (a) Band diagrams and (b) IQE for different i-layer thickness in the p-i-n structure..	86
Figure 52: J-V characteristics for varied i-layer thickness in p-i-n solar cells.	87

Figure 53: Efficiency of p-i-n solar cells as a function of i-layer thickness.	87
Figure 54: (a) Energy band diagrams, (b) IQE, (c) J-V curves, and (d) the efficiency vs. n-type thickness for p-i-n solar cells using different n-type thickness.	89
Figure 55: (a) Energy band diagram, (b) IQE, (c) J-V curves, and (d) the efficiency vs. different p-type thickness for p-i-n solar cells.	90
Figure 56: (a) Energy band diagrams, (b) IQE, (c) J-V curves, and (d) the efficiency vs. p-type doping for p-i-n solar cells.	92
Figure 57: (a) Energy band diagrams, (b) IQE, (c) J-V curves, and (d) the efficiency vs. n-type doping for p-i-n solar cells.	93
Figure 58: Efficiency versus thickness and doping concentration for p-i-n solar cells.	94
Figure 59: Optimal structure for p-i-n homojunction solar cells.	94

List of Tables

Table 1: Bandgap values, maximum theoretical efficiency, and reachable efficiencies of 3-8 junctions tandem solar cells under 500 suns and black-body radiation at 6000 K.	23
Table 2: Lattice Mismatch and thermal Mismatch of GaN with different substrates.....	26
Table 3: Some differences and similarities between finite difference method and finite element method.....	49
Table 4: Electrical parameters for silicon.	54
Table 5: Si solar cell simulation results.	57
Table 6: The composition dependent parameters used to calculate the $\text{In}_x\text{Ga}_{1-x}\text{N}$ absorption coefficient of the $\text{In}_x\text{Ga}_{1-x}\text{N}$ alloys	64

Chapter 1: Introduction

Climate change has become a substantial phenomenon which has defined the 21st century. During the previous decade, the earth has experienced significant melting of glaciers and so-called permanent polar ice, leading to increases in sea level due to global warming. Climate researchers suggested that extensive exploitation of fossil fuels are the primary causes of global warming through generating high intensities of greenhouse gases [1]. Fossil fuels are a limited resource; however, consumption has increased due to human demand of energy. With the increasing demand for energy along with the global warming, it is now of great interest to use renewable and sustainable sources of energy.

1.1 Harnessing Solar Energy

Sunlight is an efficient energy source compared to other energy resources [2]. In fact, the amount of solar power reaching the atmosphere is around 1.7×10^{17} watts, which is considerably more than is required to satisfy all of the energy consumed by humans annually [3]. The sun is not only ultimately the primary source of all energy, but also universally accessible, fundamentally unlimited (on our timescale), and environmentally safe. The sun not only provides power for natural processes, including heating, photosynthesis, as well as the formation of fossil fuels but also can be harnessed and converted into electricity by using photovoltaic systems.

These photovoltaic systems directly generate electricity from sunlight. They are extremely dependable, very safe, simple to install, and function at low-cost. Photovoltaic systems are capable of being grid-connected, modular, as well as stand-alone. At the heart of these systems, solar energy is converted into electricity by semiconductor-based solar cells, the use of which has negligible negative impact on the environment.

1.2 Economic Viability of High Efficiency

The solar cell global market is beyond 18 billion dollars per year, and the solar industry is expanding at higher than 30 percent annually [4][5]. However, despite the steady development of this market, only about 10 Giga-Watts Peak (GWP) is produced from the entire PV installed capacity globally, which is merely 0.05 percent of the global power usage [6]. Even though existing solar cells cost around \$0.20/kWh to operate in the United States [4] without any subsidies, fossil-based competitors are still four times cheaper. When comparing solar cell price to other energy sources, the main causes of cost inflation are the high installation and manufacturing costs. Nevertheless, some challenges, including system integration, reliability, and storage, are frequently being addressed.

Since the first silicon solar cell, efficiency and cost are the two main objects of improvement. Based on these objects, solar cell devices are divided into different general generations: a first-generation, a second-generation, and a third-generation. The first-generation had the most studied and well-characterized solar cells. It was the most common technology typically used for solar cells, and this generation focused on silicon solar cells. Silicon solar cells are stable, cheap, well-developed, and well-commercialized. The maximum efficiency reported recently for single-junction silicon solar cells is around 26.7% [7]. The second-generation focused on thin-film solar cells. The concept of the second-generation relies on using fewer materials to reduce the cost. However, this generation has a lower theoretical efficiency limit than the first one [8]. It was suggested that increasing solar cell efficiency while maintaining reasonable costs would achieve the target of reducing the overall price per watt to compete economically with other energy sources [9]. Those goals led to the concept of advanced third-generation solar cells, which would be more efficient than the first-generation while having comparable costs to that of second-

generation cells. The third-generation could potentially come well under the US \$1/W objective, which is equivalent to the cost of conventional energy [10] (Figure 1).

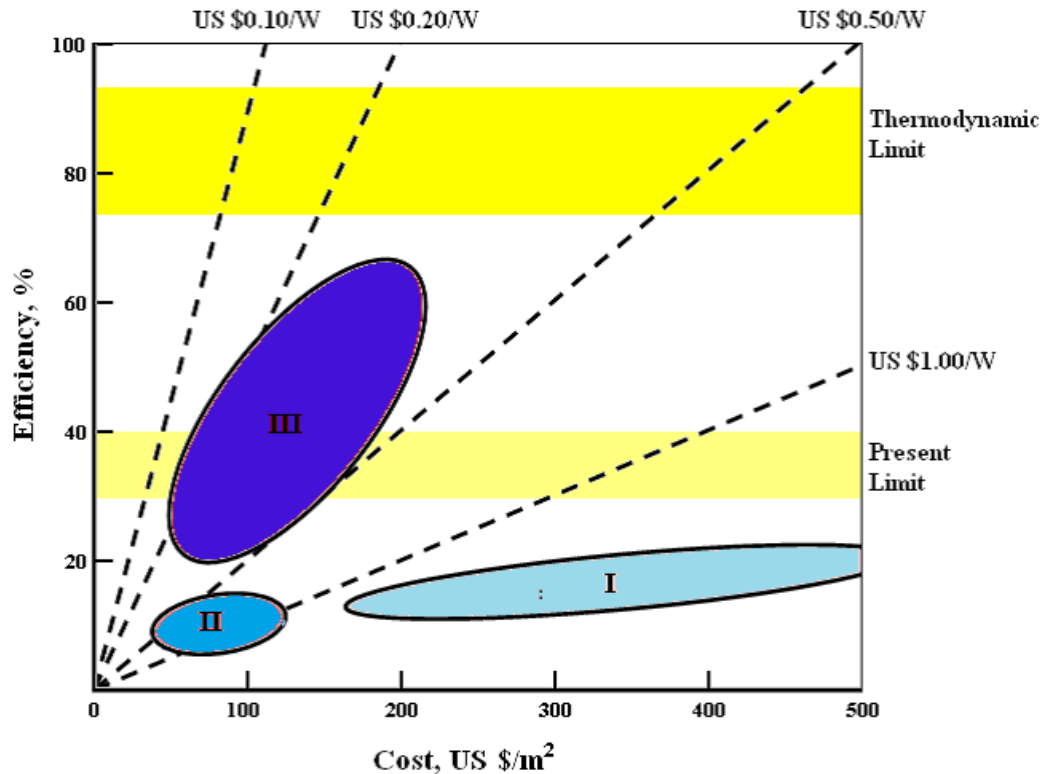


Figure 1: Efficiency as a function of cost for PV generations [10].

The third-generation of solar cells are an emerging technology, which has dominated recent PV research. One example of third-generation solar cells is the tandem solar, which contains of a different material with various bandgaps making up effectively different cells placed on top of one another in order to efficiently absorb multiple wavelength ranges of light. The current triple-junction tandem solar cells can reach up to 42.4% efficiency, which is the highest efficiency currently recorded [11]. Other high-efficiency solar cells, for example, are multiple quantum well solar cells, thermoelectric-based solar cells, and intermediate band solar cells. However, solar cells have yet to achieve an efficiency that exceeds 50%. Theoretical investigations should

explore novel designs of III-nitride semiconductor-based solar cells in order to produce very high-efficiencies [12][13].

1.3 Motivation & Objectives

The use of simulation programs has increased greatly in order to understand the behavior and operation of materials and systems without having to fabricate a device. Reducing the cost and development time have become a general requirement to design and investigate solar cell devices out of the vast selection of materials and structures. Solar cell simulation programs assist in general to study the optical and electronic behavior and to explore the impact of different parameters on solar cell performance. Nextnano³ [14] is a simulation tool which has been established for semiconductor nanodevices with a heavy emphasis on the quantum effects resulting from confinement at the nanoscale.

The primary objective of this research was to use the Nextnano³ software to simulate III-nitride based solar cells. However, even though it is a native application of the software, this has not been widely attempted. Therefore, PC1D software [15] (a well-established Si solar cell simulator) was chosen as a comparison to validate that Nextnano³ can be successfully applied to solar cell devices. To critique the outcomes of both PC1D and Nextnano³, fundamental drift-diffusion equations were used to calculate the performance of the simple, solar cell test device analytically. Silicon is a well-studied material for photovoltaic devices. Thus, it was selected as the material for the comparison between the outputs of the two simulators as well as the drift-diffusion equations.

After substantiating the capabilities of Nextnano³ for the simulation solar cells, the primary objective of simulating III-nitride solar cells broke down into three goals. The first one was to investigate the effects of various indium compositions and device structures on the performance

of this InGaN p-n homojunction solar cell using Nextnano³ as a simulation tool. The second minor objective was to use the optimal bandgap to simulate InGaN single-junction devices. Simulating p-i-n InGaN homojunction solar cells was the final goal of this work.

1.4 Organization of Thesis

The organization of this thesis breaks down into six chapters. Chapter 1 has been a brief introduction of solar cell devices in general and the motivation of this work. Chapter 2 describes the theoretical background behind the fundamental principles of solar cell devices as well as a brief introduction to the III-nitride material system including its advantage and challenges. Chapter 3 presents an overview of Nextnano³ software as a method used to simulate III-nitride solar cells and the basic semiconductor equations: drift-diffusion current equation, Poisson's equation, and continuity equation. Chapter 4 includes a brief introduction of PC1D software, the differences between Nextnano³ and PC1D, and finally, a comparative study of single-junction silicon solar cells as simulated with Nextnano³ and PC1D simulators, as well as the drift-diffusion equations. Simulation results of III-nitride based solar cells are reviewed in Chapter 5. The final chapter states the conclusion of this research and the recommended future work.

Chapter 2: III-Nitride Materials for Photovoltaics

This thesis investigates a novel method to simulate indium gallium nitride-based solar cells. Before examining the simulation, this chapter covers the essential principles of solar cell devices including the solar spectrum, p-n junctions, the operation of solar cells, factors limiting conversion efficiency, and strategies used to improve solar cell efficiency. Then, a brief introduction to the III-nitride material system including its advantages and challenges are generally discussed.

2.1 Basic Principles of Solar Cells

The most significant fundamental process of solar cells is called the “photovoltaic effect,” which is literally the generation of the voltage under exposure to light. Becquerel first discovered this effect in 1839 [16]. In 1954, Chapin, Fuller, and Pears created the first silicon solar cell with 6% efficiency, which was the beginning of the p-n junction solar cell [16].

2.1.1 Solar Spectrum

The output power of a solar cell device derives directly from sunlight, which is a part of the electromagnetic energy afforded by the sun. Sunlight is created out of energetic particles identified as photons. Each photon has an energy different from other photons based on its wavelength. The photon energy can be found by

$$E = \frac{hc}{\lambda} \quad (\text{Equation 2-1})$$

where hc is the Planck constant and the speed of light, respectively, and λ is wavelength of light. The amount of energy from the Sun is characterized by its energy or wavelength spectrum which is incident on the Earth. This spectrum or more specifically the solar spectrum power density in space and at the Earth’s surface resembles the emission spectrum of a black-body at 5500 K[17]. By considering the Sun-Earth distance and all available wavelengths, the total solar power

density at the Earth's atmosphere is about 1353 W/m². The total power density available at the surface is reduced by reflection, scattering, and absorption of the light energy by gases in the atmosphere.

In order to quantify and standardize the variation of the intensity of the solar spectrum passing through the atmosphere and then absorbed by air, one uses the unit of Air Mass (AM). It is the ratio between the path distance of solar radiation across the atmosphere (l) to the minimum possible path length (l_0), i.e., the equivalent optical path length of a light ray hitting the atmosphere at normal incidence. AM can be calculated by:

$$AM = \frac{l}{l_0} = \frac{1}{\cos(\theta)} \quad (\text{Equation 2-2})$$

where θ is a zenith angle of the sun. Since the angle of the sun affects the AM, the AM will change with the time of day, the season, weather, and latitude. The solar spectrum in space before interaction with the atmosphere is known as (AM0). This air mass is normally utilized in space-based solar applications, such as solar cells, used to power satellites. The most common air mass used for solar cells on the earth's surface is (AM1.5), which corresponds to 48.2° zenith angle, and it serves as the standard AM by which to distinguish between various solar cells. The total power density of the AM1.5 distribution is 1 kW/m² [18], which is also known as one sun.

The sunlight reaching the earth's surface can be direct light or diffuse light, scattered by the atmosphere. The air mass notation indicating these two components of light is, for example, AM1.5G, where G is defined as a "Global," which contains both diffuse as well as direct, and AM1.5D, where D stands for "Direct," which is only the direct light component. The AM1.5G spectrum is defined as a standard average air mass for ground-based solar cells. The spectral irradiance for AM0, AM1.5G, and AM1.5D versus wavelength is presented in Figure 2 [19]

where the noticeable drops in irradiance between the AM0 and the AM1.5 spectra are due to specific gas absorption bands.

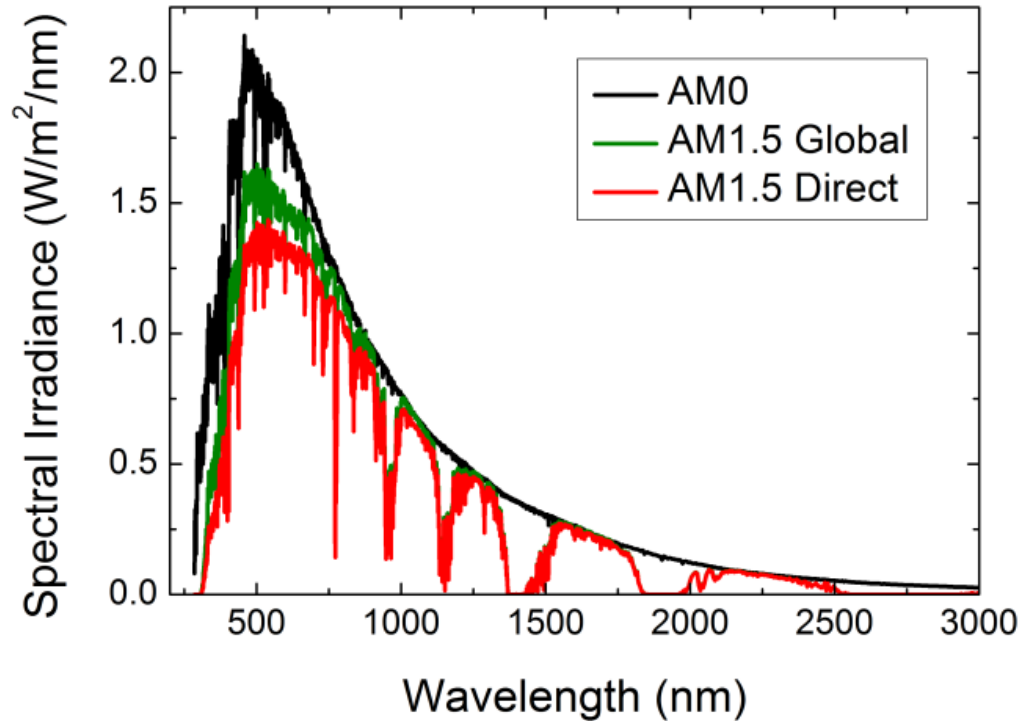


Figure 2: Spectral irradiance for AM0, AM1.5G, and AM1.5D vs. wavelength [19].

2.1.2 p-n Junction

The most common solar cells used are created out of a p-n junction, which connects two materials based on semiconductor with opposite doping types, as presented in Figure 3 [20]. The conductivity of the semiconductor materials varies by doping, where doping generally is a technique used to change the concentration of mobile electrons or holes in a semiconductor. There are two types of semiconductor doping. When materials from group IV, Si for example, are doped with atoms from Group V with one extra electron, such as phosphorus, the conduction band will have higher concentration of free electrons than that of holes in the valence band.

Therefore, the Fermi level (E_F) will lie close to the conduction band to create an n-type semiconductor material. The conductivity of the n-type semiconductor material will increase due to the electron concentration available in the conduction band.

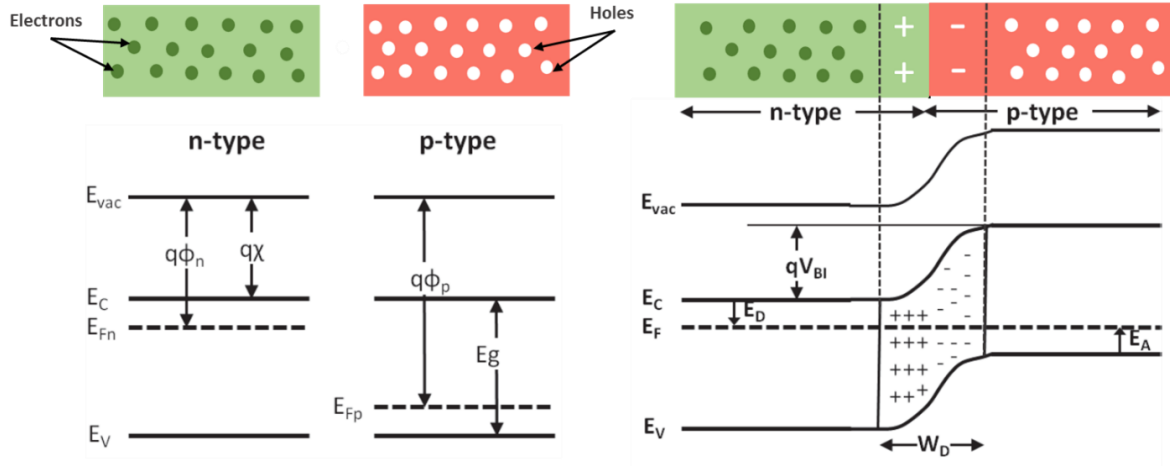


Figure 3: p-n junction before and after connection [20].

When doping a material from the group IV with atoms from Group III with one fewer electron, such as boron, the concentration of free holes in the valence band will be greater than the number of free electrons available in the conduction band. Thus, the Fermi level (E_F) will lie near the valence band to produce a p-type semiconductor material. The conductivity of the p-type semiconductor material will increase due to the number of holes available in the valence band. In reference to Figure 3 the energy between the Fermi level and the vacuum level, which is the energy needed for an electron to leave the surface of a semiconductor, is called the work function (ϕ_n), and the energy between the conduction band and the vacuum level is called the electron affinity (χ) [16].

When combining p-type with n-type semiconductor materials to form the p-n junction,

the Fermi levels become aligned due to the diffusion of majority carriers towards the interface. The diffusion of electrons leaves positively charged ions, and the diffusion of holes leaves negatively charged ions. The resulting negative and positive ions around the interface make up the “space charge region” or “depletion region” [16]. Therefore, a “built-in” electric field is generated in the space charge region due to these fixed charges, which has a direction pointing from the positively charged ions towards the negatively charged ions. This electric field leads to a “built-in” potential difference between the ends of the junction. The built-in potential is given by [16]:

$$V_{bi} = \frac{kT}{q} \ln \left(\frac{N_a N_d}{n_i^2} \right) \quad (\text{Equation 2-3})$$

where $\frac{kT}{q}$ is known as the thermal voltage, N_a and N_d are the ionized donor and acceptor densities, respectively, and n_i is the intrinsic carrier concentration.

Under the built-in electric field, the holes will drift from the n-region to the p-region, and electrons will drift from the p-region to the n-region, and this drift current has a reverse direction to the diffusion current. In thermal equilibrium condition, there must be no current flowing through the p-n junction, and the drift current and the diffusion current must have equal values [16].

The current in p-n junction can be forward and reverse currents. The forward current is defined as the diffusion of the majority carriers from one region of the junction to the other in order to overcome the built-in potential of the “depletion region.” The reverse current is known as the drift current because electric field sweeps minority carriers from one side to the other.

When applying a positive voltage to the p-region of the diode, the voltage barrier becomes small, resulting in increasing the number of carriers flowing across the junction. Therefore, rising

the forward bias voltage increases the diffusion current. In the case of reverse bias voltage, the voltage barrier rapidly increases, so a minimal number of carriers can flow from one side of the junction to the other, resulting in decreasing the diffusion current. The minority carriers affect the drift current, which can be defined by the generation rate inside a diffusion length of the p-n junction. The drift current is entirely unchanged by the electric field, and the diffusion lengths and the generation-rate can be used to evaluate the drift current. The drift current is not contingent on the voltage. The overall current can be found by the “ideal diode equation” [16]:

$$I_{tot} = I_f - I_r = I_s \exp\left(\frac{qV}{kT}\right) - I_s \quad (\text{Equation 2-4})$$

Here, I_s and V are the reverse saturation current and the applied voltage, respectively. At $V = 0$, the overall current is zero, and for increasing reverse bias voltage, the overall current will approach $-I_s$. Increasing the reverse saturation current or the drift current depends on increasing the generation rate of the minority carrier around the p-n junction. This is done optically in the case of solar cells.

There are two different types of p-n junctions regarding the utilized semiconductor materials. First, if the p- and n- region of the junction is created from the same semiconductor, this is called a homojunction. To illustrate, a homojunction forms when combining a p-type Si with an n-type Si. On the other hand, if the p- and n- sides of the junction are made from different semiconductors, generally with different bandgaps, this p-n junction is known as a heterojunction. The combination of several heterojunctions together is named a heterostructure. Through the heterostructure, the performance of solar cells is mainly enhanced by increasing the light absorption properties of the entire designed structure. The heterojunction is divided into two types: isotype and anisotype. The isotype heterojunction results from different materials with equivalent conductivity to reduce the carrier diffusion length [21]. The anisotype heterojunction

emerges from materials with different conductivities and large differences in bandgap energy to enhance the injection efficiency of the generated carriers [21]. An example of a homojunction structure and a heterojunction structure under forward bias appears in Figure 4.

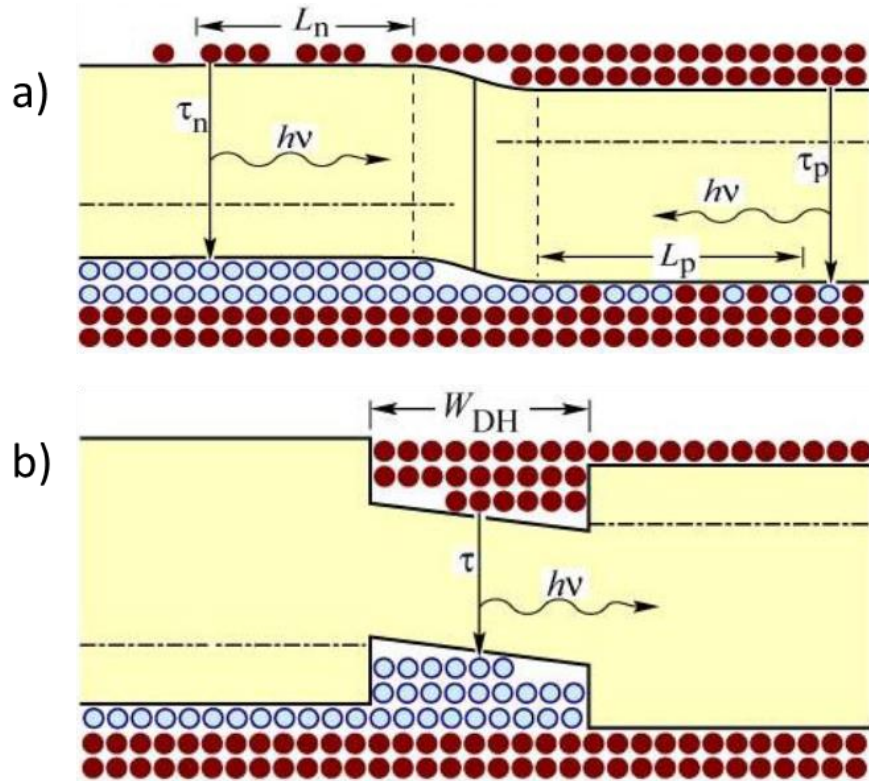


Figure 4: Example of a) a homojunction structure, and b) a heterojunction structure under forward bias, respectively [22].

2.1.3 Operation of Solar Cells

When shining light on a solar cell, some of the incident light is absorbed by the solar cell device. Only the photons with higher energy than the semiconductor bandgap are absorbed, and the absorbed photons from the solar spectrum transfer their energy to the electrons. Then, the electrons will have enough energy to be excited from the valence band into the conduction band, leading to the generation of electron-hole pairs. The built-in electric field separates those

electrons and holes in the depletion region. The electric field also drifts the electrons towards the n-region and the holes towards the p-region, generating the current which can reach the external circuit. The current and voltage together generate the power produced by the solar cells. The operation of solar cells is diagrammed in Figure 5.

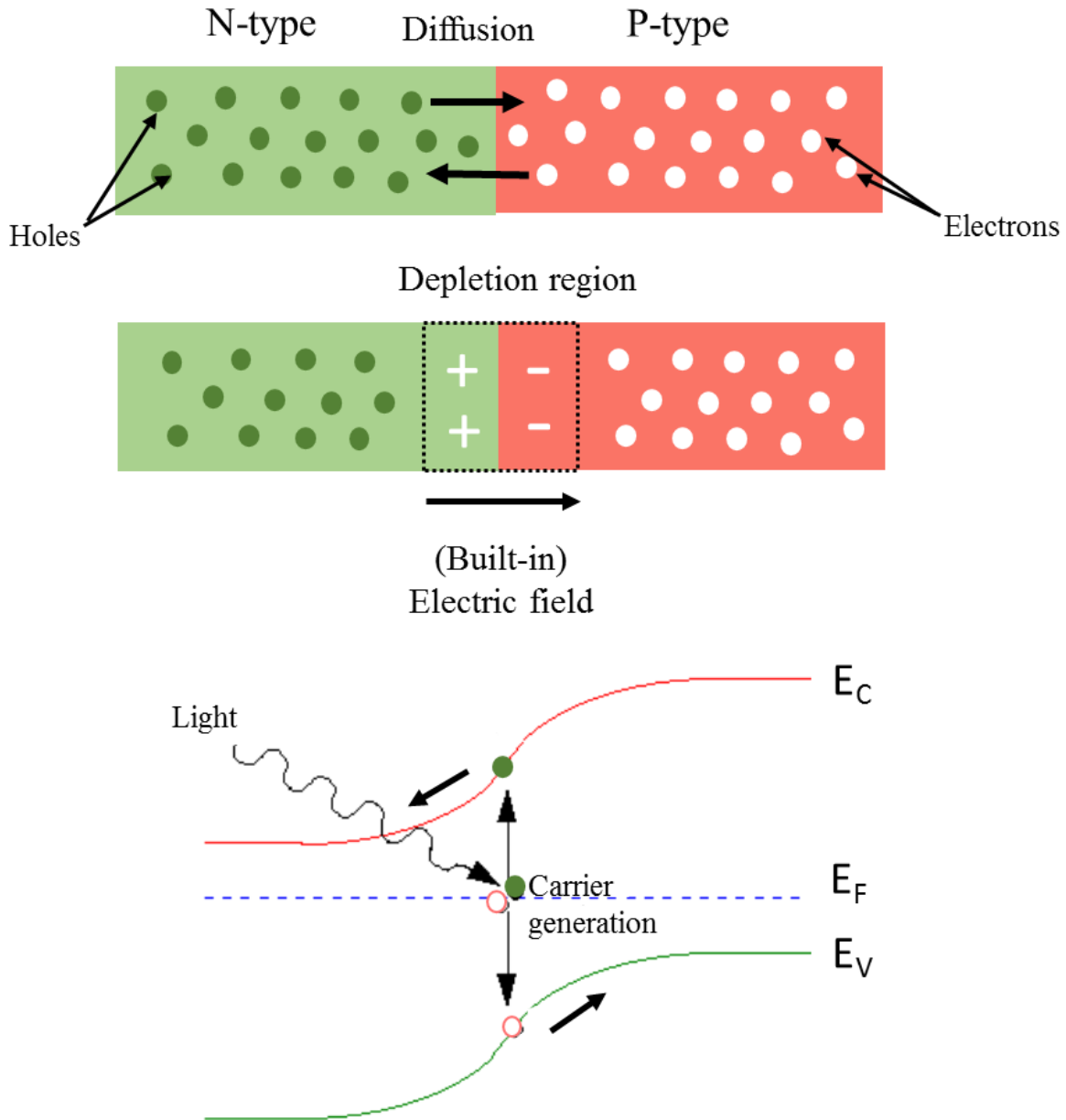


Figure 5: Operation of solar cells [17].

2.1.4 Solar Cell Characteristics

Under the effect of illumination, the photo-generated current (I_{op}) can be included in the diode equation, which becomes [16]:

$$I_{tot} = I_f - I_r = I_s \exp\left(\frac{qV}{kT}\right) - I_s - I_{op} \quad (\text{Equation 2-5})$$

Therefore, compared to the dark I-V curve, the “light” I-V curve will be shifted down by $-I_{op}$.

When the solar cell device is short circuited, at zero volts, the first term of the diode equation will be zero, and the overall current will equal to the photo-generated current (I_{op}), which is now defined as the short circuit current (I_{sc}), the highest photogenerated current that can flow through the solar cell. For the maximum voltage, the device is taken at open circuit and zero current. By then solving the diode equation for the voltage, the maximum voltage or the open circuit voltage (V_{oc}) of the solar cell is found to be [16]:

$$V_{oc} = \frac{kT}{q} \ln\left(\frac{I_{sc}}{I_s} + 1\right) \quad (\text{Equation 2-6})$$

Here, the open circuit voltage (V_{oc}) depends on I_{sc} and, therefore, the intensity of the illumination, as well as I_s and, therefore, the effective bandgap of the device. Ultimately, however, the V_{oc} cannot exceed the built-in potential of the p-n junction. To illustrate, I-V curves under illumination and in the dark for an “InGaN/GaN p-i-n solar cell” are presented in Figure 6 [23]. As mentioned, increasing the reverse saturation current (I_s) depends upon increasing the generation rate, which can be affected by the material’s bandgap [23].

When operating the solar cells, the output power can be found simply by [16]:

$$P = IV \quad (\text{Equation 2-7})$$

The highest point of a solar cell’s operation is called the maximum output power P_m , with effective voltage, V_m , and current, I_m . The fill factor, FF , is the given by the ratio of maximum

power produced by the solar cell device to the product of the short circuit current and the open circuit voltage, and it is graphically a measure of “squareness” of the I-V curve. It can be calculated by using [16]:

$$FF \equiv \frac{V_m I_m}{V_{oc} I_{sc}} = \frac{P_m}{V_{oc} I_{sc}} \quad (\text{Equation 2-8})$$

The ideal FF is 100%, but an approximation of the full I-V curve uses a smaller area. An optimal FF of the solar cell device corresponds to V_{oc} , without any effect of shunt and series resistances, and can be given by [24]:

$$FF_0 = v_{oc} - \frac{\ln(v_{oc} + 0.72)}{v_{oc} + 1} \quad (\text{Equation 2-9})$$

where FF_0 is the fill factor that is not dependent on resistances, v_{oc} is the normalized V_{oc} which can be found using $v_{oc} = \left(\frac{q}{nkT}\right) \times V_{oc}$, and where the n is the ideality factor of the device [24].

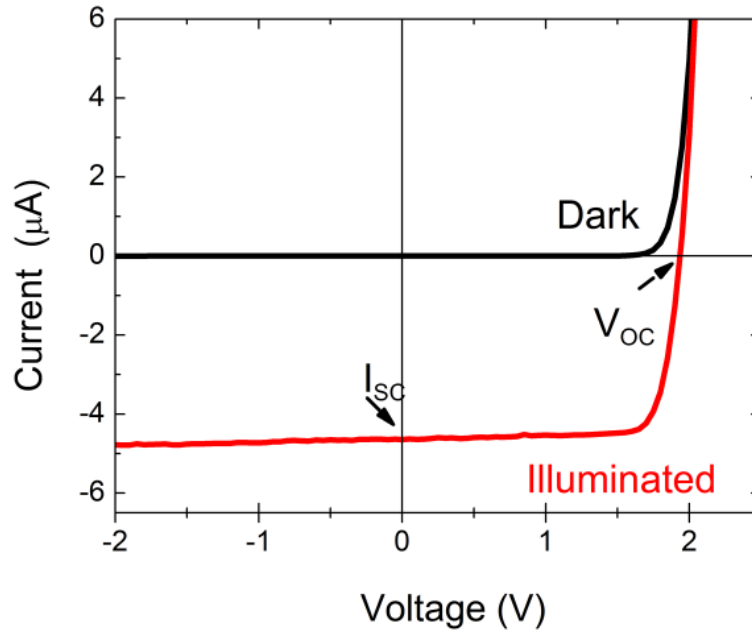


Figure 6: I-V curves under illumination and in the dark for an “InGaN/GaN p-i-n solar cell” [23].

Conversion efficiency is the most significant parameter by which to characterize solar cell performance. The effectiveness of solar cells is also characterized by internal quantum efficiency and external quantum efficiency. First, conversion efficiency (η) is the ratio of the highest output power (P_{out}) and the total incident light power (P_{in}) of sunlight, and it is affected by the intensity of the received light and the temperature. The standard conversion efficiency measurement was considered at 300 K and under one-sun illumination (100 mW/cm² intensity) or AM1.5G [16][18]. The conversion efficiency can be directly found using electrical parameters of the solar cell taken from the I-V curves, and it can be calculated by using:

$$\eta = \frac{P_m}{P_{in}} = \frac{V_m I_m}{P_{in}} = \frac{FF V_{oc} I_{sc}}{P_{in}} \quad (\text{Equation 2-10})$$

Another essential description of efficiency is the Internal Quantum Efficiency (IQE), which is the ratio of the amount of the absorbed photons to the collected electrons. Also, the External Quantum Efficiency (EQE) is the ratio of the number of accumulated electrons in the external circuit to the number of incident photons [17] and can be found by:

$$EQE \equiv \frac{(N_e/s)}{(N_{ph}/s)} \quad (\text{Equation 2-11})$$

where (N_e/s) is the number of collected electrons per second, and (N_{ph}/s) is the number of incident photons per second. The EQE is affected by the bandgap of the material because it measures the number of collected electrons, which is a result of the absorption of incident photons. Thus, the EQE will have zero value if the energy of photons is smaller than the material's bandgap [25]. The optimum quantum efficiency, which measures the sensitivity of a solar cell to the solar spectrum, has the square curve as presented in the Figure 7. In a typical silicon solar cell, the quantum efficiency is limited by recombination mechanisms,

reflection at the surface, and low absorption in the solar cell [26].

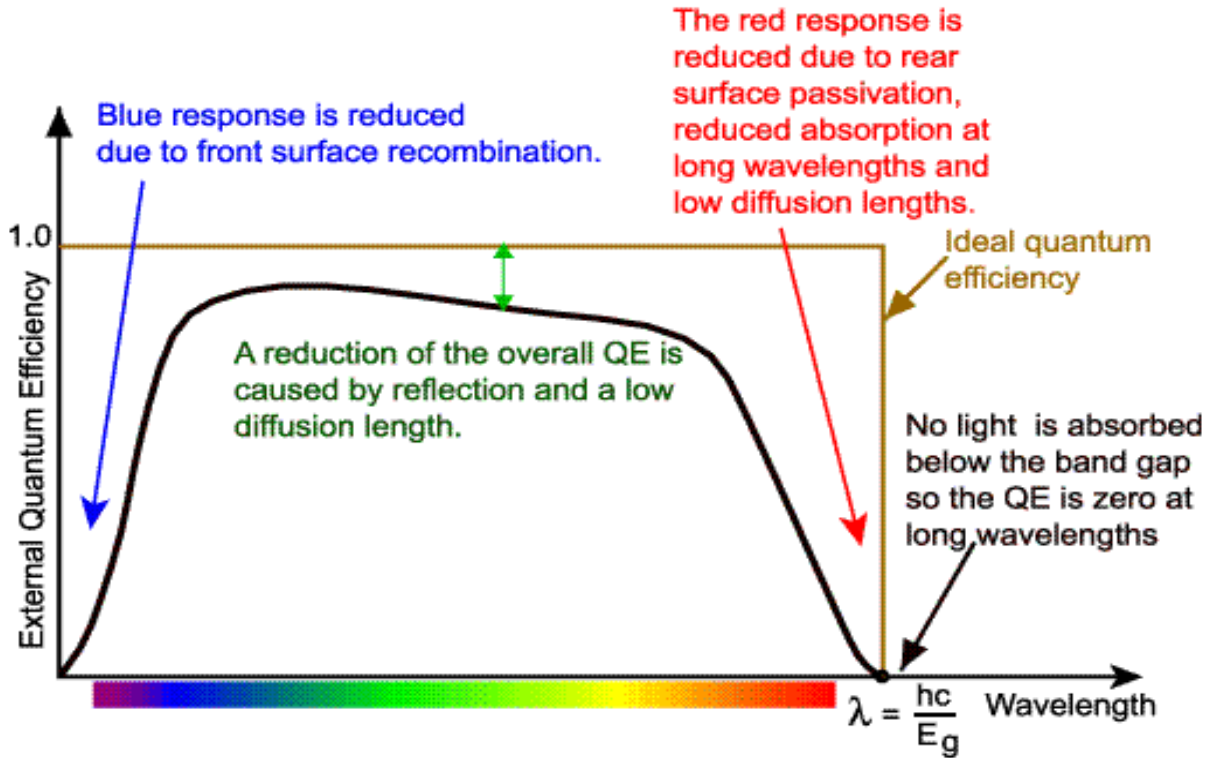


Figure 7: Maximum quantum efficiency curve of a silicon solar cell and the EQE effective mechanisms [26].

2.1.5 Factors Limiting Conversion Efficiency in Photovoltaics

The conversion efficiency of solar cells may decrease due to several factors, which will inhibit fabricated solar cells from achieving their theoretical maximum. The first factor limiting the efficiency is non-absorption of low-energy photons, as shown in Figure 8. If photons have lower energy than the semiconductor's bandgap, those photons are not absorbed by the solar cell device. Therefore, these photons cannot produce electron-hole pairs, which cuts down the solar efficiency [27].

Another limiting factor is thermalization. Photons with higher energy than the

semiconductor's bandgap can produce electron-hole pairs. Then, the electrons tend to occupy the lowest energy levels of the conduction band, and holes tend to occupy the highest energy levels of the valence band. However, electron-hole pairs receive more energy than needed from the photons, so this extra energy is released as heat (transferred to the semiconductor lattice). The energy loss process is called thermalization [27].

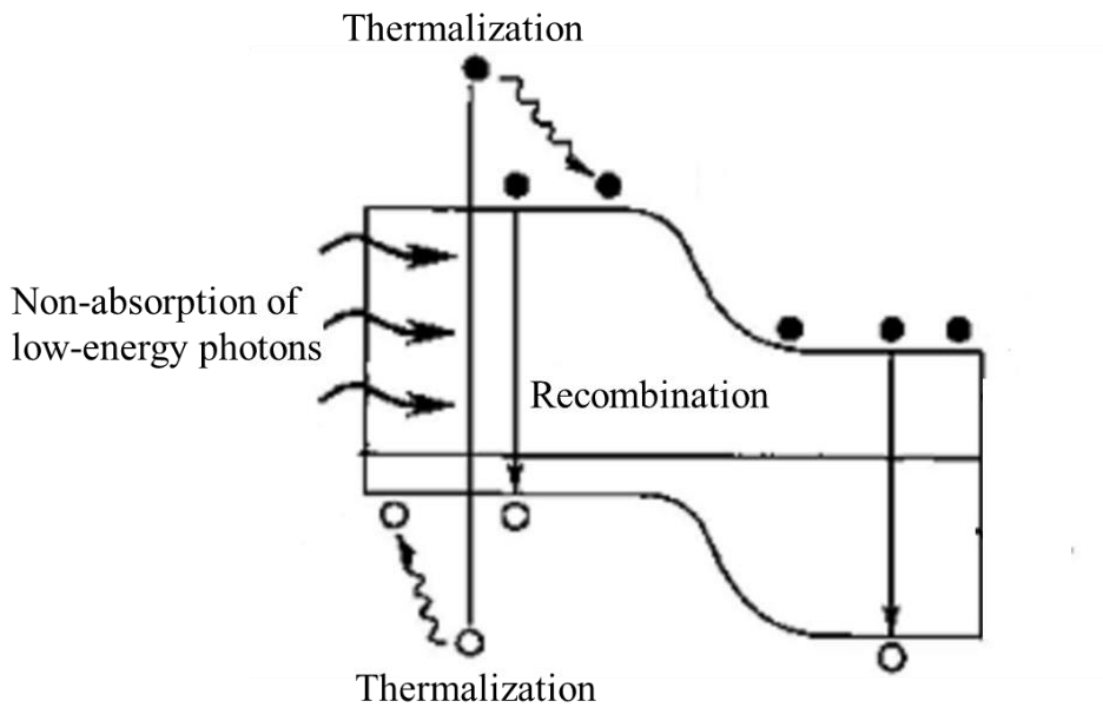


Figure 8: Factors limiting solar efficiency: non-absorption of low-energy photons, thermalization mechanism, and recombination loss [28].

Recombination loss is another factor that can affect solar efficiency. Since some of the photogenerated carriers in the solar cells are not collected and used in generating electricity, those carriers will recombine and, thus, waste their energy. This recombination mostly occurs at interfaces, at the surface of the junction and in bulk [27].

Moreover, reflection of some of the incident light can negatively affect the solar conversion efficiency, as shown in Figure 9. The light can be reflected at the interface between the sun-facing surface of the solar cell device and the air or at the interface between the solar cell individual layers. Thus, some of the incident light that contributes to the conversion efficiency of solar cells can be affected by this reflection [27]. This is especially a problem for heterojunction devices.

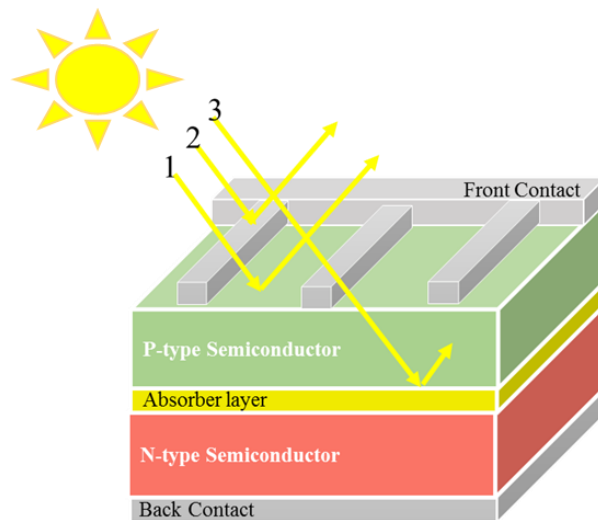


Figure 9: Other factors limiting efficiency: (1) reflected some of the incident light, (2) shadowing losses, and (3) finite thickness of the absorber layer.

Shadowing losses are another contributing factor in reducing solar conversion efficiency. One of the device contacts must be on the sun-facing side of the solar cell device. These front metal contacts, which cover some areas of the sun-facing surface, will, therefore, reflect some of the incident light, thus decreasing the effective active area of the solar cell and reducing the conversion efficiency. This is shown as ray 2 in Figure 8 [27].

Finally, finite thickness of the absorber layer is another factor limiting the efficiency. Even if all layers can absorb the incident light within the solar cell structure, the main absorber layer

cannot be thick enough in order to absorb most of the received light. Therefore, generally, some light will be lost due to transmission through the device or at least transmission through part of the device where absorbed light will no longer be efficiently collected as current [27].

2.1.6 Strategies for Improving Efficiency in Photovoltaics

Greater solar cell efficiency for single-junction silicon cells is achievable by utilizing advanced methods that decrease the effect of the efficiency-conversion limiting factors. These include reducing the thickness of the entire wafer, decreasing the reflection [29] by surface texturing or coating, and decreasing shading by covering the contacts [30]. Employing such concepts can allow high-efficiency solar cells to come close to their ultimate thermodynamic limit. Some of the most current successful methods used to attain high efficiency are tandem solar cells [31] and nano-electronic concepts such as intermediate bands [32] and quantum-wells [33] [34], which can be included in the solar cell device to improve the effective wavelength absorbing range.

2.1.6.1 Tandem Solar Cells

The two significant losses, non-absorption of low-energy photons and thermalization, can be removed if the absorbed photons have higher energies than the semiconductor bandgap. The concept of higher energy photons than the bandgap brings the idea of the tandem solar cell [31], which uses several cells with various bandgaps. An individual cell in the tandem solar cell can convert some photons with energies near and above its bandgap as shown in Figure 10. The wide-bandgap cell is placed on the top to absorb high-energy photons and to transmit low-energy photons to lower cells, which have lower bandgaps. Tandem cells can increase the performance of solar cells as much as increasing the number of cells. Nevertheless, using many cells brings complications and increases the sensitivity of solar cells to the irradiating spectrum, for each cell

must attach in series, match in current, and have low contact resistance.

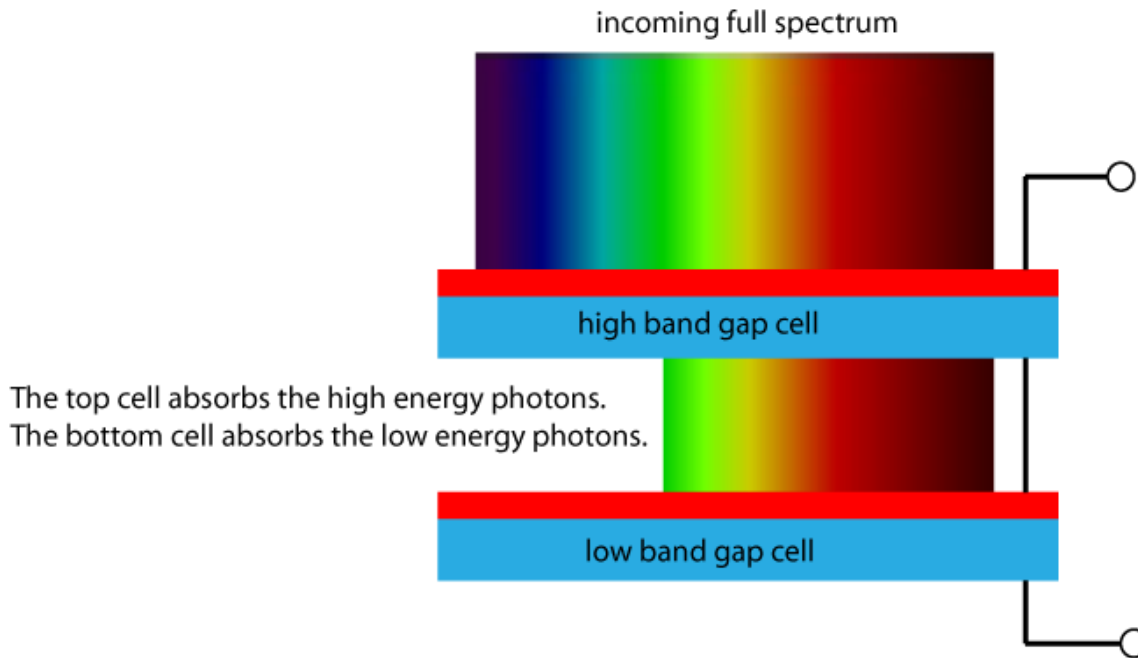


Figure 10: Concept of multi-junction solar cells [26].

2.1.6.2 Quantum Well Solar Cells

Multiple bandgap structures as in the tandem solar cells are also attainable by utilizing a quantum well heterostructure-based solar cell, which was first proposed in 1990 [33][34]. Quantum well based solar cells consist of a p-i-n structure, with multi-quantum wells (MQW) inserted into the intrinsic region (i-region), which is surrounded by the p-n junction, as shown in Figure 11. Thin successive small-bandgap materials surrounded by a bigger-bandgap material are grown in the i-region, which appears as wells on a band diagram, to create the MQWs. If the total thickness of each QW and the spacer layer between it and the next is equivalent to the de Broglie wavelength of the carriers, it forms miniband energy levels that span the entire MQW region. The variance in energy between the valence miniband and the conduction miniband is

now the equivalent bandgap of the MQW. Thus, changing the thickness or spacing of the QWs serves to increase or decrease their bandgap. This MQW absorbs photons, with energy less than the bandgap of the p-n junction or the barrier. These photons would otherwise pass through without being absorbed. Therefore, the solar conversion efficiency increases due to additional absorption in the MQWs, which can mostly be seen as an improvement in the short-circuit current. However, this concept has been plagued because, similarly, the open-circuit voltage of the MQW solar cell lies between the traditional cell formed from the barrier material and the cell consisting of the well material, i.e., at a lower value.

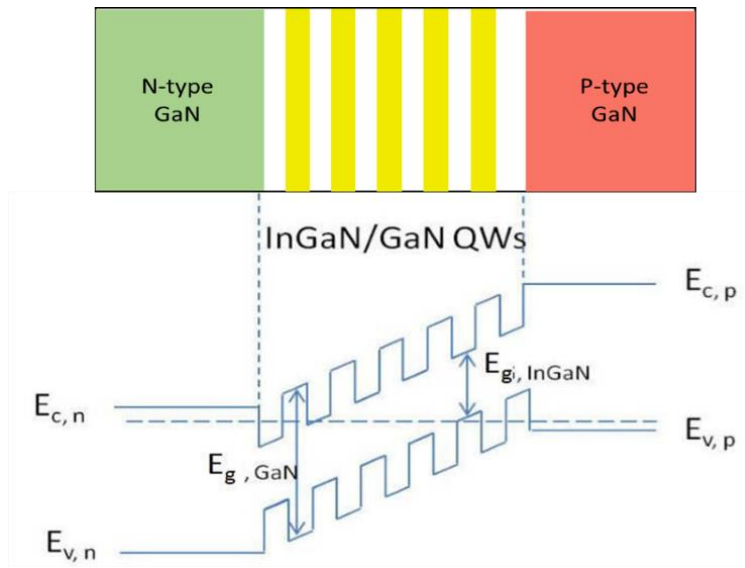


Figure 11: Band diagram and structure of GaN/InGaN quantum-well solar cell [35].

2.2 III-Nitride Materials System

Over the past five decades, PVs have been advanced by several significant jumps in efficiencies with single and triple junction solar cells. Although a diversity of methods has been utilized to improve the effectiveness of these cells, the present efficiency of single and triple

junction solar cells have almost achieved their maxima [36]. Table 1 gives optimum values of the bandgap, maximum theoretical efficiency, and reachable efficiencies of 3-8 junction tandem solar cells under 500 Suns and black-body radiation at 6000 K [4]. A single-junction Si solar cell achieves 24.7% efficiency under AM1.5, and the highest efficiency reached for GaAs solar cells is around 25.1% under AM1.5 [4]. Multijunction solar cells, which include two or three junctions of diverse materials, present higher efficiency than the traditional single-junction solar cells. The current highest efficiency triple-junction solar cell recorded is around 44%, compared to its thermodynamic limit of 56% [4]. Consequently, to reach the target of greater than 50% efficiency, solar cells would require five or more layers with at least one bandgap greater than 2.4 eV.

Table 1: Bandgap values, maximum theoretical efficiency, and reachable efficiencies of 3-8 junctions tandem solar cells under 500 suns and black-body radiation at 6000 K [4].

Number of Junction	Band Gap (eV)								Theoretical Limit (η)	Reachable Limit ($\eta \times 0.8$)
3	0.7	1.37	2						56	44.8
4	0.6	1.11	1.69	2.48					62	49.6
5	0.53	0.95	1.4	1.93	2.68				65	52
6	0.47	0.84	1.24	1.66	2.18	2.93			67.3	53.84
7	0.47	0.82	1.191	1.56	2	2.5	3.21		68.9	55.12
8	0.44	0.78	1.09	1.4	1.74	2.14	2.65	3.35	70.2	56.16

The III-nitride semiconductor material system, which contains GaN, InN, AlN and their alloys, presents a considerable potential in achieving ultra-high efficiency primarily due to its wide range of direct bandgaps from 0.7 eV for pure InN to 6.2 eV for pure AlN. This novel

material system covers more than the entire visible solar spectrum and much of the useful range outside of the visible through simple varying of the composition [1], as shown in Figure 12.

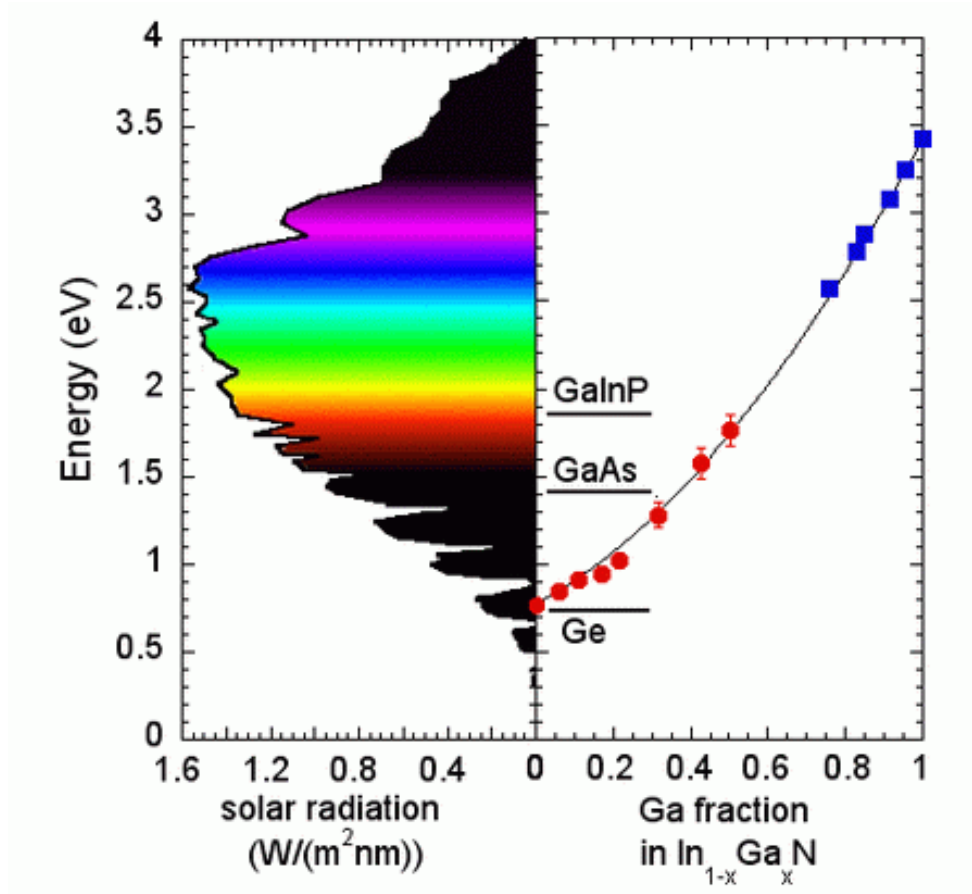


Figure 12: Bandgap of the InGaN materials [37][38].

These materials are widely used in different applications, such as laser diodes (LDs) and light emitting diodes (LEDs) [39]. Besides the appropriate and direct bandgaps, III-nitride materials have additional advantages for use in solar cell devices. InGaN alloys have a very high absorption coefficient [40]. Furthermore, when comparing the optical and electrical properties of current GaInP and GaAs materials in solar cells with that of InGaN alloys, the InGaN optical and electrical properties are significantly better regarding having a formidable opposition to high

irradiation photon energies greater than 2 MeV [36]. This feature leads to using InGaN in the solar cells which will operate under harsh conditions, such as space applications. InGaN is also highly stable with respect to changing temperature, which is valuable for use in solar cells operating under concentrated light [41]. Other advantages include high thermal conductivity, high drift velocity, high mobility, and low effective mass of holes and electrons [42]. Despite the advantages of using InGaN for the solar cells, the efficiency and performance of the solar cell devices are still inferior due to the low crystalline quality of In-rich InGaN layers.

2.2.1 Challenges in III-Nitride-Based Solar Cells

2.2.1.1 Lattice Mismatch

The growth of III-nitride materials has been the focus of most studies due to significant challenges associated with achieving high-quality materials. III-nitride materials usually have a wurtzite crystal structure, which is different from the zinc blend or diamond structures found in GaAs or Si, respectively. Due to the difficulty of finding appropriate lattice-matched substrates, sapphire is still the most commonly utilized substrate for the wurtzite GaN growth.

Unfortunately, the considerable lattice mismatch (+29% between sapphire and InN and -16% between sapphire and GaN) and thermal mismatch (-100% between sapphire and InN and -34% between sapphire and GaN) produces many defects between sapphire and the InGaN materials leading to high dislocation densities. SiC and ZnO are other substrates that are better lattice matched, but, they are much more expensive and still result in high dislocation densities due to both lattice and thermal-mismatch, as presented in Table 2 [4].

A thick, relaxed GaN template layer is typically grown on sapphire to reduce the lattice-mismatch. However, even though the lattice mismatch between InN and GaN is much smaller (around 11%) than either with sapphire, it is still sufficient to create dislocations in the growth of

InGaN on GaN [43][44]. There is a critical thickness for the relaxation of InGaN layers on GaN template, resulting in the formation of dislocations. This critical thickness can be quite small depending on In composition and is less than 5 nm for higher than 20% In [45]. At the critical thickness, as the dislocations form, the device performance will suffer. These dislocations can terminate at the surface of the final crystal and have been shown to directly absorb photons without the creation of usable charge. This leads to a shadowing effect, which reduces efficiencies even more [46]. These defects can be overcome by using multi-quantum wells or superlattices with a thickness less than the critical thickness instead of a thick InGaN layer.

Table 2: Lattice Mismatch and thermal Mismatch of GaN with different substrates [4].

Substrate	Lattice Mismatch (%)	Thermal Mismatch (%)
Si	17	+100
Sapphire	16	-34
SiC	3	+25
ZnO	2	-14

2.2.1.2 Phase Separation

There are several roadblocks to reaching high-performance solar cells based on the III-nitride system, and phase separation in InGaN materials is one of the main challenges. A substantial difference in lattice constants (chemical affinity and interatomic spacing) between GaN and InN can produce a solid phase miscibility gap in the InGaN alloy [47]. Phase separation is spontaneous formation of regions with increased or decreased In content in the material. This creates small regions with a lowered bandgap, which can absorb light with low energy. The size of the phase-separated regions acts in the same way as recombination centers, leading to reducing the I_{sc} and then decreasing the solar cell performance. Moreover, it is obvious from the

quantum-well concept [48] that the lower bandgap phase-separated material can pin down the V_{oc} of the device. Theory predicts that In composition and temperature, besides the strain state of the InGaN materials, can affect the phase separation in InGaN [48]. Therefore, In-rich phases appear in InGaN films through the material growth to attain thermodynamic equilibrium. There are two ways to identify the phase separation: through photoluminescence (PL) and x-ray diffraction (XRD). Thus, it becomes significant to manage the phase separation and determine its impact to create efficient InGaN based solar cells. The growth conditions of the active region design must be optimized by reducing the growth rate associated with low In-composition to overcome the phase separation.

2.2.1.3 P-type Doping and Ohmic Contacts

The p-type conduction is critical for the development of solar cells, but it is extremely complicated to reach high p-type doping concentrations in InGaN alloys because of a normally, high background concentration of donors, which results generally from the high density of defects [49]. Moreover, the usually used p-type dopant, Mg, in InGaN has a very high activation energy. Therefore, very high concentrations of Mg are required to achieve usable carrier densities in InGaN [49]. The activation energy has been characterized to be about 204 meV [50][51]. Therefore, reaching greater hole concentrations at higher In compositions is achievable in theory; nevertheless, the hole concentrations reduce a considerable amount with higher In compositions as a result of degradation in crystal quality [52]. Attaining greater hole concentrations along with smaller series resistance is significant for creating a good p-n junction, especially for wide bandgap materials. This will also result in getting the highest possible V_{oc} out of a given solar cell design. Furthermore, decreasing the resistance of the p-type semiconductor material also causes a reduction in shadowing loss by reducing the constraints on the top contact

grid spacing in a solar cell.

Also, to get better performance from III-nitride-based solar cells, it is required to produce high quality and low resistance ohmic contacts to the p-type as well as the n-type III-nitride materials. An appropriate metal to form an ohmic contact to p-type InGaN is not easy to obtain because of the large theoretically required work function. An example of the most common metals used to achieve ohmic contacts to p-type $\text{In}_x\text{Ga}_{1-x}\text{N}$, for x from 0 to 0.5 is shown in Figure 13 [4]. Here, the band edges of InGaN are exposed with respect to the vacuum level along with the work functions of the respective metals. Several metallization schemes, including high work function metals such as Pt, Pd, Au, and Ni with single-layer, bi-layer, and multi-layers, have been considered for contact formation [53]. Nevertheless, these contacts are not ideal and still result in considerable Schottky barrier at the interface with the p-type InGaN. Many approaches have been considered to decrease the contact resistance of the p-type III-nitride contacts by annealing [54], surface treatment [33], a short-period superlattice (SPS) structure [55], as well as novel metal depositions [56].

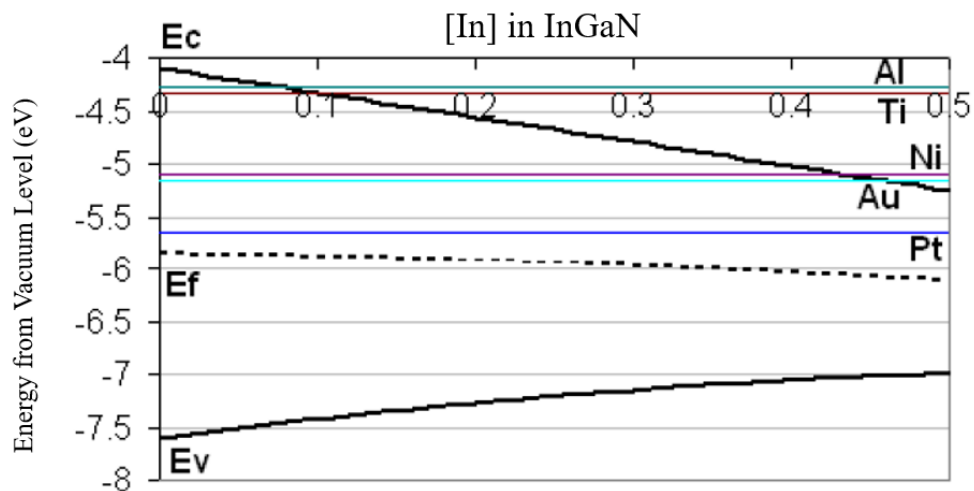


Figure 13: The most common metals used to achieve ohmic-contacts to p-type InGaN [4].

2.3 Conclusion

This chapter reviewed some fundamental principles of solar cell devices, including the solar spectrum, p-n junctions, the operation of solar cells, and solar cell characteristics. Some factors limit the conversion efficiency in the single junction, and some strategies, such as tandem solar cells and quantum-well solar cells, can be used to enhance the conversion efficiency of photovoltaics to overcome some of those factors. Finally, the brief introduction to the III-nitride material system, which provide an opportunity to fabricate high-efficiency solar cells, presents some of the advantages and challenges facing these novel materials. The next chapter will discuss Nextnano³ software to examine and investigate an innovative method to simulate InGaN-based solar cells.

Chapter 3: Novel Method to Simulate III-Nitride Based Solar Cells

3.1 Introduction

Simulation programs are increasingly used mainly due to their considerable potential in understanding the behavior and operation of the simulated systems without the need to fabricate each material and device studied, reducing costs and development time. The use of computer modeling became a general requirement in order to design and investigate solar cell devices as materials became more novel and structures more complicated. Solar cell simulation programs assist, in general, to study the optical and electronic behavior of the solar cell devices and to explore the impacts of the different parameters on the solar cell performance.

This chapter presents an overview of Nextnano³ software as a method used to simulate III-nitride solar cells. Nextnano³ is a simulation tool, established initially at the Walter Schottky Institute [57], and it is written mainly in the Fortran programming language. This simulator is used for semiconductor nanodevices, and it has been used for studying a variety of optical and electrical properties of nanostructures. Moreover, Nextnano³ can model nano-sized systems using an extensive range of materials in the database for III–V, II–VI, and Si/Ge semiconductor materials, which include nitride semiconductors and their alloys. That is also true for different quantum structures, and both wurtzite and zinc-blende polytypes of the nitride system as well as the unique polarization properties resulting from the crystal symmetries [58]. This software can deal with geometries and any combination related to the semiconductor materials in one, two, or three dimensions. Besides Nextnano³, the Nextnano package provides three other simulated tools: Nextnanomat, Nextnano++, and Nextnano QCL. Both Nextnano++ and Nextnano³ offer a self-consistent solution of the Schrödinger equation, drift-diffusion current equation, Poisson equation, and strain equation [57]. The choice of the tool is based on the application for which it

will be used. In the case of the solar cell device, Nextnano³ is recommended to be used.

Nextnano³ is a useful software to study nanoelectronic devices because it is considered not only to study nanoelectronics but also to solve physics problems [50].

Nextnano³ can be freely downloaded from the website after registration. The site offers various tutorials on optoelectronic and electronic semiconductor nanodevices [50]. Nextnano³ is a very general simulator, but it has not been examined for the simulation of solar cells based on InGaN.

3.2 Solving the Software Equations

In order to model and simulate semiconductor solar cells, a simulation tool should have the ability to calculate the basic semiconductor equations: drift-diffusion current equation, Poisson equation, and continuity equation. Nextnano³ provides a self-consistent solution of the basic semiconductor equations to describe the operation of solar cells.

3.2.1 Poisson Equation

The Poisson equation, which is known from the electrostatics, relates the electric displacement field (\vec{D}) to the space charge density (ρ). The Poisson equation can be expressed as

$$\nabla \cdot \vec{D} = \rho \quad (\text{Equation 3-1})$$

Solving the Poisson equation for the divergence of the electric field is substantial for polarization effects in III-nitrides which is included by:

$$\vec{D} = \epsilon \vec{E} + \vec{P} \quad (\text{Equation 3-2})$$

where ϵ is the material's permittivity, \vec{E} is the electric field, and \vec{P} is polarization density. When there is no change time or magnetic field, the electric field can be found by:

$$\vec{E} = -\nabla\phi \quad (\text{Equation 3-3})$$

Substituting Eqn. 3-2 & Eqn. 3-3 into Eqn. 3-1 produces

$$\epsilon \nabla^2 \phi = -\rho + \nabla \vec{P} \quad (\text{Equation 3-3})$$

The electrons and holes participate with a negative charge and a positive charge, respectively, to define the contributors to the charge density in the semiconductor. An ionized donor contributes a positive charge while an ionized acceptor has a net negative charge. Thus, the charge distribution is a nonlinear function of the potential.

$$\rho(\phi) = [p(\phi) - n(\phi) + N_D^+(\phi) - N_A^-(\phi)] \quad (\text{Equation 3-4})$$

where p and n are the mobile charge carrier densities, and N_D^+ and N_A^- are the densities of ionized donors and acceptors.

The solution of the Poisson equation needs identified boundary conditions. Boundary conditions must be indicated at the boundaries between nanostructures and at the metal-semiconductor interface. Even though the system contains contacts, the Poisson equation within the contacts is not solved. As an alternative to resolve the Poisson equation, assumptions on the electrostatic potential inside the contacts are created, and then, they are combined maintaining consistency with the appropriate boundary conditions [59].

3.2.2 Drift-Diffusion Current Equation and Continuity Equation

When applying a bias to the contacts of a device, the device is no longer under equilibrium resulting in a flow of electric currents. A single Fermi level, which is unchanging throughout the instrument, is not enough to describe the charge distribution. However, a fully quantum mechanical calculation of the non-equilibrium distribution of charge is computationally still too challenging for calculations in quasi-two or -three spatial dimensions.

By drift and diffusion processes, the electrons and holes can participate in the current flow.

The total current density of electron (J_e) and the total current of the holes (J_h) can be found [25] by:

$$J_e = q\mu_e n\xi + qD_e \frac{dn}{dx} \quad (\text{Equation 3-6})$$

$$J_h = q\mu_h p\xi - qD_h \frac{dp}{dx} \quad (\text{Equation 3-7})$$

where ξ is the associated electric field strength. The mobilities of electrons (μ_e) and holes (μ_h) are related to the diffusion constant of electrons and holes, D_e and D_h , through the Einstein relationship, which can be found [25]by:

$$D_e = \left(\frac{kT}{q}\right)\mu_e \quad (\text{Equation 3-8})$$

$$D_h = \left(\frac{kT}{q}\right)\mu_h \quad (\text{Equation 3-9})$$

The continuity equations are the last equations in a system which mainly redirects the number of holes and electrons in a system. The net rate of raising the number of electrons in a certain volume is the rate entering minus the rate exiting, which are relative to the current density and with respect to elemental volume of length (δx). The net rate can be found by:

$$\text{rate of entering} - \text{rate exiting} = \frac{A}{q} \{-J_e(x + \delta x)\} = \frac{A}{q} \frac{dJ_e}{dx} \delta x \quad (\text{Equation 3-10})$$

$$\text{rate of generating} - \text{rate of recombination} = A\delta x(G - U) \quad (\text{Equation 3-11})$$

where A is the cross-section area, G and U are generation rate and recombination rate, respectively. Considering the steady state condition, the equation becomes for electrons, and equally for holes [25],

$$\frac{1}{q} \frac{dJ_e}{dx} = (G - U) \quad (\text{Equation 3-12})$$

$$\frac{1}{q} \frac{dJ_n}{dx} = -(G - U) \quad (\text{Equation 3-13})$$

An overall analytical solution of the coupled of nonlinear differential equations, including Poisson, drift-diffusion current equation, and continuity equation, is not possible.

For Nextnano³ software, two approaches are used. The first method is utilized for the ballistic quantum transport calculation in situations comparable to equilibrium and without any effect of scattering. Hackenbuchner has presented the second approach, which combines the traditional drift-diffusion method with a quantum mechanical method for the calculation of the charge carrier densities [59].

Comparable to the Poisson equation, a solution of the drift-diffusion current equations needs to identify the boundary conditions. The boundary conditions must be definite at the interfaces to the contacts and the edges of any nanostructures. As an alternative to resolve the current equations, different assumptions on the quasi-Fermi levels inside the contacts are created, and then they are combined concerning the appropriate boundary conditions.

There are two types of contacts that need to be physically distinguished [59].

1. An ohmic contact forms when the space charge region at the interface between the metal and the semiconductor is small. As a result, the carriers can tunnel across the energy barrier [59]. Near the contacts, the electrostatic potential should be defined such that the local charge is maintained neutral.
2. A Schottky contact forms due to the energy difference between the conduction band edge and the Fermi level pinned by surface states. The finite value of the electric field at the contact is associated with the charge of the occupied surface states [60][61].

3.4 Program Flow

A summary of the program flow of Nextnano³ can be simplified in several steps as presented in Figure 14 [59].

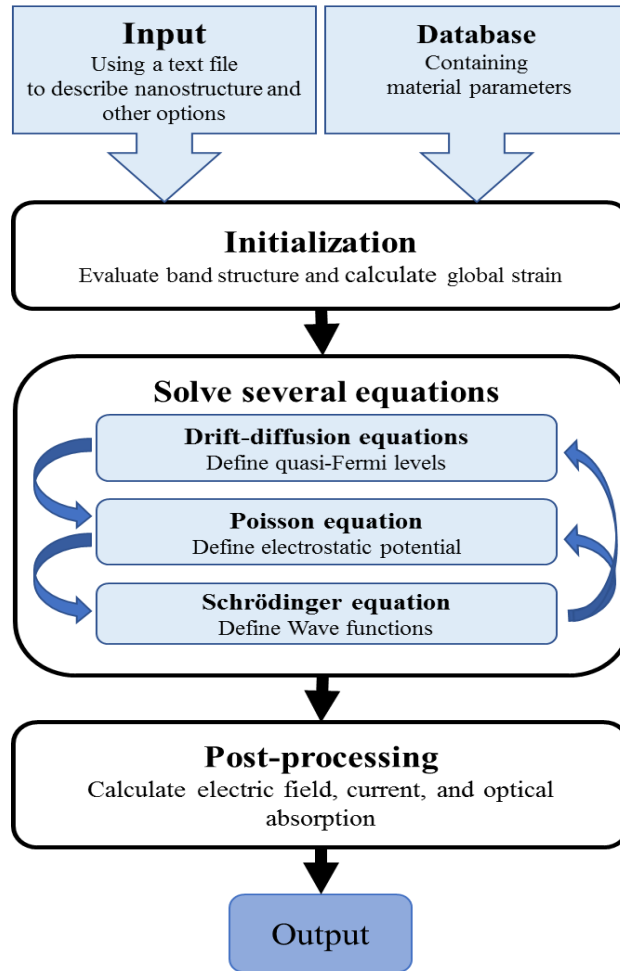


Figure 14: Program flow scheme of Nextnano³ software [59].

In the beginning, the user needs to identify the input files to describe the materials and the geometry of the structure. The contact and all other options are necessary to define the physical system. During the initial phase, Nextnano³ makes a map of the geometry of the device utilizing a grid defined by the user and the materials database, which provides necessary parameters for

the semiconductor materials. Then, the software estimates the band structure of all the materials, calculates a global strain and defines pyroelectric and piezoelectric charges and finally the new band edges based on these charges. The program will then solve the current, Poisson, and Schrödinger equations self-consistently. Newton’s method with an “inexact line” is used as an iterative solving process. During a post-processing phase, optical matrix elements, electrical fields, and current densities can be calculated. Finally, the output of the Nextnano³ will be created as ASCII data files.

3.5 The Parameters of Nextnano³

This section primarily describes the code structure of the Nextnano³ software. The entered code in the input file can be divided into six command groups: General, Sample, Material, Doping, Current and Recombination, and the Output specification, which is typically used for a primary solar cell structure, as presented in the Figure 15. Each command group includes several keywords, which can be referenced to find the default value assigned to specific parameters [59].

Nextnano³ supports a simple feature, called “Find and Replace”, where strings in the file of entry can be exchanged with another string. This feature can be utilized to set a variable in the input file, and the software uses the following format for variable and comment:

`<Variable> = <Value> <Comment>`

where `<Variable>` starts with %, and can include characters (0-9, A-Z, or a-z) and the underscore (_). `<Value>` is any string without !, and it is used as the default value in the input file. `<Comment>` starts with !, and it is utilized as a description of the variable. The comment is optional. The variables are recommended for a good organization to be at the beginning of the input file, but it will be implemented the same regardless of where it is placed as a result of the compiling process [59]. By using the variables, it is possible to define the thickness, doping,

alloy content, grid spacing, and grid nodes and to convert the real number into an integer number. An example of using the variables is in the following lines of code:

```
%ImportReflectivity =<yes/no>
    ! import reflectivity spectrum from a file
%FunctionParser    =<yes/no>
    ! This is an important line to evaluate all functions
%Thickness_pLayer =<value>
    ! thickness of p-type doped layer (DisplayUnit: nm)
%ptypeDoping_pLayer =<value>
    ! doping concentration of p-type (DisplayUnit:1018cm-3)
%GridNodes_pLayer = %Thickness_pLayer/%GridSpacing_pLayer - 1
    ! number of grid nodes for p-type doped layer
%INT(GridNodes_pLayer) = %GridNodes_pLayer
    ! convert the real number into an integer number
```

Now, an explanation of the keywords involved in each group will be presented to identify the default value assigned to the parameters.

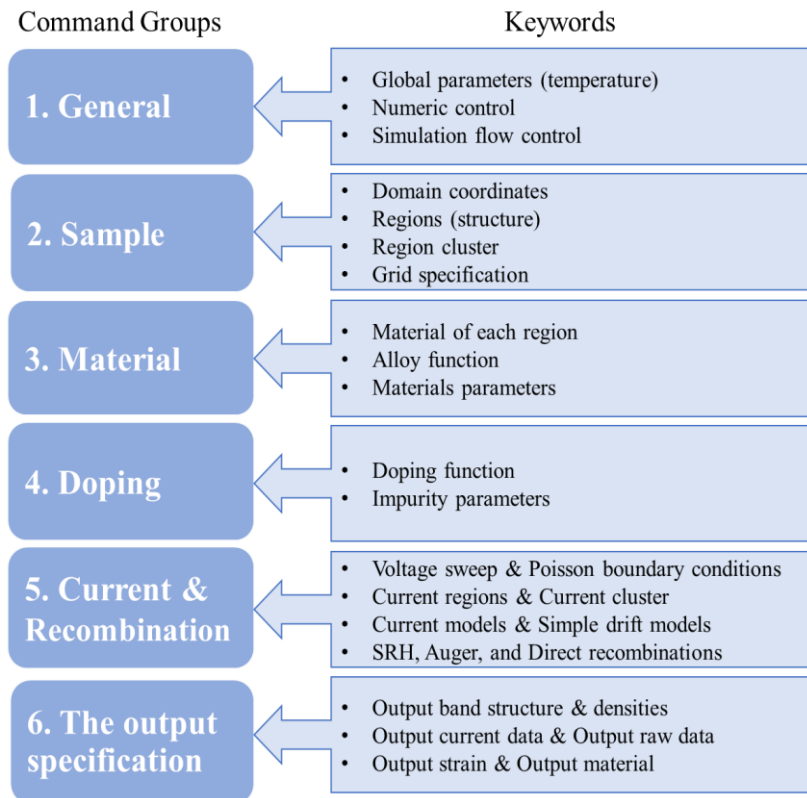


Figure 15: Nextnano³ command groups and primary keywords for solar cell devices.

3.5.1. General

The general group defines the broad parameters used in the simulation, and it includes global parameters (temperature), numeric control, and simulation flow control.

The keyword “\$global-parameters” defines the general parameters, such as temperature, which is applicable throughout the device. Within the keyword “\$numeric-control,” all numerical methods and input parameters can be monitored such as the solving of the strain equation, the Poisson equation, the nonlinear Poisson equation, the current equation, the coupled Poisson-current equation, and other equations. For example, Newton’s method can be implemented to solve the classical nonlinear Poisson equation, a nonlinear Schrödinger-Poisson equation based on predictor-corrector approach, and coupled Current-Poisson equation in 1D [59].

The keyword “\$simulation-flow-control” can control the simulation by telling the software what scheme to use to calculate the equations. Every single flow scheme has a specific process. In every run, the program will first calculate the strain and then apply the flow systems only if the strain calculation is not turned off using “strain-calculation = no-strain.” After that, the program will solve the Poisson equation to define the electrostatic potential. Finally, the flow scheme is completed [59].

3.5.2. Sample

This command group involves domain coordinates, regions (structure), region cluster, and grid specification.

The keyword “\$domain-coordinates” describes the general simulation domain which is limited to a line, a cuboid, or a rectangle based on the dimension for the simulation.

Within the “\$regions” keyword, the structure of solar cells can be defined. Most of the

simulation work in this thesis is based on a one-dimensional object which is a line. The following is an example of the region keyword for a one-dimensional p-n junction.

```
$regions
  region-number      = 1
  base-geometry      = line
  region-priority    = 1
  x-coordinates      = 0d0 10d0
$end_regions
```

The keyword “`$region-cluster`” can cluster the regions to larger objects. Every area should be allocated to a group which can be considered by its “`cluster-number`” which is an integer number (≥ 1). Likewise, the default region, which is the remainder of the simulation domain, is an empty area. Even if it is a blank area, it has to be allocated to a cluster. In every situation, the default zone number must be equal to the highest number defined plus one [59]. The grid specification is a parameter used to determine the size of the grid spacing which can have dramatic influences on the runtime of the software. To reduce the runtime of the software, the grid spacing in different zones which are less attractive can be decreased by lowering the number of nodes for which the equations need to be solved [59].

3.5.3. Material

The material group consists of three keywords which define the material specification of each region, the alloy function, and the materials parameters.

The keyword “`$material`” assists in defining the material assigned to each cluster region.

An example of the format of known materials in the database statement used in the input is [59]:

```
$material
  material-number = 1
  material-name   = GaN
  cluster-numbers = 1
  material-number = 2
  material-name   = In(x)Ga(1-x)N
```

```

cluster-numbers = 2
alloy-function  = constant
$end_material

```

where the alloy function can be constant or linear for a known alloy function, which sets up the function utilized to create the profile of an alloy within the material. Additionally, if the material is completely unknown in the database, or if unique definitions are required, more specification of the materials is possible.

Then, the “\$alloy-function” needs to be specified, and it is utilized to describe a ternary alloy profile. A name of an alloy function has to be presented first in the material keyword, then, within the alloy function keyword, the parameters for different built-in functions, which create the alloy profile, must be defined. The next example is the format for the alloy function in the input of Nextnano³ [59]:

```

$alloy-function
material-number      = 2
function-name        = constant
xalloy               = 0.2d0
$end_alloy-function

```

The final keyword that needs to be defined in the material group is the material parameters. First, if the string of the material-type is known in the database, the program will read the default settings for the defined material-type from the database. Some of the parameters need to be identified by using this keyword. Then, the defaults will be overwritten. However, if the string of the material-type is unknown in the database, the user has to specify all the material parameters, and the related definitions in the “\$material” including “material-model,” and “material-type” [59].

3.5.4. Doping

The doping group includes two keywords: doping function and impurity parameters. First,

the doping can be identified by the created function which is the dimension of the simulation: 1, 2 or 3. Every function is based on one coordinate. The function is utilized for a particular region, but the doping is separated from the region that has been identified before. The doping concentration can be identified in this keyword as in the next example [59].

```
$doping-function
doping-function-number = 1
impurity-number        = 1
doping-concentration    = %ptypeDoping_pLayer !1.0 * 1018cm-3
only-region            = 0d0 %pLayer_right_boundary
$end_doping-function
```

The second is the impurity parameters, which are used to specify the properties of the impurities used in the simulation. The format for the impurity parameters in the input is shown in the following [59]:

```
$impurity-parameters
impurity-number          = 1      ! labelled in doping-function
impurity-type            = p-type! can be p-, or n-type
number-of-energy-levels  = 1      ! only 1 is currently allowed
energy-levels-relative  = 0.01507d0! found in the database
degeneracy-of-energy-levels = 4 !4 for p-type, & 2 for n-type
$end_impurity-parameters
```

3.5.5. Current and Recombination

The current group keywords involve voltage sweep, Poisson boundary conditions, current regions, current cluster, current models, and simple drift models. In order to find the current, the user has to define the contacts, which can be specified using the Poisson boundary conditions, the “current regions,” its clusters, and “current models.”

The voltage sweep keyword is used to apply some bias voltage to a particular contact. This keyword is used to retrieve the current-voltage characteristics. The solar cell device needs to include contacts to apply any voltage, and the Poisson boundary conditions are used to define the contacts as either Schottky and ohmic. The two methods used to simulate these contacts are

equilibrium and nonequilibrium. First, the equilibrium simulation offers a solution to the Poisson equation with a constant Fermi level at 0 eV with boundary conditions given by Neumann, Dirichlet, Mixed, Ohmic, or Schottky conditions. The second method is the nonequilibrium which offers a self-consistent solution of the current continuity and Poisson equations. It is expected that voltage application result in a minimal flow. Thus, the “current-regions” must be specified between the contacts. The essential boundary conditions in nonequilibrium can only be Ohmic or Schottky [59].

The user has to identify the specific current regions and its clusters to compute the current flow according to the applied bias in the Poisson boundary conditions. The user can use a particular current model such as a simple drift-diffusion. The user can also identify diverse regions for various current models. If the current region is not defined, the number of the “current-region” in the whole simulation area can equal one [59].

To specify the drift model, the user needs to set the models for generation, recombination, and models, and provide all related parameters for each material used in the device. The input file or the database must include all the mobility parameters for the covered materials in the current cluster. Even if the mobility parameters of the metal contacts are not utilized in the calculation, they must be present as well [59].

Finally, the keywords: “Shockley-Read-Hall (SRH) recombination,” “Auger recombination,” and “direct recombination” should be defined for solar cell devices. Impurities, generally due to dopant atoms, are the main source of SRH recombination, whereas the high carrier concentration that results from high doping will generally increase the importance of Auger recombination. Finally, direct recombination is, of course, the creation of a photon due to band-to-band relaxation between the conduction and valence bands [59].

3.5.6. The output specification

The input file includes a particular keyword to define the output for every group of existing data. Then, a destination directory is required. The directory name must add a trailing slash such as 'dir\.' The specifications for each output keyword is a flag, which can be “yes” or “no,” or numbers. Examples of output keyword options, which should be included in the input file for solar cell devices, are: “\$global-settings,” “\$output-raw-data,” “\$output-bandstructure,” “\$output-densities,” “\$output-current-data,” and “\$output-material” [59].

After running the simulation, the output of Nextnano³ simulator will be many ASCII files including information on the input structure. The Nextnano³ simulator contains a viewer in the “Output” tag, which assists in visualizing the data as presented in the Figure 16. Nextnano³ can output bandgap, Gamma, I-V characteristics, generation rate, quantum efficiency, and solar cells result, including J_{sc} , V_{OC} , P_{max} , P_{in} , FF, and conversion efficiency [59].

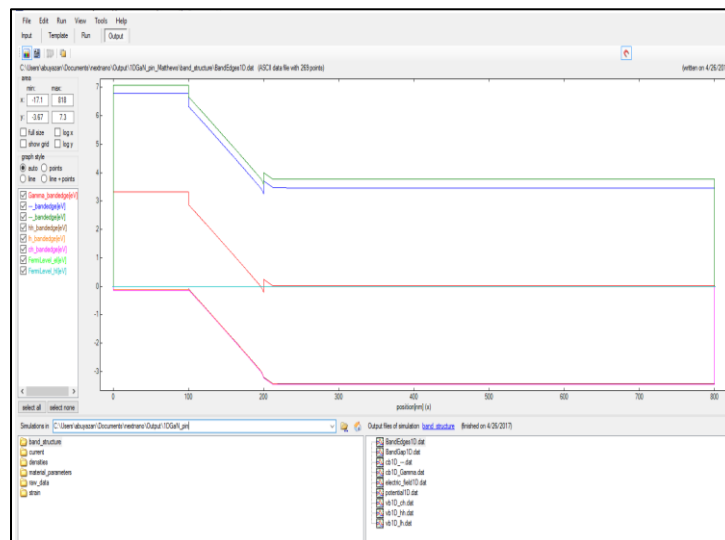


Figure 16: Nextnano³ window showing the 1D band-edges of a double heterostructure InGaN/GaN solar cell: gamma band-edges (red), heavy-hole (brown), light-hole (orange), the electron Fermi level (light green hidden under light blue), and the hole Fermi level (light blue).

3.6 Conclusion

This chapter presented an introduction to Nextnano³ software including some of the equations solved, the program flow, the code structure of the input files, and some of its keywords. In order to demonstrate that Nextnano³ is a suitable software for simulating solar cell devices, the next chapter introduces a comparison between Nextnano³ and PC1D.

Chapter 4: Comparative study of Single-Junction Silicon Solar Cells within Nextnano³ and PC1D

4.1 Introduction

This chapter presents a brief introduction to the Personal Computer One-Dimensional (PC1D) software package and a comparative study of single-junction silicon solar cells using Nextnano³ and PC1D. The variation of I-V characteristics was studied by changing the thickness, and the doping concentrations.

4.2 PC1D Simulation Tool

Personal Computer One-Dimensional (PC1D) software is a commonly used software package for the quick simulation of mainly semiconductor solar cell devices, but it is not very versatile in terms of new materials or nanostructures [62]. At the same time, the Nextnano³ software package has widely be applied to nanostructures and has a vast and customizable database of materials. However, it has not been used extensively to simulate the performance of solar cell devices. Therefore, the PC1D simulator was chosen as a comparison to validate that Nextnano³ can be used for solar cell devices. PC1D is used not only for research purposes but also for an industrial purposes. PC1D assists users in understanding the operation of solar cells and is known to give reliable and expectable results, mainly for silicon-based devices [63]. PC1D uses finite-element analysis as the numerical method to solve the coupled nonlinear equations required to simulate solar cell performance [15] providing I-V characteristics including J_{sc} , V_{oc} , P_{max} , as well as the conversion efficiency.

4.2.1 Operation of PC1D

The operating interface for the PC1D software can be seen in Figure 17. Here, there are four distinct sections on the right side of the “Device Schematic.” The first one is the “DEVICE”

section which consists of general information about the semiconductor device such as the device area and the reflectance. Then, the “REGION 1” section, which covers all of the parameters describing the semiconductor material used in the device. The user can add more regions to create a multijunction or heterojunction device. The third section is the “EXCITATION” which includes the lighting conditions such as applied temperature and the light source. The “RESULTS” section provides the output of solar cell’s performance.

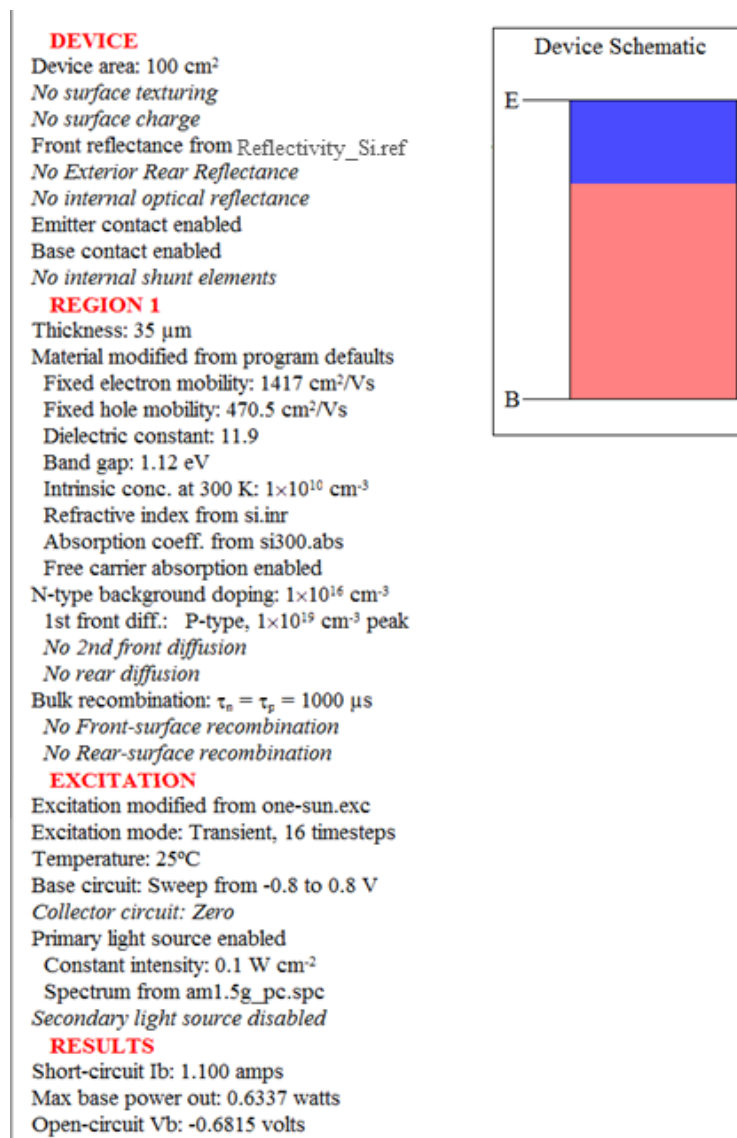


Figure 17: An example of the operation interface of the PC1D software.

4.3 Differences Between Nextnano³ and PC1D

To explain the electrical characteristics of solar cells, differential equations, which form the semiconductor equations with appropriate boundary conditions, are expanded to describe the solar cell performance. The coupled system of nonlinear partial differential equations is complicated and, in most cases, impossible to be explicitly solved in general. Therefore, numerical techniques must be applied to solve the semiconductor equations. This numerical method contains the discretization of a device in space and time and, therefore, a solution of such a system can be obtained from the discretization process. The most common three methods which are being employed to discretize a particular semiconductor structure are the finite difference, finite element, and finite boxes methods [64]. The chosen method for discretizing the device is based on several factors including the partial differential equations along with the boundary conditions, the domain geometry, and the coordinate scheme used to describe the continuous problem [65].

The Finite Difference Method (FDM) is the used method by Nextnano. FDM is the oldest and the most straightforward process, and it is exceptionally stable. This approach is a differential scheme, which divides the domain into sub-domains by determining an organized grid, where the grid is a group of mesh streaks parallel to the coordinate axes. This process produces a scheme of nonlinear equations, which can be solved by standard algorithms such as Newton's method [64].

PC1D uses the Finite Element Method (FEM), which is an integral scheme. This method splits the domain into a finite number of subdivision domains or finite elements without elimination or overlap. The most frequently chosen shape for the individual element is a triangle.

“At each element, an approximation of the solution is sought in such a manner that outside the element the contribution to the total approximate solution is zero.

The approximate solution at each of these elements is expressed in terms of a polynomial and the coefficients of these polynomials are determined by approximate solutions at each of the nodes of the elements and/or middle of the edges of the elements” [66].

The discretization schemes differ between the FEM and FDM. The FEM is suitable for more complex geometry than FDM, though it demands more computational resources than FEM, which discretizes equations on groups of mesh points (Figure 18). However, FDM discretizes derivatives at the nodes of a homogeneous mesh (Figure 19). The mesh in the FDM is square while the mesh in FEM can take flexible geometrical forms.

The solution using the two methods can be different due to discretization differences and calculation errors. Ultimately, FEM methods usually achieve better accuracy than FDM however at the great expense of processing time [66]. Table 3 summarizes the differences and similarities between the two methods.

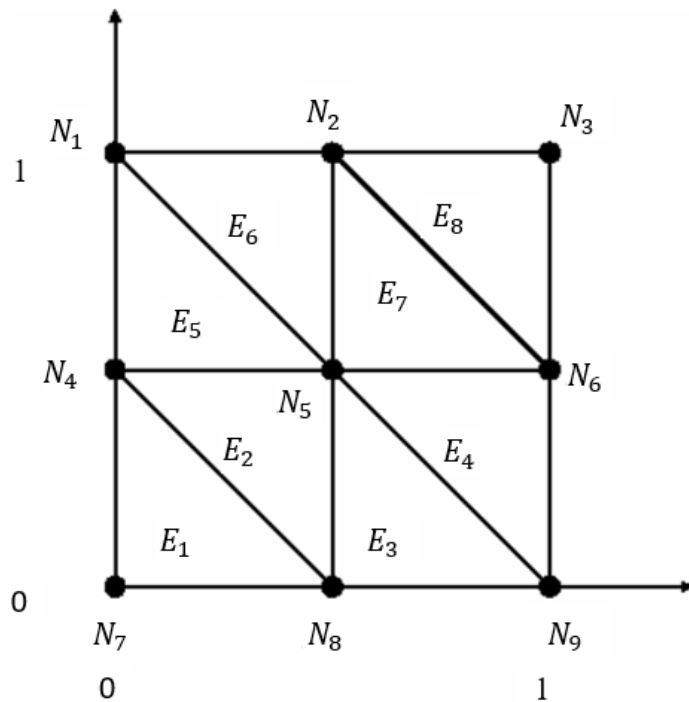


Figure 18: Finite element discretization [66].

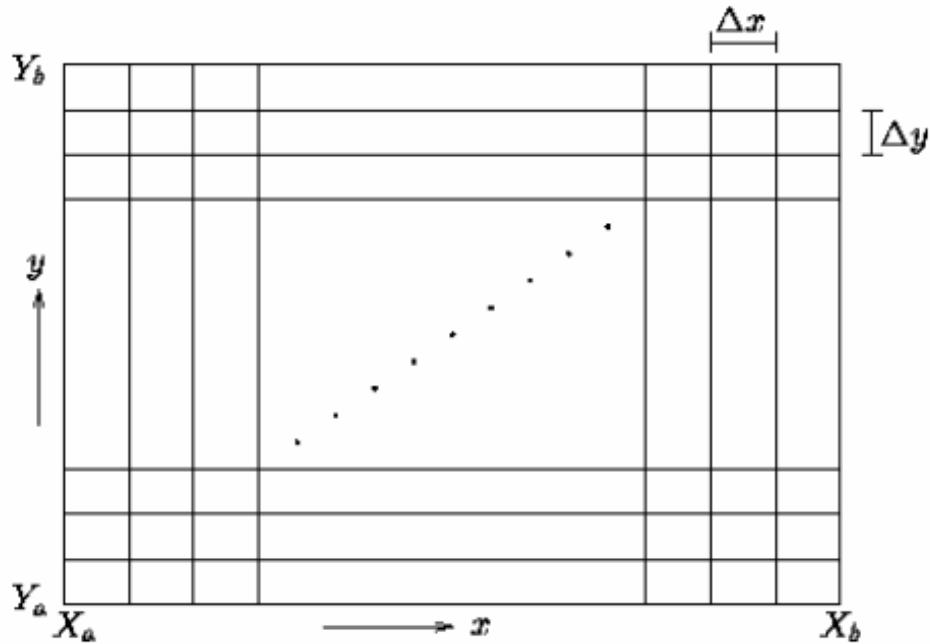


Figure 19: Finite difference discretization [66].

Table 3: Some differences and similarities between finite difference method and finite element method [67].

	Finite-element method	Finite difference method
Differences	<ul style="list-style-type: none"> ▪ Use irregular grid ▪ Determine the mesh itself ▪ Discretizes equations at cells of a mesh ▪ A lot of calculations are done in each time step ▪ Require an iterative procedure to follow a non-linear constitutive law 	<ul style="list-style-type: none"> ▪ Use regular grid ▪ User has to determine the mesh ▪ Discretizes derivatives at nodes of an homogeneous mesh ▪ A little calculations are done in each time step ▪ Not required for an iterative procedure to follow a non-linear constitutive law
Similarities	<ul style="list-style-type: none"> ▪ Use Newton method to solve the non-linear equations 	<ul style="list-style-type: none"> ▪ Use Newton method to solve the non-linear equations

4.4 Simulation of Single-Junction Silicon Solar Cells in Both Simulation Tools

4.4.1 Silicon Solar Cell Structure

The initial solar cells were simulated using silicon, a well-studied material for photovoltaic devices, with more than 85% of the currently fabricated production solar cells being based on it [51]. Si was chosen as the material for the comparison between the two packages because it is a well-known material in both software tools which will make the comparison much more manageable.

The p+/n structure of a crystalline silicon solar cell utilized in this chapter is presented in the Figure 20. The doping concentration of the n-type base is $1 \times 10^{16} \text{ cm}^{-3}$, with a $30 \mu\text{m}$ thickness while the doping concentration of the p+ emitter is $1 \times 10^{19} \text{ cm}^{-3}$ at the front surface, with a thickness of $5 \mu\text{m}$.

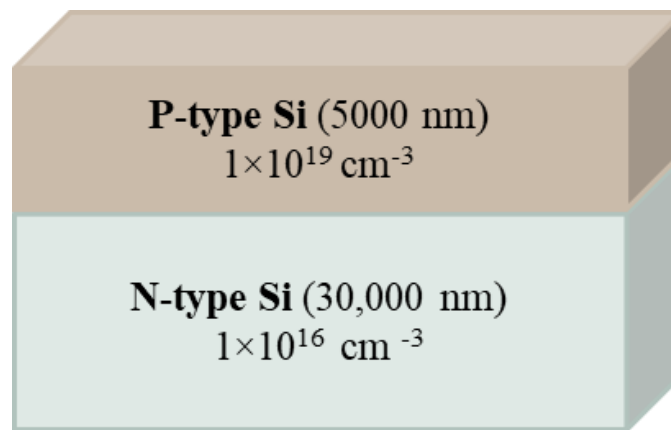


Figure 20: Silicon solar cell structure.

4.4.2 Input Parameter

4.4.2.1 Optical Parameters in Nextnano³ and PC1D

The optical parameters of silicon used in Nextnano³ and PC1D were obtained through a

combination of existing values in the database in both simulators. The solar radiation applied in this simulation is ASTM G173-03 Reference Spectra for AM1.5G under one sun, shown in Figure 21. This solar spectrum was applied to the input of both Nextnano³ and PC1D. Importing the solar photon intensity into the simulation assists in computing the number of carriers contributing to the solar cell devices at different wavelengths. The absorption coefficient of Si is also required to determine the cell response. Silicon is an indirect bandgap material which leads to a significantly reduced absorption coefficient as compared with direct bandgap semiconductors. The absorption coefficient used in PC1D and Nextnano³ for Si is shown in Figure 22.

The two packages require different optical inputs to calculate the performance of the solar cell. PC1D makes use of the refractive index while Nextnano³ requires the reflectivity. The refractive index was taken from the PC1D database. In order to apply the same optical input in both simulators, calculating the imaginary part of the refractive index requires obtaining the reflectivity of Si. The imaginary part is found by:

$$K = \frac{\lambda\alpha}{4\pi} \quad (\text{Equation 4-1})$$

where λ and α are the wavelength and absorption coefficient, respectively. The absorption coefficient was taken from PC1D database and used in both simulators. The refractive index and the calculated imaginary part are shown in Figure 23.

These results were used to get the reflectivity of Si by the following equation:

$$R = \frac{(n - 1)^2 + K^2}{(n + 1)^2 + K^2} \quad (\text{Equation 4-2})$$

where n is the index of refraction for Si. The calculated reflectivity used in Nextnano³ is presented in Figure 24.

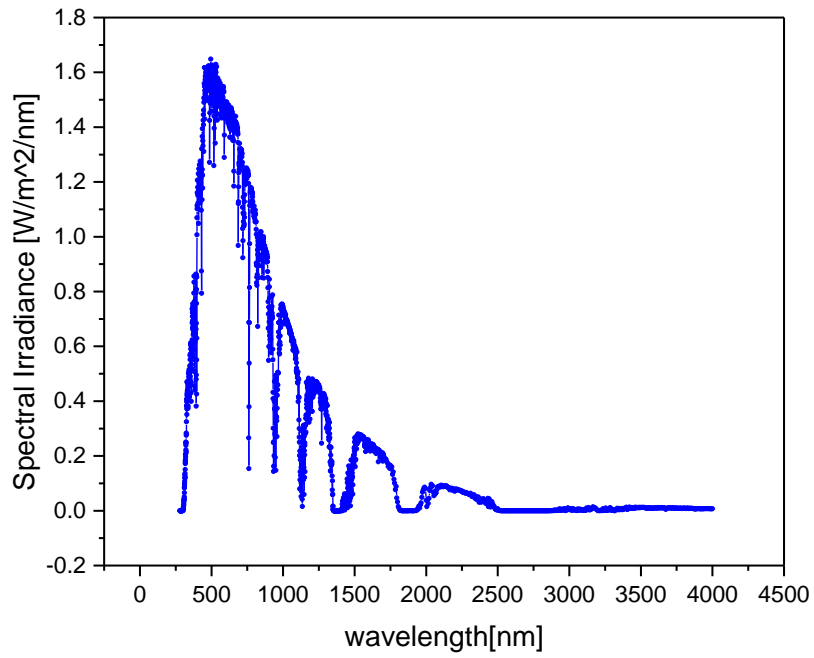


Figure 21: The used solar spectrum for AM1.5G.

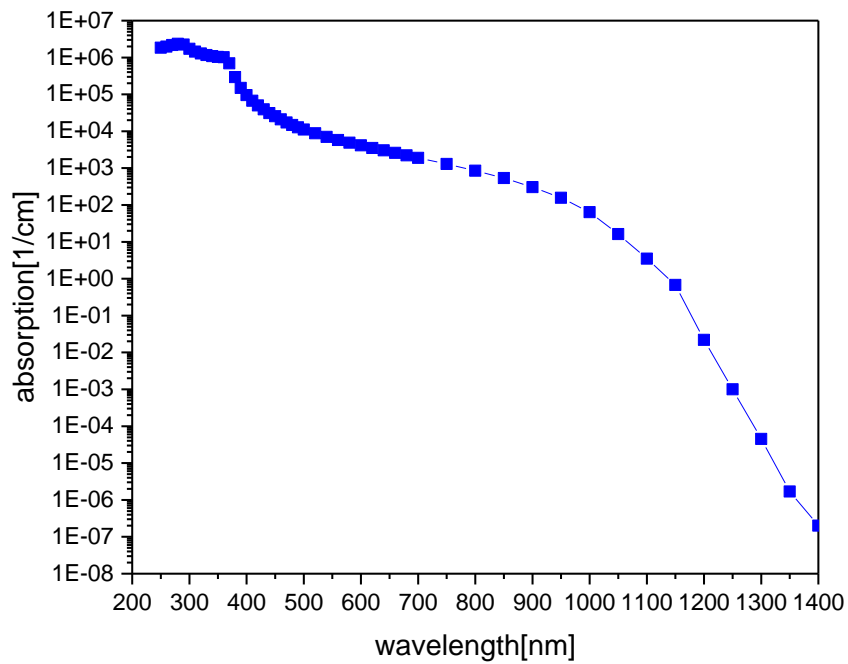


Figure 22: Absorption coefficient of silicon.

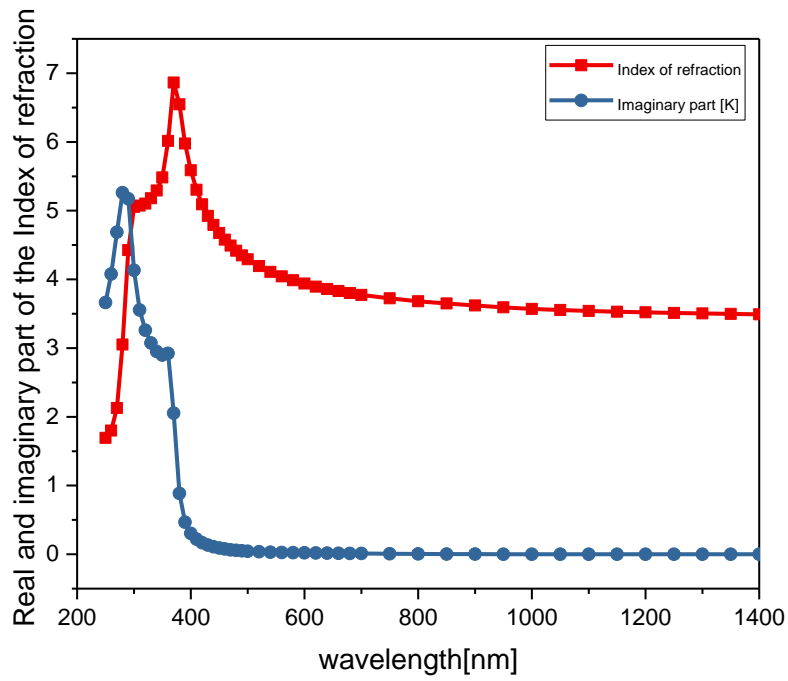


Figure 23: The real and imaginary part of Si refractive index vs. wavelength.

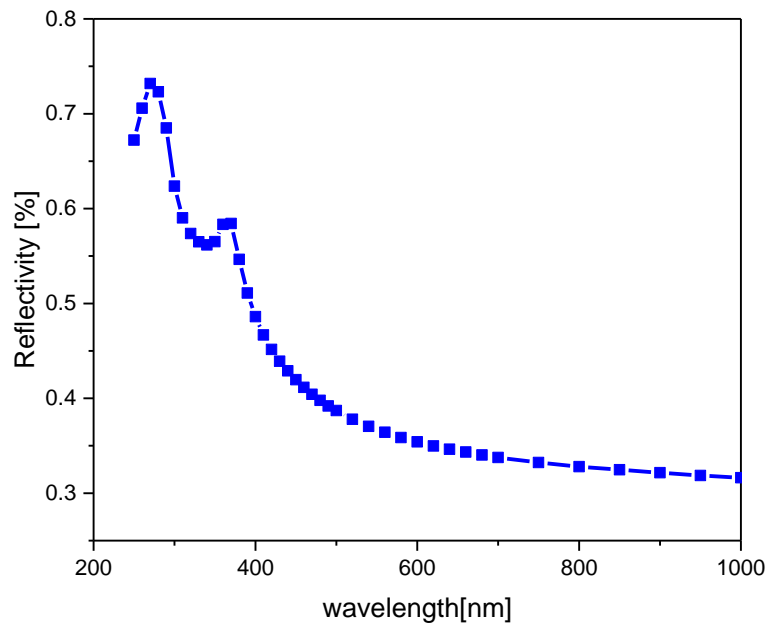


Figure 24: The computed reflectivity for silicon.

4.4.2.2 Electrical Parameters in Nextnano³ and PC1D

The material electrical parameters used were matched (to the extent possible) in both simulators. These parameters for Si are summarized in Table 4.

Table 4: Electrical parameters for silicon.

Electrical Parameters	Value
Electron mobility	1417 cm ² /Vs
Hole mobility	470.5 cm ² /Vs
Dielectric constant	11.9
Band gap	1.09
Temperature	300 K
Lifetime	1000 us
Auger for electron	2.8e-31 cm ⁶ /s
Auger for hole	9.9e-31 cm ⁶ /s
Bulk doping (n & p)	7.1e15 cm ⁻³

4.4.3 Calculation of Si Solar Cell

The electrical performance of the Si solar cell was also analytically derived, due to its relative simplicity, in order to critique the outcomes of both PC1D and Nextnano³. The solar radiation applied in the calculation is ASTM G173-03 Reference Spectra for AM1.5G for one sun. In order to calculate the photon flux which is expressed as the number of photons per second per unit area, the photon energy in joules needs to be first calculated by:

$$E_{ph} = \frac{hc}{\lambda} \quad (\text{Equation 4-3})$$

where hc is the Planck constant times the speed of light, respectively, and λ is the wavelength of light in nm. Then, the photon flux in cm⁻² s⁻¹ was computed by:

$$Photon\ flux = \frac{solar\ spectrum\ (w\ m^{-2}\ nm^{-1}) \times (\lambda_2 - \lambda_1)(nm)}{10000} \quad (Equation\ 4-4)$$

where the solar spectrum used was for AM1.5G under one sun.

The photon flux is essential in defining the number of electrons generated, and thus the current produced from the solar cell device. Therefore, to calculate the number of electrons produced at any point within the solar cell, the generation rate G , which is a critical parameter in the operation of solar cell, is used. The generation rate can be found by:

$$G = \alpha N_0 (e^{-\alpha x}) \quad (Equation\ 4-5)$$

where α is the absorption coefficient, N_0 is the photon flux, and x is the depth into the semiconductor from the light exposed surface. The absorption coefficient is an essential parameter to determine the generation rate and is the same as is used in the simulations. To determine the largest current drawn from the solar cell, the short-circuit current, as explained in detail in Section 2.1.4, can be found by:

$$J_{sc} = qG(L_n + L_p) \quad (Equation\ 4-6)$$

where L_n and L_p are the diffusion lengths of the electron and holes respectively. The diffusion length can be defined as the typical length that a carrier travels between generation and recombination. These can be calculated by:

$$L_e = \sqrt{D_e \tau_e}, \quad L_h = \sqrt{D_h \tau_h} \quad (Equation\ 4-7)$$

where τ_e and τ_h are the lifetimes of the electrons and holes, and D_e and D_h are the diffusivity of electrons and holes, respectively. Heavily doped semiconductors have higher recombination rates leading to shorter diffusion lengths. However, longer diffusion lengths can be obtained by using materials with longer lifetimes. Thus, the lifetimes are an important quantity that must be considered when choosing the semiconductor materials for solar cells [26]. In order to define the

diffusion length, the diffusivity must first be calculated by:

$$D_e = \frac{KT}{q} \mu_e, D_h = \frac{KT}{q} \mu_h \quad (\text{Equation 4-8})$$

where μ_e and μ_h are the mobility of majority carriers for electrons and holes respectively, and these mobilities can be obtained by:

$$\mu_e = 65 + \frac{1265}{1 + \left(\frac{N_D}{8.5 \times 10^{16}}\right)^{0.72}} \quad (\text{Equation 4-9})$$

$$\mu_h = 47.7 + \frac{447.3}{1 + \left(\frac{N_A}{6.3 \times 10^{16}}\right)^{0.76}} \quad (\text{Equation 4-10})$$

where N_D and N_A are the donor concentration and acceptor concentration in cm^{-3} correspondingly.

All the above parameters can be used to compute the dark saturation current (J_0) which is an essential parameter to differentiate between different diodes. J_0 is used to measure the recombination in a solar cell [26], and can be calculated by:

$$J_0 = \left(\frac{qD_e n_i^2}{L_e N_A} + \frac{qD_h n_i^2}{L_h N_D} \right) \quad (\text{Equation 4-11})$$

where n_i is the intrinsic carrier concentration in the semiconductor materials.

The remaining parameters to define the solar cell results, including V_{oc} , FF , and, η , as described in detail in Section 2.1.4, were calculated by the following equations:

$$V_{oc} = \frac{KT}{q} \ln \left(\frac{J_{sc}}{J_0} + 1 \right) \quad (\text{Equation 4-12})$$

$$FF = \frac{v_{oc} - \ln(v_{oc} + 0.72)}{v_{oc} + 1}, \quad v_{oc} = \frac{V_{oc}}{\left(\frac{KT}{q}\right)} \quad (\text{Equation 4-13})$$

$$\eta = \frac{V_{oc} J_{sc} FF}{P_{in}} \times 100 \quad (\text{Equation 4-14})$$

where P_{in} is the incident power in the solar cell device. The IV curve of a solar cell under illumination can be calculated by using the following:

$$I = I_L - I_0 \left[e^{\left(\frac{qV}{nkT} \right)} \right] \quad (\text{Equation 4-15})$$

where I_0 can equal I_{sc} if the series resistance is very small.

4.4.4 Results

In this section, all the simulation results of the single-junction Si solar cell obtained by both Nextnano³ and PC1D will be discussed and compared with the analytical results. The simulation results of the Si solar cell are presented in Table 5, which contains short circuit current, J_{sc} , open circuit voltage, V_{oc} , maximum power output, P_{max} , fill factor, FF , and the solar conversion efficiency, η . These parameters are the most principal to characterize solar cell performance.

Table 5: Si solar cell simulation results.

<i>Solar cells output</i>	Nextnano³	PC1D	Calculation
J_{sc} [A/m²]	94.7	89.7	70
V_{oc} [V]	0.56	0.66	0.7
P_{max} [W]	43	49	41
FF	0.81	0.83	0.84
η	4.34	4.9	4.14

These parameters can be extracted from the I-V curves of the Si solar cell which are shown in Figure 25. The solid red line with square points is from Nextnano³, the solid blue line with circle points is from PC1D, and the light purple solid line with triangle points is the I-V curve plotted using the analytical solution.

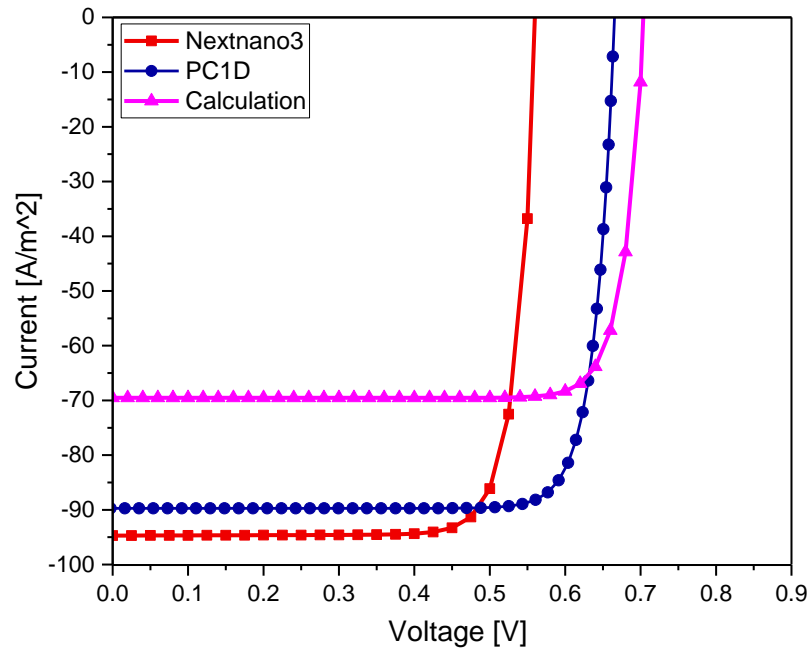


Figure 25: Comparison of I-V curves for Si solar cells.

To ensure an accurate comparison of simulations between the two simulators and the analytical calculation, the optical and electrical parameters used in all cases were kept the same, as defined in detail in Section 4.3.2. The only notable difference is the numerical methods used by each simulator, which was discussed in more detail in Section 4.2.

As presented above, Table 5 indicates a decent agreement, although not exact, between the output results in Nextnano³ and PC1D and the calculation. When comparing Nextnano³ with PC1D, the difference in solar conversion efficiency is only 0.56%. This can generally be attributed to variations in the discretization and numerical methods and is acceptable for the purpose of this comparison. However, when comparing the output data of Nextnano³ with the analytical calculation, the difference in solar conversion efficiency is only ~0.2%.

Accepting the absolute variation in the results, a comparison between the simulation

packages was made by varying the thickness of the emitter of the Si solar cell. The other three parameters, thickness, doping concentration of n-type absorber layer, as well as the doping concentration of p-type emitter, were fixed.

Changing the Thickness of P-type Emitter

Here, the doping concentration of the n-type base was fixed at $1 \times 10^{16} \text{ cm}^{-3}$, the thickness was fixed at 30,000 nm, while the doping concentration of the p-type emitter was fixed at $1 \times 10^{19} \text{ cm}^{-3}$. These parameters are shown in Figure 26. The thickness of the p-type emitter was varied between 1000, 5000, and 10,000 nm.

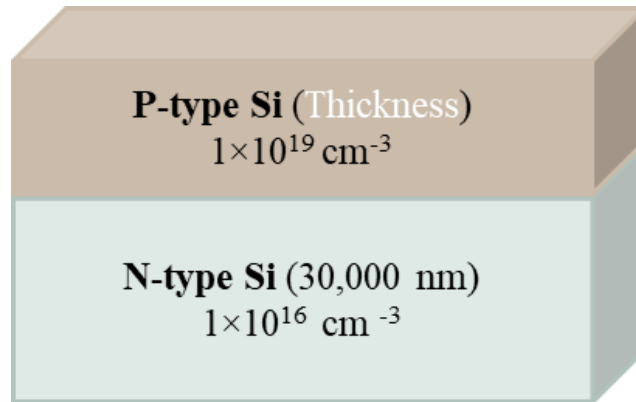


Figure 26: Fixed parameters in Si solar cell structure varying the p-type thickness.

The output I-V curves of the different p-type thicknesses using PC1D and Nextnano³ are presented in Figure 27 and Figure 28. The output I-V curves from both simulators show that increasing the thickness of the p-type region negatively affects both the J_{sc} and V_{oc} . The smallest thickness (1000 nm) shows the best response in both cases, while the resulting I-V curves decrease monotonically with increasing thickness. The differences between the two simulations in J_{sc} and V_{oc} was $\sim 6.3\%$, and $\sim 27.3\%$, respectively, which is within a suitable range.

Additionally, the thickest device simulated (10,000 nm) had the poorest performance. Here the differences in J_{sc} and V_{oc} were $\sim 23.3\%$ and $\sim 21.15\%$, respectively. More important than the comparison of the absolute values is that the trends observed by changing a parameter are identical and of similar magnitude as obtained from each simulation package.

For completeness, to explain the physical response of the device, the p-type region has a fixed minority diffusion length. As the thickness of this emitter gets more substantial, more carriers are absorbed outside of that diffusion length from the base and cannot be used as photocurrent. Therefore, as the emitter gets thicker, the device operation decays.

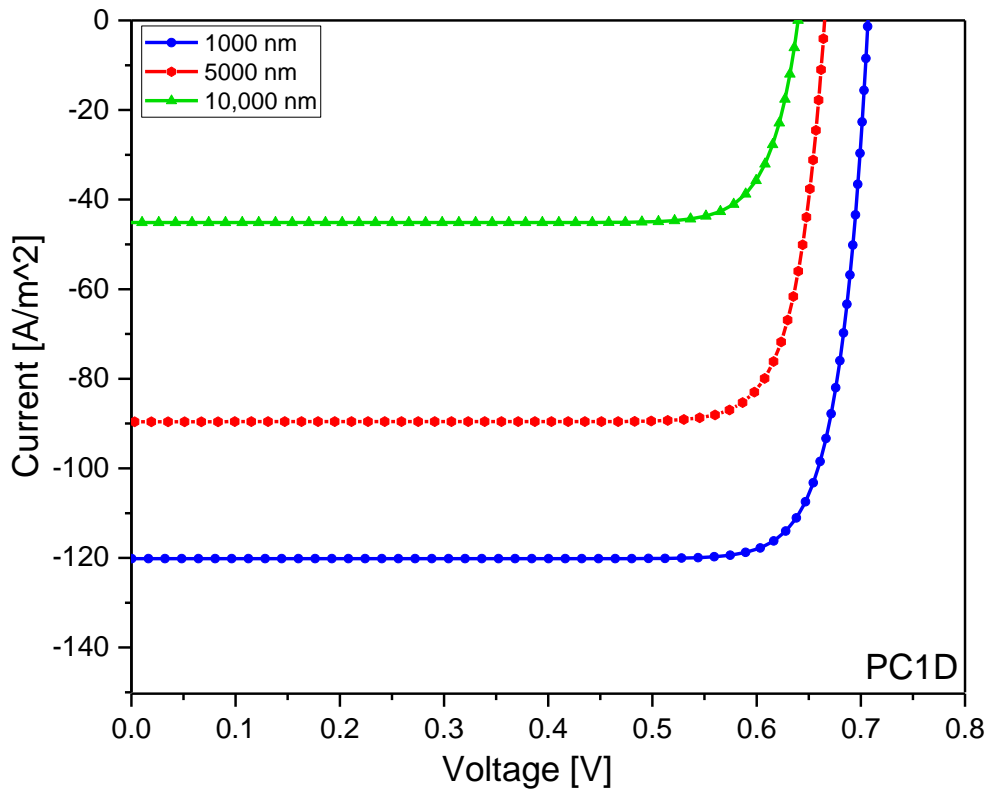


Figure 27: Output I-V curves for different thickness of p-type emitter using PC1D.

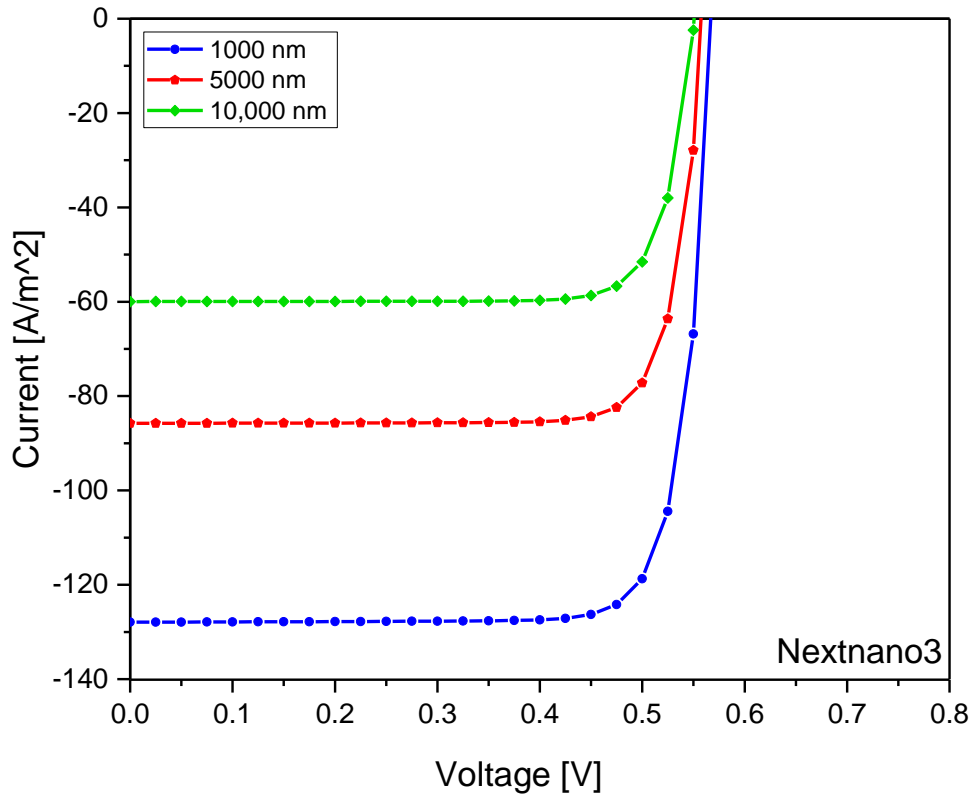


Figure 28: Output I-V curves for different thickness of p-type emitter using Nextnano³.

Consequently, this comparison successfully demonstrates that the modeling and simulation, specifically for solar cells, is acceptable using Nextnano³. Therefore, the output results of the two simulators, as well as of the fundamental drift-diffusion equations, are acceptably similar. The simulation results of single-junction Si solar cell prove the feasibility of using Nextnano³ software for solar cell simulation. Hence, the next step was to use Nextnano³ software to simulate III-nitride based solar cells.

Chapter 5: Simulating III-Nitride Based Solar Cell within Nextnano³

The primary motivation behind this work was to develop the use of Nextnano³ software to simulate III-nitride-based solar cells in order to make the future use of it possible for nanostructured III-nitride solar cell research. This was motivated, not only by the range of bandgap energies available to work with in the InGaN system, but also by the extremely high absorption coefficients as compared to Si (potentially absorbing most available light within ~200 nm) as well as the widespread adaptation of InGaN in blue light emitting diodes in spite of their relatively low material quality [68].

Nevertheless, the growth of III-nitride materials has been a significant focus of research due to the substantial challenges associated with achieving high-quality materials, many of which are a direct result of the lack of native GaN substrate material to grow on. In that absence, sapphire substrates are generally used which result in high defect densities in the as-grown materials. These defects can be overcome to some degree by using multi-quantum wells (MQW) or superlattices with a small thickness instead of thick InGaN layers, for example. Another challenge is phase separation for high In content InGaN alloys. This prevents the growth of thick layers of these compositions of InGaN, which includes the green band where the ultra-high efficiency green light can be observed. The separate phases of the material can act as recombination centers, leading to reducing the short-circuit current and decreasing the solar cell performance. However, it is recently becoming possible with advanced growth techniques to both control the phase separation and in-fact exploit it in order to grow material which might be usable for ultra-high efficiency solar cells [52].

Even though fabrication of different InGaN-based solar cells have shown some promising results, the conversion efficiencies are still lower than 2% which is much lower than the

theoretical maxima for simple designs [69]. In order to optimize their performance using novel structures without growing and fabricating every possible combination, simulation-based investigations should provide useful understanding. In order to take the first steps toward realizing this simulation-based study, in this work the performance of single-junction InGaN solar cells was studied as a function of some simple parameters including the indium composition and the inclusion of an extended intrinsic region using Nextnano³.

5.1 Structure

The structure of the single-junction $\text{In}_x\text{Ga}_{1-x}\text{N}$ solar cells used for theoretical simulation is presented in Figure 29. The doping concentration of the p-type emitter is $1 \times 10^{18} \text{ cm}^{-3}$, with a thickness of 200 nm, and the doping concentration of the n-type base is $1 \times 10^{17} \text{ cm}^{-3}$, with a 1000 nm thickness.

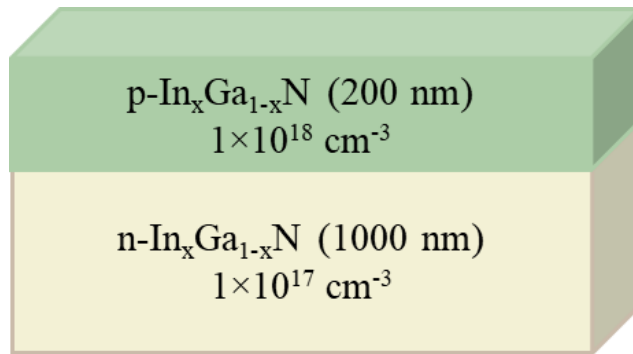


Figure 29: $\text{In}_x\text{Ga}_{1-x}\text{N}$ solar cell structure.

5.2 Input Parameters

The optical parameters of $\text{In}_x\text{Ga}_{1-x}\text{N}$ alloys were obtained through a combination of existing values in the Nextnano³ database and published results (Table 6). The solar radiation applied in this simulation is ASTM G173-03 Reference Spectra for AM1.5G under one sun, as was offered

in Figure 21. In addition, the absorption coefficient (α) of the $\text{In}_x\text{Ga}_{1-x}\text{N}$ alloys were calculated [69] by:

$$\alpha = (1.0 \times 10^5) \sqrt{C(E_{ph} - E_g) + D(E_{ph} - E_g)^2} \quad (\text{Equation 5-1})$$

where C and D are composition dependent parameters found in Table 6 [70]. E_{ph} is the photon energy, which can be calculated using Equation 4-3, and E_g is the indium energy bandgap of the $\text{In}_x\text{Ga}_{1-x}\text{N}$ alloys at 300 K, which can be calculated [69] by:

$$E_g = x \cdot E_g^{\text{InN}} + (1 - x) \cdot E_g^{\text{GaN}} - b \cdot x \cdot (1 - x) \quad (\text{Equation 5-2})$$

where x is the indium content in the $\text{In}_x\text{Ga}_{1-x}\text{N}$ alloys. E_g^{InN} , the bandgap energy of InN, is 0.7 eV, and E_g^{GaN} , the bandgap energy of GaN, is 3.42 eV. The bowing parameter, b , is 1.43.

Table 6: The composition dependent parameters used to calculate the $\text{In}_x\text{Ga}_{1-x}\text{N}$ absorption coefficient of the $\text{In}_x\text{Ga}_{1-x}\text{N}$ alloys [70].

x	C	D
1	0.69642	0.46055
0.83	0.66796	0.68886
0.69	0.58108	0.66902
0.57	0.60946	0.62182
0.5	0.51672	0.46836
0	3.52517	-0.65710

The absorption coefficients used for various indium compositions in the $\text{In}_x\text{Ga}_{1-x}\text{N}$ material system are shown in Figure 30. For $x = 0.2$, the data was taken from the Nextnano³ database,

while the other values, for $x = 0.5, 0.6, 0.7,$ and $0.8,$ were calculated using Equation 5-1 and the published data included in Table 6. The InGaN layers have very high absorption coefficients, on the order of 10^5 cm^{-1} for optical energies above the bandgap, and then they fall very quickly for energies lower than the bandgap as a result of the direct nature of the bandgap as opposed to the indirect bandgap for Si [71]. The absorption coefficient of $\text{In}_x\text{Ga}_{1-x}\text{N}$ materials is one order of magnitude greater than that of GaAs. Thus, a considerable amount of light can be absorbed by a small thickness in the $\text{In}_x\text{Ga}_{1-x}\text{N}$ materials [71].

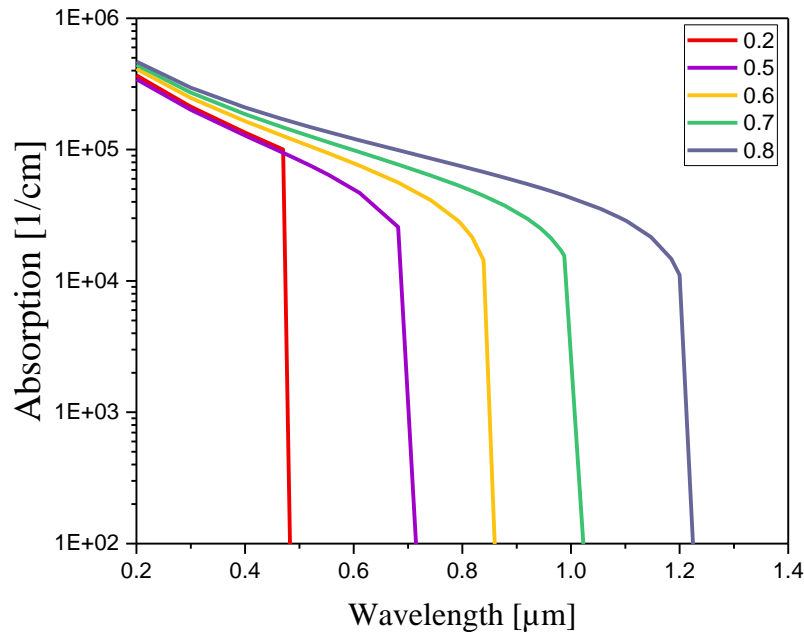


Figure 30: $\text{In}_x\text{Ga}_{1-x}\text{N}$ absorption coefficient for various indium content.

The temperature used in all the simulation of the $\text{In}_x\text{Ga}_{1-x}\text{N}$ solar cells was 300 K. The mobility of both electrons and holes for the $\text{In}_x\text{Ga}_{1-x}\text{N}$ materials was set at $100 \text{ cm}^2/\text{Vs}$. To simplify the simulations, some assumptions were made. The Auger recombination and the Shockley-Read-Hall (SRH) recombination were turned off, leaving direct, band-to-band recombination as the only recombination mechanism used in the InGaN simulations, and it was

set at $1.1 \times 10^{-8} \text{ cm}^3/\text{s}$.

5.3 Simulating Single-Junction $\text{In}_x\text{Ga}_{1-x}\text{N}$ Solar Cells with Various Indium Contents

Several single-junction solar cells were simulated using indium concentrations varying from 0.2% to 0.8%. The influence of the indium composition on the performance of $\text{In}_x\text{Ga}_{1-x}\text{N}$ single-junction solar cells was investigated to understand the operation of these solar cells better and to provide the crucial parameters and optimum efficiency for the actual fabrication of solar cells.

The energy band diagrams of $\text{In}_x\text{Ga}_{1-x}\text{N}$ single-junction solar cells with various indium compositions are presented in Figure 31a. Here, for each composition the same color is used for the conduction band edge as for the valence band edge except that it is a darker shade. Furthermore, the simulated internal quantum efficiencies (IQE) for these same cells are shown in Figure 31b where the colors for each composition match those in Figure 31a. Generally, the bandgap of each indium concentration can be obtained from the energy band diagram. As the indium content in the $\text{In}_x\text{Ga}_{1-x}\text{N}$ alloys increases, the device bandgap decreases. Starting with the lower indium content solar cell, the near UV bandgap reduces the number of photons absorbed resulting in decreasing the number of photons collected into the contacts of the cell as can be seen by the shifting cutoff to longer wavelengths in the IQE. Additionally, the output IQE for each cell shows basically that all the photons absorbed are collected in the contacts of the cells. The structure of the curve (sharp or round) is generally due to the structure of the absorption curves in Figure 30.

The operation of $\text{In}_x\text{Ga}_{1-x}\text{N}$ single-junction solar cells were investigated through the characteristic parameters including J_{sc} , V_{oc} , and η . These parameters can be obtained from the simulated J-V characteristics of $\text{In}_x\text{Ga}_{1-x}\text{N}$ as shown in Figure 32. As the indium content was increased, V_{oc} decreased, while J_{sc} increased. The V_{oc} can be affected by the bandgap

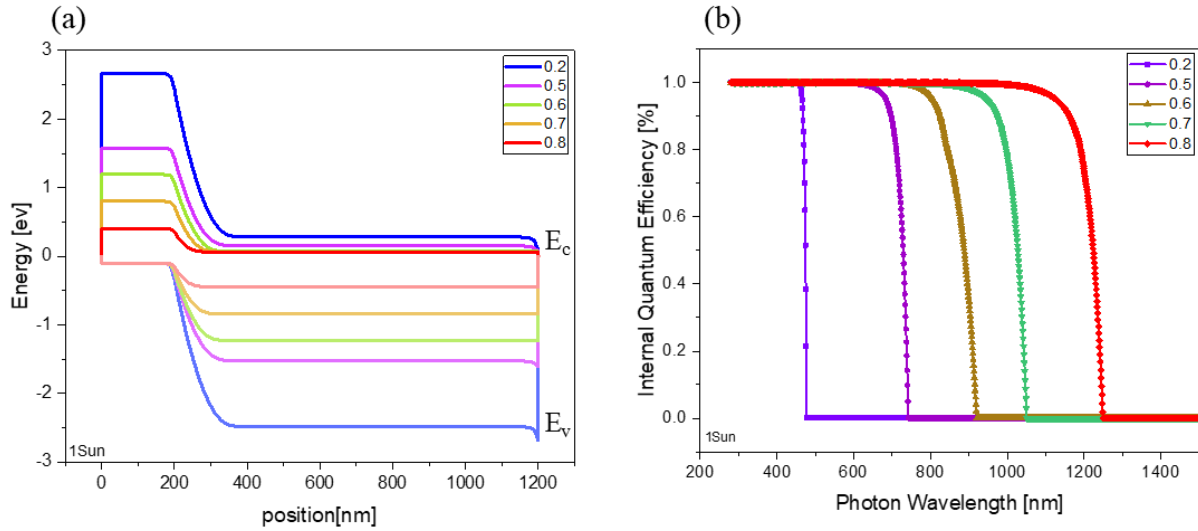


Figure 31: (a) Energy band diagrams, and (b) IQE of $\text{In}_x\text{Ga}_{1-x}\text{N}$ single-junction solar cells for various indium compositions.

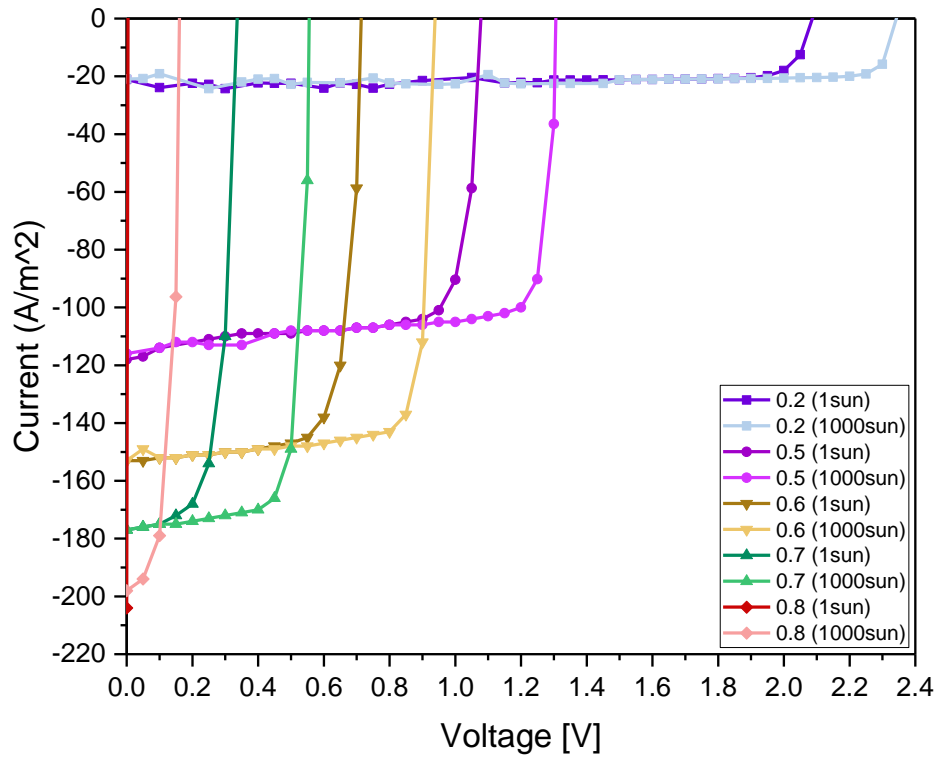


Figure 32: J-V characteristics of $\text{In}_x\text{Ga}_{1-x}\text{N}$ single-junction solar cells for different indium compositions.

energy due to the variation of the Fermi energies (ΔE_F) in the depletion region [69]. Thus, the V_{oc} is expected to decrease with the increasing indium content. According to Equation 5-3, the V_{oc} is also directly related J_{sc} , so smaller J_{sc} leads to reduced V_{oc} . The J_{sc} clearly depends on the number of absorbed photons by the solar cells. By reducing the bandgap through using more indium concentration, more photons were absorbed by the $\text{In}_x\text{Ga}_{1-x}\text{N}$ leading to higher J_{sc} . The absorption of photons can also be enhanced by higher penetration depth of infrared light. Smaller bandgap and larger penetration depth leads to the generation of more photocurrent in the solar cells with the higher indium concentrations.

Additionally, the effects of concentrating the light intensity can be seen from Figure 32. When raising the intensity of light to 1000 suns, there was no relative change in the J_{sc} for all solar cells. These concentrator curves are all divided by 1000 here. However, higher V_{oc} was found due to the logarithmic dependence on J_{sc} as found by [16]:

$$V'_{oc} = \frac{nkT}{q} \ln \left(\frac{XJ_{sc}}{I_0} \right) = \frac{nkT}{q} \left[\ln \left(\frac{J_{sc}}{I_0} \right) + \ln X \right] = V_{oc} + \frac{nkT}{q} \ln X \quad (\text{Equation 5-3})$$

where X is the light intensity.

Figure 33 shows that the conversion efficiency increases with indium content until reaching 0.5 then it decreases again. As mentioned before, when increasing the indium concentration, the absorption and the J_{sc} improve while the V_{oc} is reduced. These characteristic parameters, J_{sc} and V_{oc} , could affect the final conversion efficiency (η). Furthermore, in order to simplify the description of η , the indium content in each $\text{In}_x\text{Ga}_{1-x}\text{N}$ solar cell was divided into three categories: (a) low indium concentrations, $x = \sim 0.2$, (b) high indium concentrations, $x = 0.7$ and 0.8 , and (c) medium indium concentrations with $x = 0.5$ and 0.6 . First, in (a), the cells have very low η due to the very low J_{sc} , and similarly in (b), the cells with high indium concentrations have very low efficiency due to their very low V_{oc} . Finally, in (c), the solar cell with medium indium

contents has the highest efficiency due to the combination of both relatively high J_{sc} and V_{oc} . The $\text{In}_x\text{Ga}_{1-x}\text{N}$ solar cells with medium indium contents are optimum for high efficiency solar cells. However, phase separation in high indium content InGaN alloys has been a challenge.

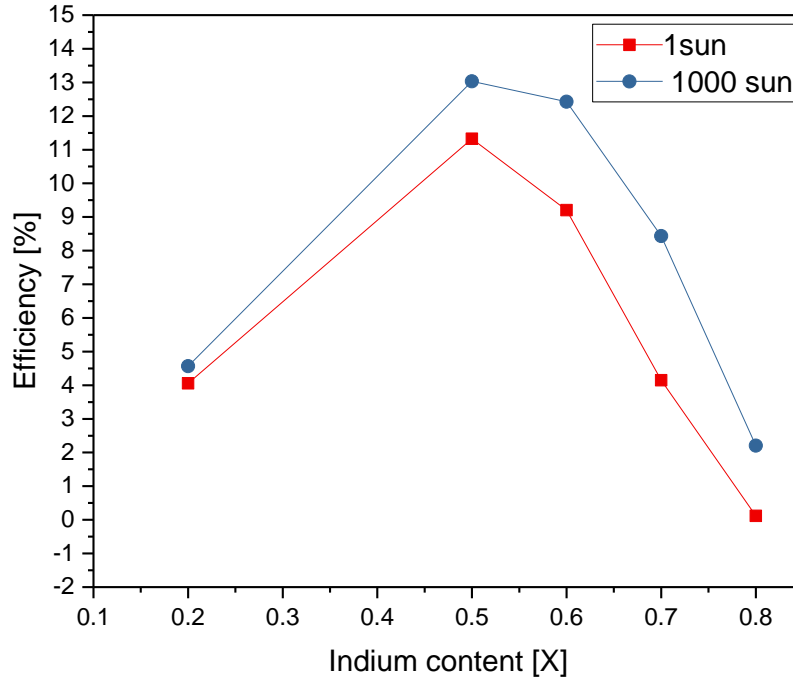


Figure 33: Efficiency versus indium content in the $\text{In}_x\text{Ga}_{1-x}\text{N}$ single-junction solar cells.

The simulations so far included strain in the InGaN layer with the assumption that the growth is strained to a GaN substrate. In reality there will be some strain relaxation, so to study the effects of the strain on solar cell performance, the $\text{In}_x\text{Ga}_{1-x}\text{N}$ single-junction solar cells with the same structure under 1sun were simulated using 0.6 and 0.8 indium contents with strain and without strain. The J-V characteristics of this simulation are shown in Figure 34. These results for both indium compositions show no change for J_{sc} while a significant improvement was found for the V_{oc} without strain. It is known that pseudomorphic, compressive, biaxial strain in the InGaN system will result in an increase in the bandgap. Therefore, the inclusion of strain should

result in higher V_{oc} and, thus, an improved efficiency in relation to the bandgaps in Figure 33. However, according to Figure 34, the efficiencies of both compositions decreased significantly with the introduction of strain. This result is not well understood at this time and will be the focus of future study.

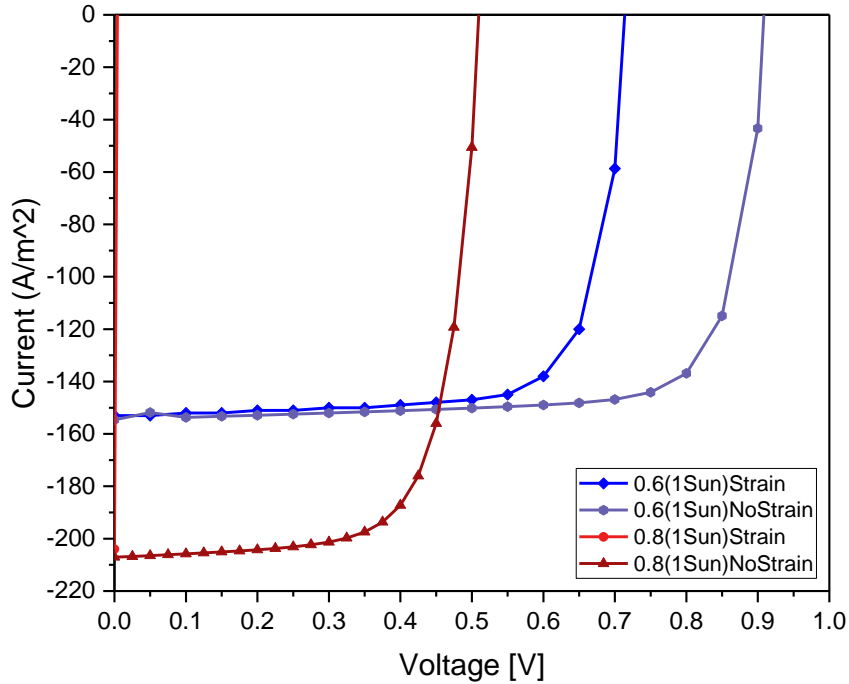


Figure 34: J-V characteristic of $\text{In}_x\text{Ga}_{1-x}\text{N}$ single-junction solar cells with and without strain.

5.4 Simulating $\text{In}_{0.5}\text{Ga}_{0.5}\text{N}$ Single-Junction Solar Cells

Since the maximum efficiencies were achieved by using $\text{In}_{0.5}\text{Ga}_{0.5}\text{N}$ (Figure 33), various $\text{In}_{0.5}\text{Ga}_{0.5}\text{N}$ single-junction solar cells were simulated in order to study the impact of the thickness of p-type region on the solar cell performance and to find the optimal thickness for p-type region. In this experiment, the thickness of p-layers was varied while the other parameters were fixed. The structure used in this simulation of $\text{In}_{0.5}\text{Ga}_{0.5}\text{N}$ single-junction solar cells is shown in Figure 35.

Figure 36 shows the energy band diagrams, J-V characteristics, and the total conversion efficiency as functions of the p-type thickness. Increasing the p-layer thickness leads to increase in the distance between the front surface of the device and the space charge region. Thus, the photogenerated carriers would have to travel for a long distance before being collected in the contact. The long distance increases the chance of being lost due to recombination, which should generally decrease the J_{sc} . This is found to be true in the output J-V characteristics of Figure 36. However, at very small thicknesses, the V_{oc} dropped suddenly, because the depletion region extended sufficiently close to the front surface affecting the efficiency by reducing the voltage required to reach flatband and, thus, the V_{oc} . On the other hand, there were some anomalies found in the simulations using $x = 0.5$, seen as the spikes at $\sim 0.2V$ in the J-V curves of the 100nm and the 300nm samples. These results need to be investigated further in order to understand the causes of these anomalies. Finally, the efficiency was found to be maximum at 100nm thickness.

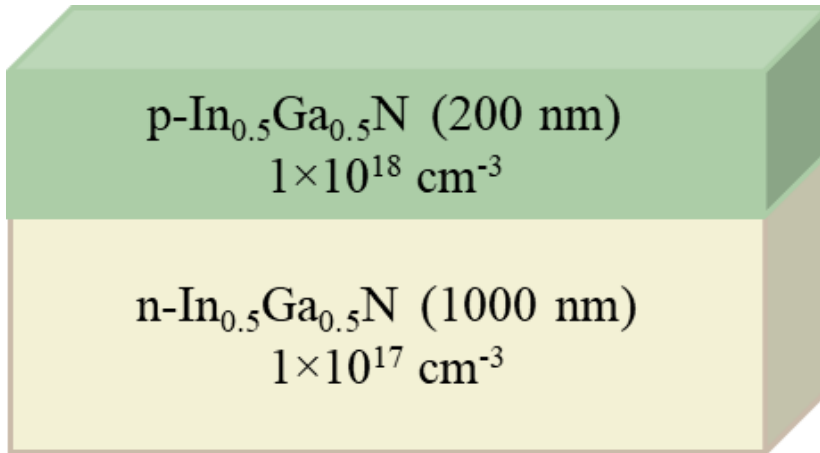


Figure 35: The reference $In_{0.6}Ga_{0.4}N$ single-junction structure.

Due to the relatively high efficiency of the $In_{0.6}Ga_{0.4}N$ device and unforeseen anomalies in

the simulations using $\text{In}_{0.5}\text{Ga}_{0.5}\text{N}$, the following studies were performed using $\text{In}_{0.6}\text{Ga}_{0.4}\text{N}$. The general trends resulting from the following variations are the interesting results and will be assumed to be similar for this range of composition even though it is understood that $\text{In}_{0.6}\text{Ga}_{0.4}\text{N}$ may not produce the absolute maximum efficiencies.

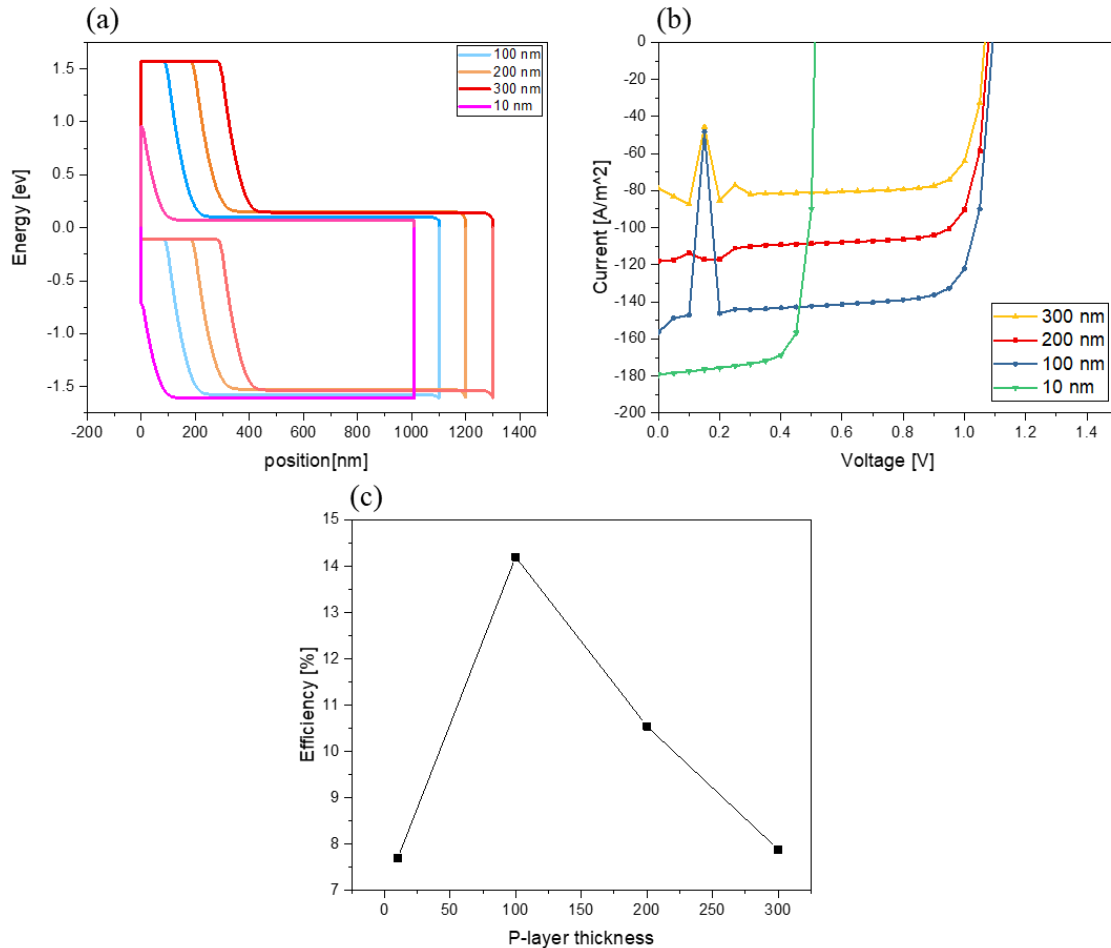


Figure 36: (a) Energy band diagrams, (b) J-V characteristics, and (c) efficiency as a function of p-type thickness.

5.5 Simulating $\text{In}_{0.6}\text{Ga}_{0.4}\text{N}$ Single-Junction Solar Cells

In this section, several $\text{In}_{0.6}\text{Ga}_{0.4}\text{N}$ single-junction solar cells were simulated. The objective of this simulation work was to uncover the trends that lead to maximizing the conversion efficiency

of single-junction InGaN solar cells and to obtain the effective structure parameters. The effects of the thickness of each layer and the doping concentration on the electrical parameters of the solar cell, including characteristic parameters J_{SC} , V_{OC} , and η , were investigated. The structure used in this simulation of $\text{In}_{0.6}\text{Ga}_{0.4}\text{N}$ single-junction solar cells within Nextnano³ (Appendix A) is shown in Figure 37.

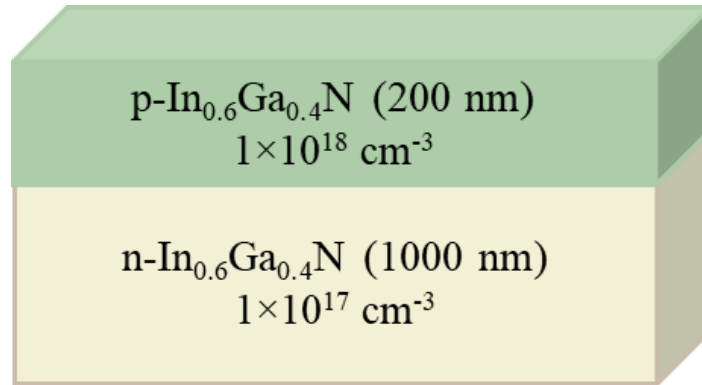


Figure 37: $\text{In}_{0.6}\text{Ga}_{0.4}\text{N}$ single-junction structure.

5.5.1 The effect of different thickness of each layer

The InGaN thickness is sufficient to absorb about 99% of the incident light. It was found that the InGaN solar cells with 300 nm of the total device thickness absorbed around 95% of the light, and about 99% for 500 nm of device thickness. Therefore, the limit of the total device thickness of InGaN solar cell is approximately 500 nm to absorb all of the incident light [4]. However, simply absorbing all the light does not necessarily lead to high efficiency. In order to study the effect of thickness on the performance of $\text{In}_{0.6}\text{Ga}_{0.4}\text{N}$ single-junction solar cells and to find the optimal thickness for each region, varying the thickness of p- and n-layers were explored.

First, the doping concentration of the n-type base was fixed at $1 \times 10^{17} \text{ cm}^{-3}$, and the

thickness was fixed at 1000 nm, while the doping concentration of the p-type emitter was fixed at $1 \times 10^{18} \text{ cm}^{-3}$. The thickness of the p-type emitter was varied between 30, 50, 100, 200, and 300 nm.

The energy band diagrams of $\text{In}_{0.6}\text{Ga}_{0.4}\text{N}$ single-junction solar cells for various p-type thicknesses are given in Figure 38a and the IQE in Figure 38b. By decreasing the p-layer thickness, the distance between the space charge region and the front surface, where the contact is, was decreased. Therefore, the photogenerated carriers have to travel a shorter distance before being collected in the contact. As a result, the carriers have less chance of recombining and being lost, which generally should lead to increased J_{SC} .

The output J-V characteristics of these cells are shown in Figure 39. When decreasing the p- $\text{In}_{0.6}\text{Ga}_{0.4}\text{N}$ top layer thickness of the solar cell, it was indeed found that J_{SC} increased. However, at very small thicknesses, the depletion region can become too close to the front surface, resulting in reduced V_{oc} and also conversion efficiency. This will be seen in later simulations.

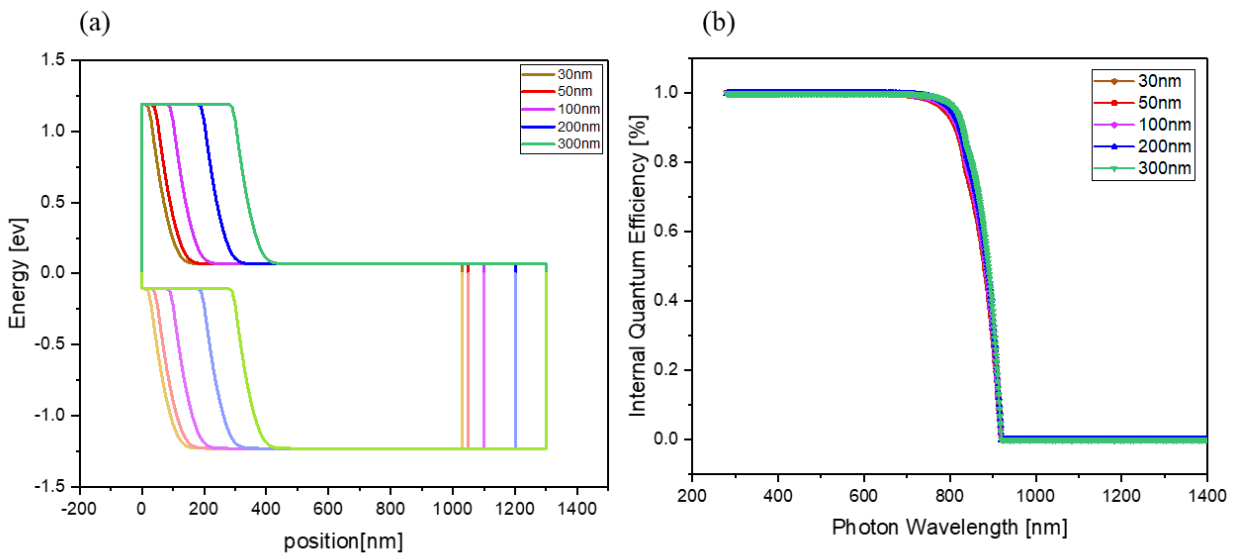


Figure 38: (a) Energy band diagrams, and (b) IQE of $\text{In}_{0.6}\text{Ga}_{0.4}\text{N}$ single-junction solar cells for various p-type thicknesses.

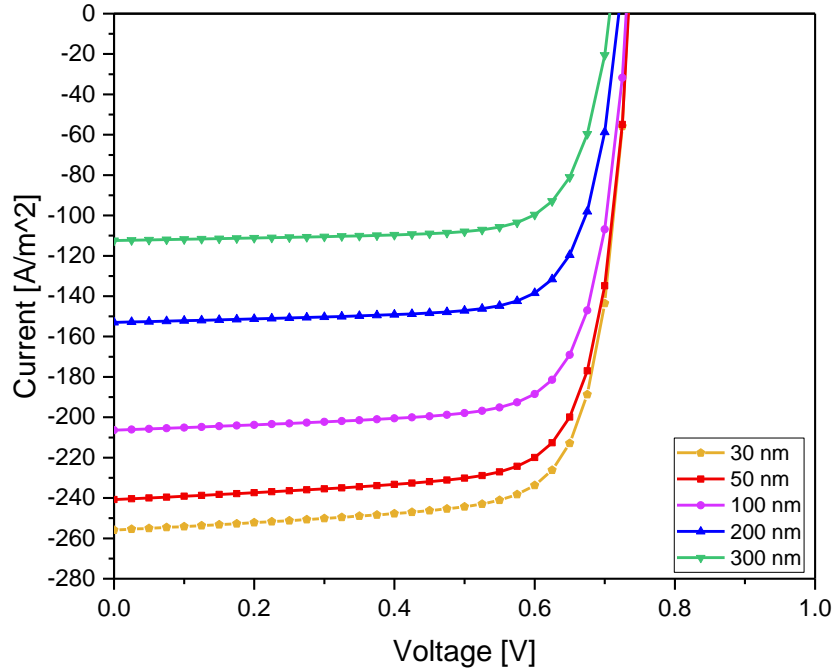


Figure 39: Output J-V characteristics of $\text{In}_{0.6}\text{Ga}_{0.4}\text{N}$ single-junction solar cells with various p-type thickness.

Next, the effects of varying the thickness of n-type base was examined. The doping concentration of the p-type emitter was fixed at $1 \times 10^{18} \text{ cm}^{-3}$ and the thickness at 200 nm while the doping concentration of the n-type base was fixed at $1 \times 10^{17} \text{ cm}^{-3}$. The thickness of the n-type base was varied between the values of 100, 500, 1000, 1500, and 2000 nm.

The energy band diagram of the resulting $\text{In}_{0.6}\text{Ga}_{0.4}\text{N}$ single-junction solar cells for various n-type thicknesses is presented in Figure 40a and the IQE in Figure 40b. Here, it was found that the general thickness of the n-type layer does not significantly affect the depletion region. The IQE shows that more total light is absorbed as the n-type thickness increases. Even though increasing the n-type thickness enhanced the absorption of the light, the collection efficiency, and generated more carriers, the very long drift length prevents the extra carriers from reaching the n-type back

contact.

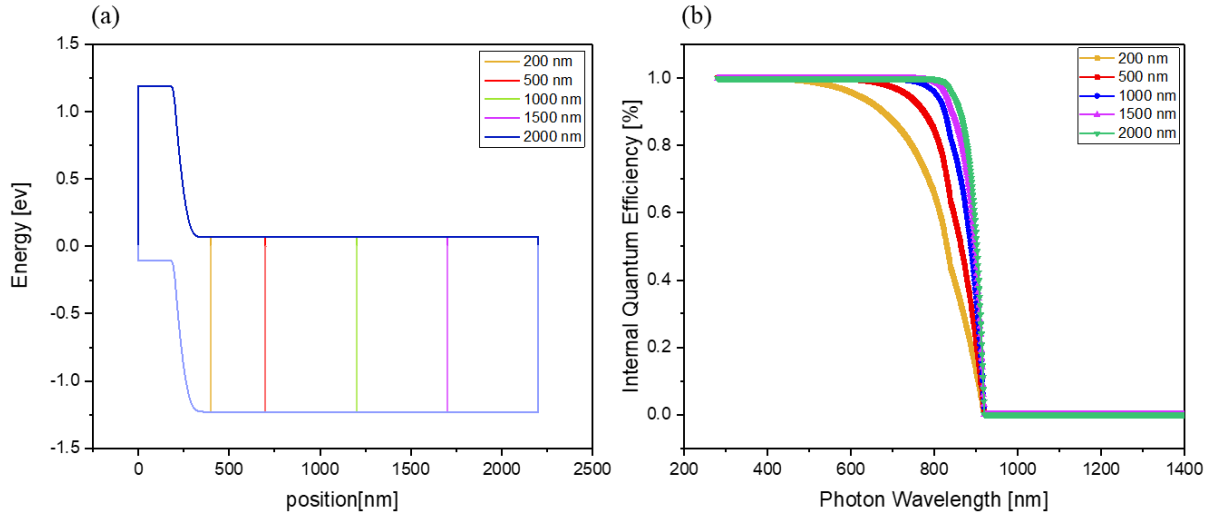


Figure 40: (a) Energy band diagrams, and (b) IQE of $\text{In}_{0.6}\text{Ga}_{0.4}\text{N}$ single-junction solar cells for various n-type thicknesses.

The output J-V characteristics of the $\text{In}_{0.6}\text{Ga}_{0.4}\text{N}$ single-junction solar cells with various n-type thicknesses are shown in Figure 41. By increasing the n-layer thickness, the J_{sc} increased until a thickness of 1000 nm then decreased. Although a thicker n-layer base enhanced the absorption and generates more carriers, most carriers would be lost before reaching the n-contact due to a longer drift length leading to the ultimate decrease of J_{sc} for too thick of an n-type layer.

The efficiency as a function of the layer thickness is shown in Figure 42. The conversion efficiency improved as the thickness increased for both regions, reached a maximum, and then dropped. The optimum efficiency was achieved for a p-type thickness of 50 nm while the n-layer attained the optimum efficiency at 1000 nm. The highest efficiency found was around 15% for 50 nm p-type layer and around 9.3% for 1000 nm n-layer. The black stars in Figure 42 represent the reference structure, i.e., that which is the same in both series. The maximum thickness of the

n-type layer should be around 1000 nm in order to generate maximum photocurrent without significant loss due to recombination.

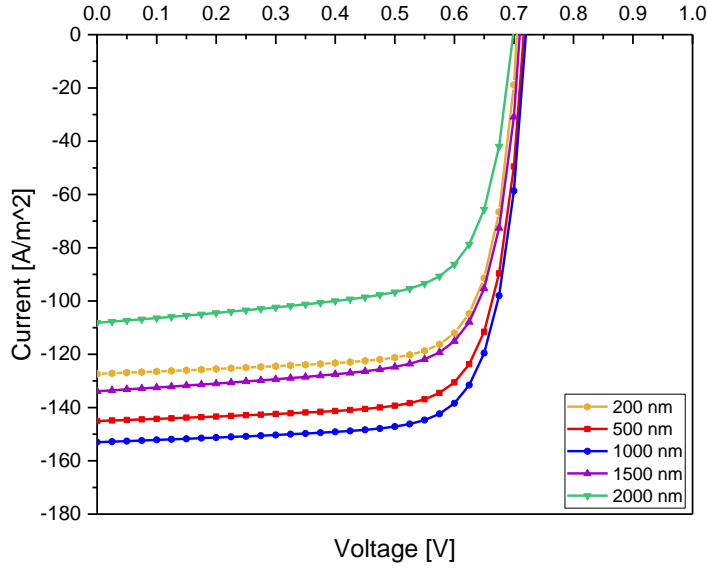


Figure 41: J-V characteristics for different n-type thicknesses of $\text{In}_{0.6}\text{Ga}_{0.4}\text{N}$ single-junction solar cells.

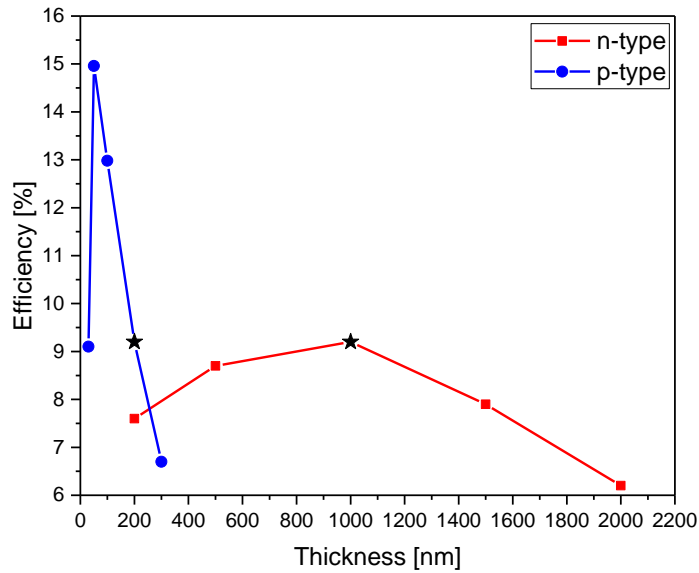


Figure 42: Efficiency as a function of thickness for different n- and p-type thicknesses of $\text{In}_{0.6}\text{Ga}_{0.4}\text{N}$ single-junction solar cells.

5.5.2 The effect of different doping concentration of each layer

First, the influence of varying the doping concentration of p-type emitter was studied. The doping concentration of the n-type base was fixed at $1 \times 10^{17} \text{ cm}^{-3}$ with a thickness of 1000 nm while the thickness of the p-type emitter was fixed at 200 nm. The doping concentration of the p-type emitter was varied between $1 \times 10^{16} \text{ cm}^{-3}$ and $1 \times 10^{20} \text{ cm}^{-3}$.

The energy band diagrams for this series of solar cells for various p-type doping concentrations are presented in Figure 43. Decreasing the doping concentration generally increased the width of the depletion region as expected which should lead to improved collection efficiency resulting from decreased loss due to recombination. However, as can be seen in Figure 43, below a concentration of $\sim 1 \times 10^{16} \text{ cm}^{-3}$ the depletion region extends all the way to the surface resulting in an obvious reduction in the required voltage to be applied to reach flat-band conditions. This should predict a drop in the V_{oc} .

Figure 44 shows the J-V characteristics of the $\text{In}_{0.6}\text{Ga}_{0.4}\text{N}$ single-junction solar cells with several doping concentrations of p-layer. Increasing the doping of the p-type layer leads to decreasing the depletion region width and increasing the “drift length” of the layer. This results in increased loss due to recombination and a lowering of the J_{sc} . Furthermore, with decreasing the doping of the p-layer, the minority carrier lifetime and the mobility of the carriers were increased leading to an improvement in the minority carrier diffusion length and also to an increase in J_{sc} . With very high doping concentration, the depletion region becomes vanishingly small leading to near zero efficiencies. However, with very low doping, a very high J_{sc} was found, but the extent of the depletion region to the surface resulted in a very small V_{oc} and again a small conversion efficiency. This indicates an interplay between the surface layer thickness and doping concentration in these cell structures. Finally, for the highest concentration, $1 \times 10^{20} \text{ cm}^{-3}$,

an inverted current condition resulted. This is an anomaly included for completeness and needs to be investigated further. However, it is believed to be due to the near degenerate doping of the p-type layer here and inversion of the Fermi level and the valence band edge.

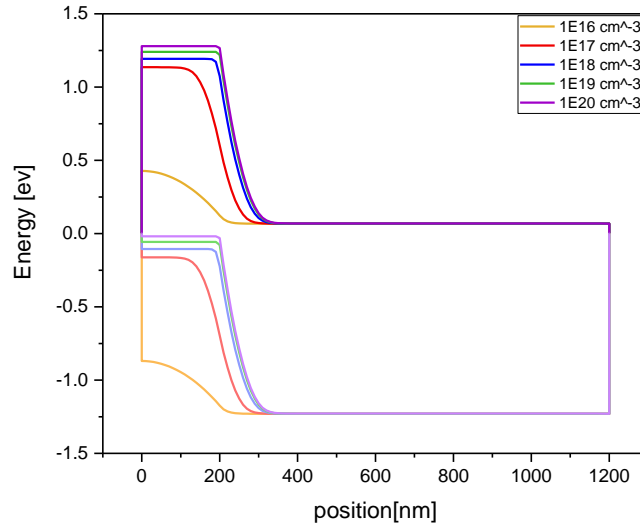


Figure 43: Energy band diagrams of $\text{In}_{0.6}\text{Ga}_{0.4}\text{N}$ single-junction solar cells for different p-type doping levels.

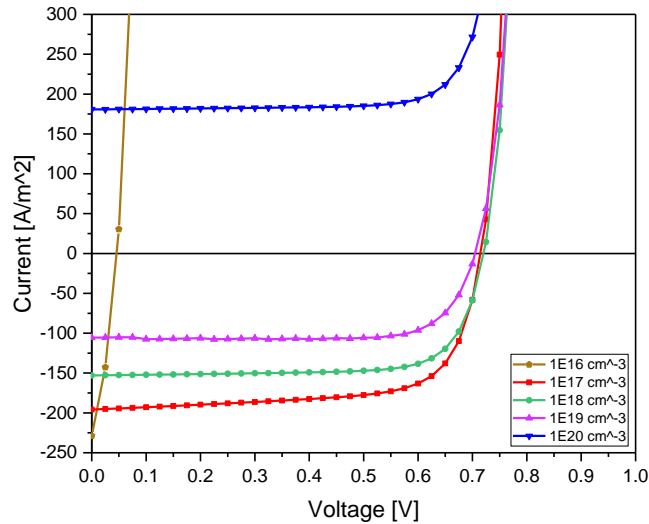


Figure 44: J-V characteristics of $\text{In}_{0.6}\text{Ga}_{0.4}\text{N}$ single-junction solar cells with several p-doping levels.

Next, the effect of n-type doping concentration on the $\text{In}_{0.6}\text{Ga}_{0.4}\text{N}$ single-junction solar cells performance was examined. The energy band diagrams of this series are presented in Figure 45. The doping concentrations of the n-layer showed a significant impact on the depletion width. Decreasing the doping concentration of the n-layer again increased the width of the depletion region. Similar to before, it is expected that increasing this length will increase the current due to decreased loss due to recombination in the drift layer.

The J-V characteristics for this series of InGaN solar cells is given in Figure 46. As expected, similar to the p-type case, decreasing the doping of the n-type base leads to an increase in the J_{sc} resulting from the extension of the depletion region and the high electron diffusion length. Similar to the p-type layer results, the extremely low doping concentrations result in the depletion region extending all the way to the back contact and ultimately reducing V_{oc} .

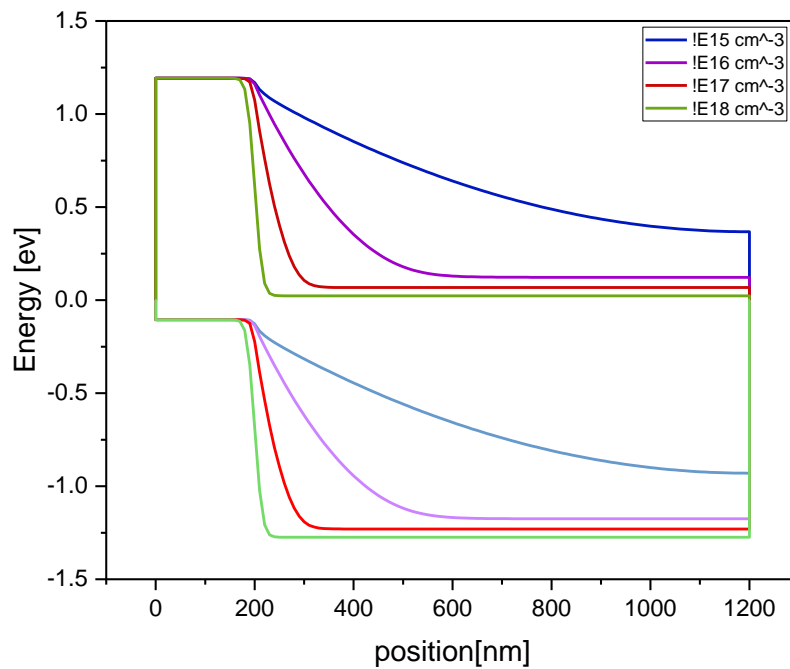


Figure 45: Energy band diagrams of $\text{In}_{0.6}\text{Ga}_{0.4}\text{N}$ single-junction solar cells for several n- doping levels.

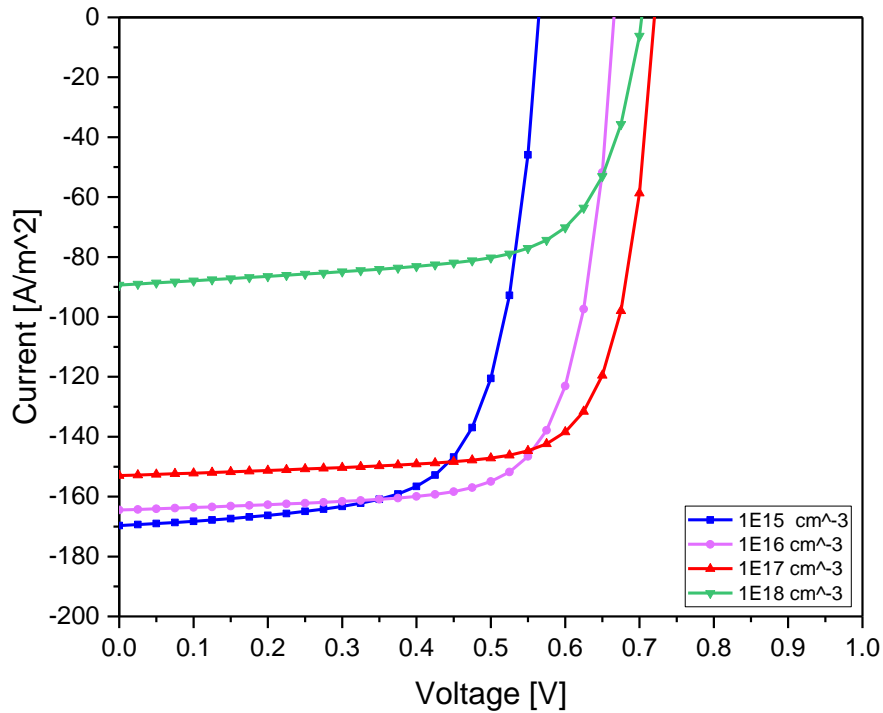


Figure 46: J-V characteristics for several levels of n-type doping of the $\text{In}_{0.6}\text{Ga}_{0.4}\text{N}$ solar cells.

To conclude this set of simulation experiments, the efficiency as a function of the doping concentration is summarized in Figure 47. The conversion efficiency was improved by increasing the doping concentrations of both n- and p-layers to some maxima and then decreased with further increase in doping. The highest efficiency achieved was around 12% for $1 \times 10^{17} \text{ cm}^{-3}$ p-type layer and around 9.3% for $1 \times 10^{17} \text{ cm}^{-3}$ n-layer. The black stars, again denote the reference structure.

5.5.3 Using optimal thickness with different doping

In order to maximize the conversion efficiency, the optimal thickness of the p-n junction, 50 nm for the p-type upper region and 1000 nm for n-region, were used. The doping concentration

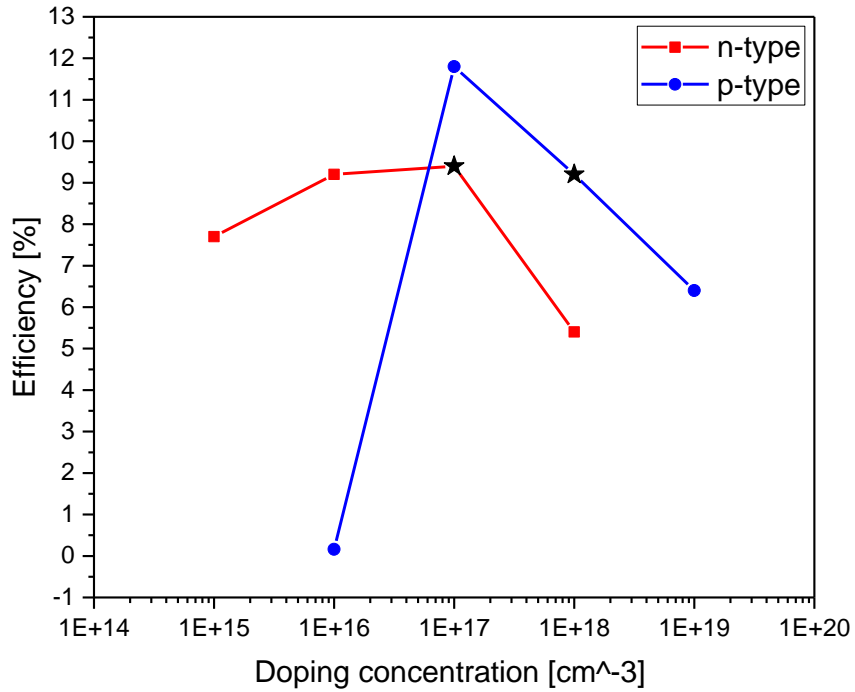


Figure 47: Efficiency as a function of doping concentrations for several p- and n-type doping of the $\text{In}_{0.6}\text{Ga}_{0.4}\text{N}$ solar cells.

of n-type region was fixed at $1 \times 10^{17} \text{ cm}^{-3}$, and the variation with p-type doping concentration was studied again.

In Figure 48, the energy band diagrams, J-V characteristics, and the total conversion efficiency as a function of p-type doping concentration, using the optimal thickness are presented. Generally, the same trends are found as before with variations of the doping concentration. The J_{sc} decreases, while the V_{oc} increases, with increasing doping concentration. Here, the highest efficiency found is around 15.2% for a $1 \times 10^{18} \text{ cm}^{-3}$ p-type layer.

In summary, by comparing between the efficiencies at different doping and thickness of p- and n-layers, the best design of the $\text{In}_{0.6}\text{Ga}_{0.4}\text{N}$ single-junction solar cells can be obtained. From Figure 49, the optimal thickness of p-type emitter is found to be 50 nm with $1 \times 10^{18} \text{ cm}^{-3}$ doping

concentration, and 1000 nm for the n-type base with $1 \times 10^{17} \text{ cm}^{-3}$ doping concentration. However, the interplay between these parameters still needs to be completely understood. By using the optimal thicknesses of both regions, the p-type doping experiments were rerun, and their result, which is the curve with the light red stars, shows significant improvement in the efficiency.

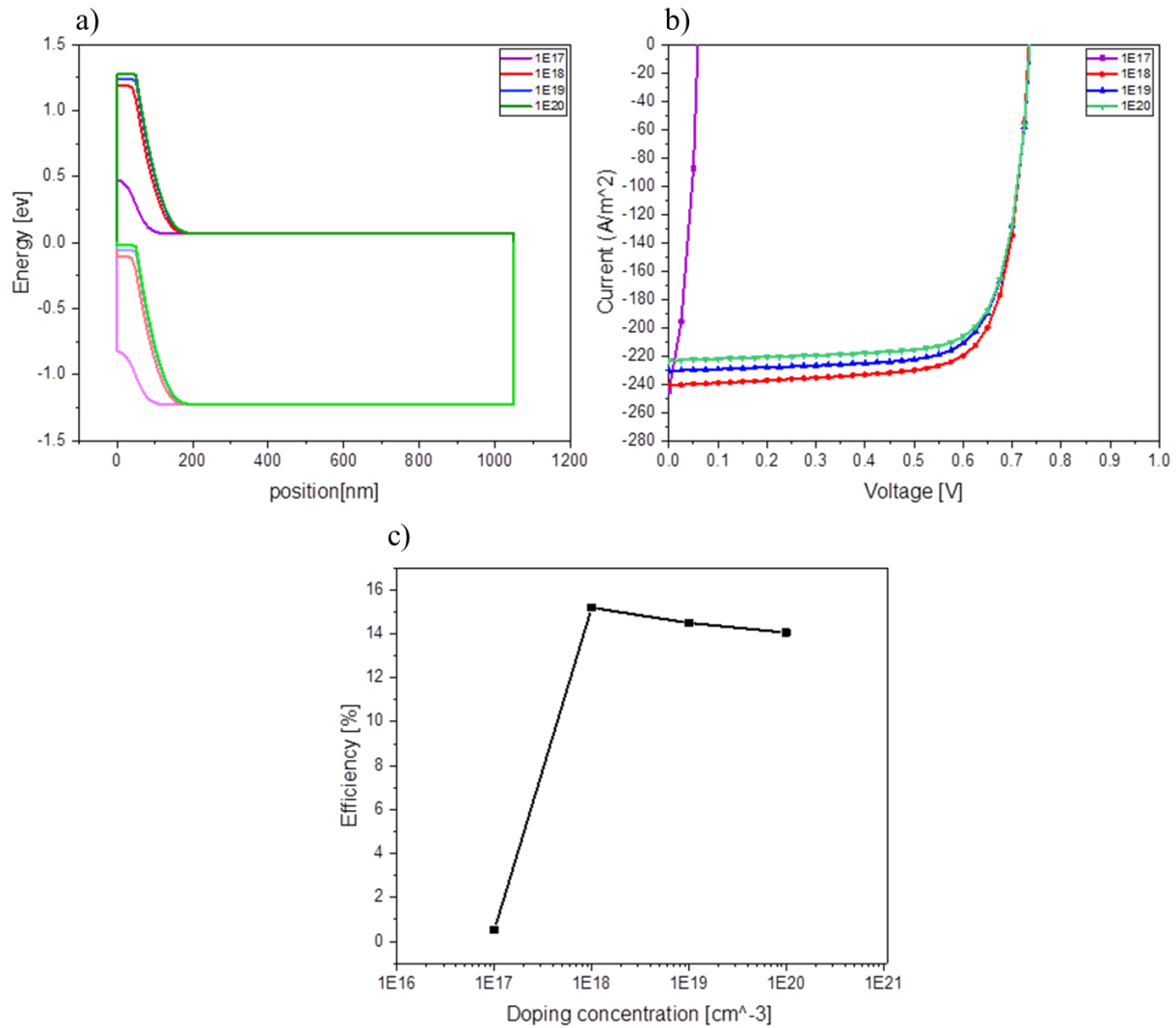


Figure 48: (a) Energy band diagrams, (b) J-V characteristics, and (c) efficiency as a function of doping concentrations using optimal thickness.

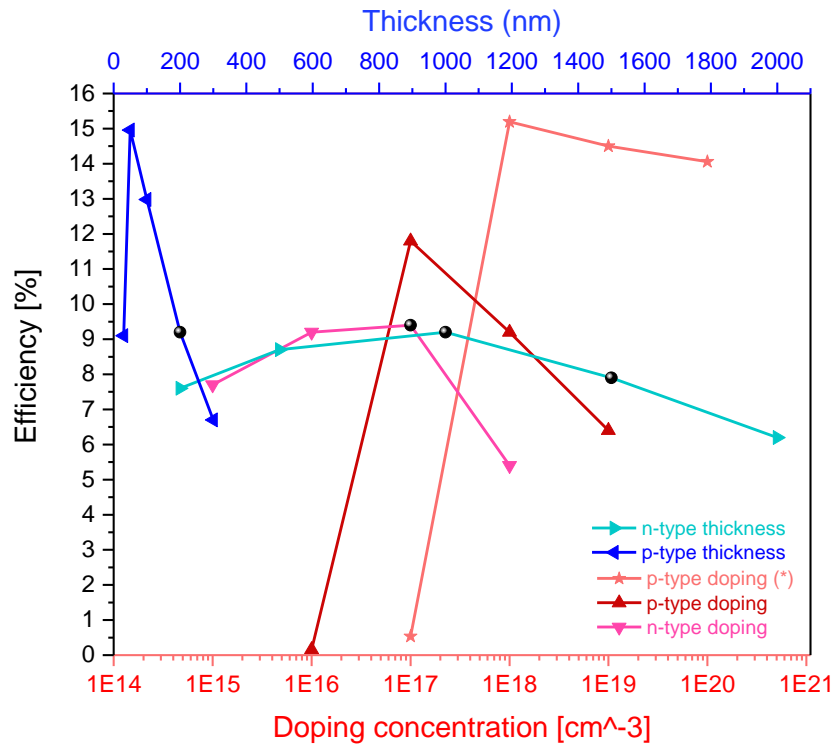


Figure 49: Efficiency as a function of thickness and doping concentration of single-junction $\text{In}_{0.6}\text{Ga}_{0.4}\text{N}$ solar cells.

5.6 Simulating $\text{In}_{0.6}\text{Ga}_{0.4}\text{N}$ p-i-n Solar Cells

In this section, $\text{In}_{0.6}\text{Ga}_{0.4}\text{N}$ p-i-n solar cells were simulated to understand the trends which lead to maximum conversion efficiency with the use of an intrinsic i-region between the p-region and n-region. The general reason for using an i-region is to maximize the effective thickness of the depletion region in order to enhance the absorption in the depletion region. The bandgap of 1.44 eV was again chosen, and the effects of the thickness of each layer and the doping concentration on the characteristic parameters including J_{sc} , V_{oc} , and η , were investigated.

The structure used in this simulation of $\text{In}_{0.6}\text{Ga}_{0.4}\text{N}$ p-i-n homojunction solar cells is shown in Figure 50. This structure was adapted from Reference 53 using the InGa_N composition as roughly optimized above. Furthermore, the strain was addressed in all experiments in this

section. For reference, the thickness of the upper p-type region was chosen to be 10 nm with $5 \times 10^{17} \text{ cm}^{-3}$ of doping concentration, and the thickness of n-type base was chosen to be 10 nm with $5 \times 10^{17} \text{ cm}^{-3}$ of the doping concentration. The thickness of undoped i-layer was 200 nm.

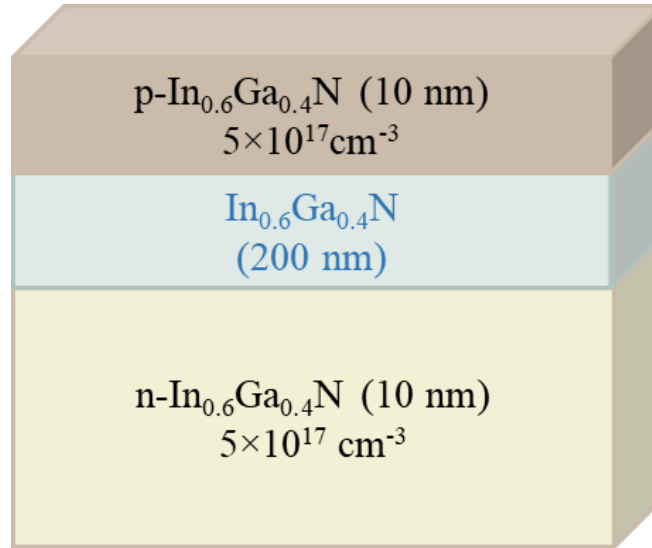


Figure 50: Structure of the $\text{In}_{0.6}\text{Ga}_{0.4}\text{N}$ p-i-n homojunction solar cell.

5.6.1 The effect of varying the thickness of i-region

In this simulation, the i-region was varied between 50, 100, 300, 400, 500, 600, 800, and 1000 nm in order to find its optimal thickness.

Figure 51 shows (a) the band diagrams, and (b) the IQE of different i-layer thickness in the p-i-n solar cells. The IQE obtained shows that as the thickness of the i-layer increased, the total amount of light absorbed increased due to the finite thickness of the cell. For the thinnest designs, there should be a substantial amount of light transmitted through the entire sample without absorption. The thicker i-layer can absorb more photons with appropriate energy leading to increasing the photo-generated current.

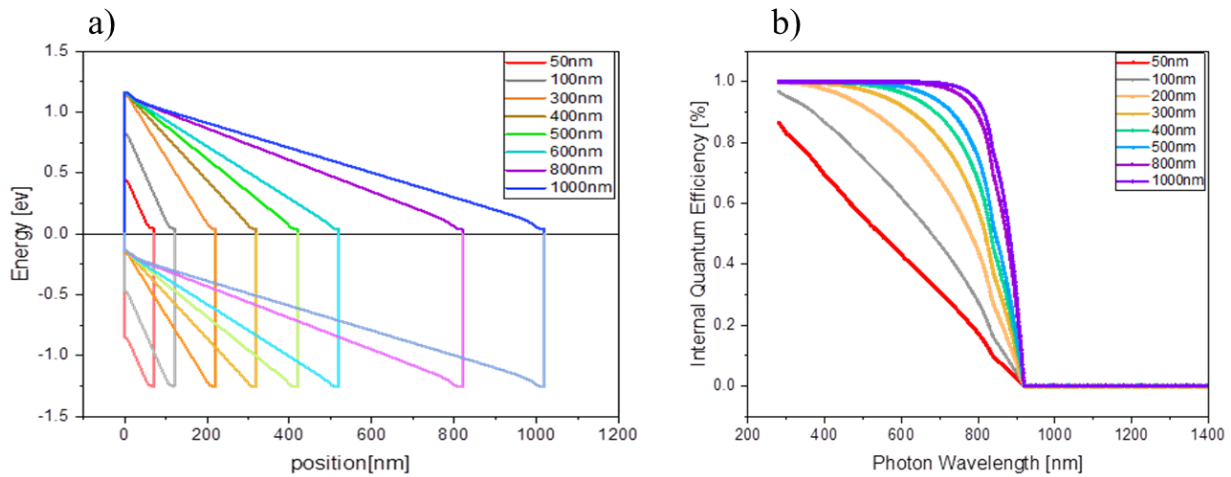


Figure 51: (a) Band diagrams and (b) IQE for different i-layer thickness in the p-i-n structure.

The J-V characteristics for this series are presented in Figure 52. Increasing the i-layer thickness maximized the absorption of photons leading to increasing the photo-generated current and J_{sc} . However, the V_{oc} goes through some maximum at 200 nm. For higher i-layer thicknesses, the built-in electric field in the longer depletion region must decay slightly due to a small background n-type doping concentration which is included in the simulations. This ultimately leads to the small decrease in V_{oc} with increasing thickness. On the other hand, as the thickness decreases from ~200 nm, a significant fraction of the light passes through the back of the cell leading to significant reductions in both J_{sc} and V_{oc} .

Figure 53 presents the efficiency as a function of i-layer thickness in p-i-n solar cells. The efficiency increases with the i-layer thickness until 400 nm and then remains nearly constant as both the J_{sc} and V_{oc} change in the background. The highest efficiency achieved is around 13.2% for a 400 nm i-layer.

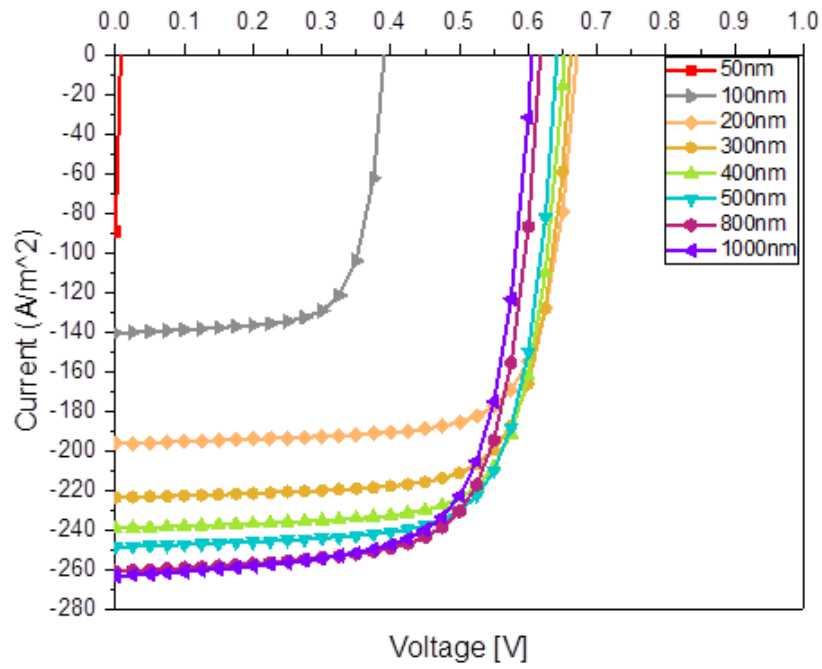


Figure 52: J-V characteristics for varied i-layer thickness in p-i-n solar cells.

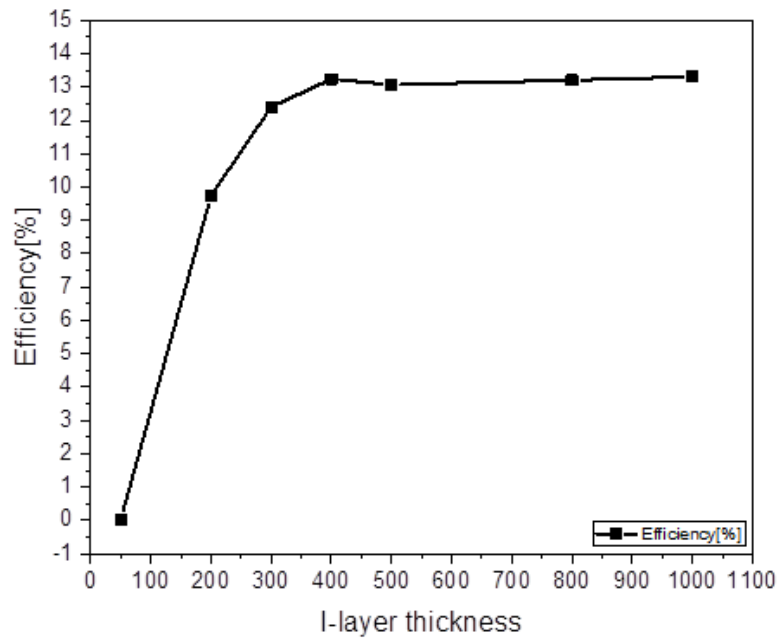


Figure 53: Efficiency of p-i-n solar cells as a function of i-layer thickness.

5.6.2 The effect of varying the thickness of n-layer

The optimal thickness of i-layer was fixed at 400 nm in this experiment. Also, the thickness of upper p-type region was fixed at 10 nm with $5 \times 10^{17} \text{ cm}^{-3}$ doping, and the n-type base was fixed at $5 \times 10^{17} \text{ cm}^{-3}$ doping. The thickness of n-type base was then varied between 10, 30, 50, 100, 150, 200, 400, 500, and 1000 nm.

Figure 54 shows the results of this experiment including the energy band diagrams, IQE, J-V curves, and the efficiency achieved for each n-type thickness. As noted before in the InGaN single-junction solar cells, the IQE shows that more light is absorbed as the n-type thickness increases. Even with this variation in absorption with smaller n-type thickness, the depletion region was able to generate significant photocurrent. However, the smallest thicknesses did ultimately reduce the collection efficiency and then reduce the minority carrier diffusion length leading to smaller J_{sc} . The J-V curves shows that increasing the n-type thickness slightly increased the J_{sc} until reaching 400 nm then dropping again. The optimal thickness was found to be 400 nm with 13.9% efficiency.

5.6.3 The effect of varying the thickness of p-layer

In order to find the optimal efficiency, the optimal thicknesses for n-region (400 nm) and i-region (400 nm) were used and fixed. The doping concentrations for p- and n-regions were fixed at $5 \times 10^{17} \text{ cm}^{-3}$. The p-type thickness was changed between 2, 5, 10, 30, 50, and 100 nm (Figure 55).

The results of this simulation (Figure 55) show similar responses as in p-n junction InGaN solar cells. The efficiency improved with increasing the p-type thickness until reaching 10 nm, then decreased. For the smallest thickness, the band offset at the front contact was lowered, again due to the depletion reaching through the p-type layer, resulting in lower V_{oc} . Therefore, the

thickness of p-type top layer in the p-i-n solar cell should be as thin as possible without being completely depleted at ultra-thin values. The best thickness achieved for p-type layer was 10 nm.

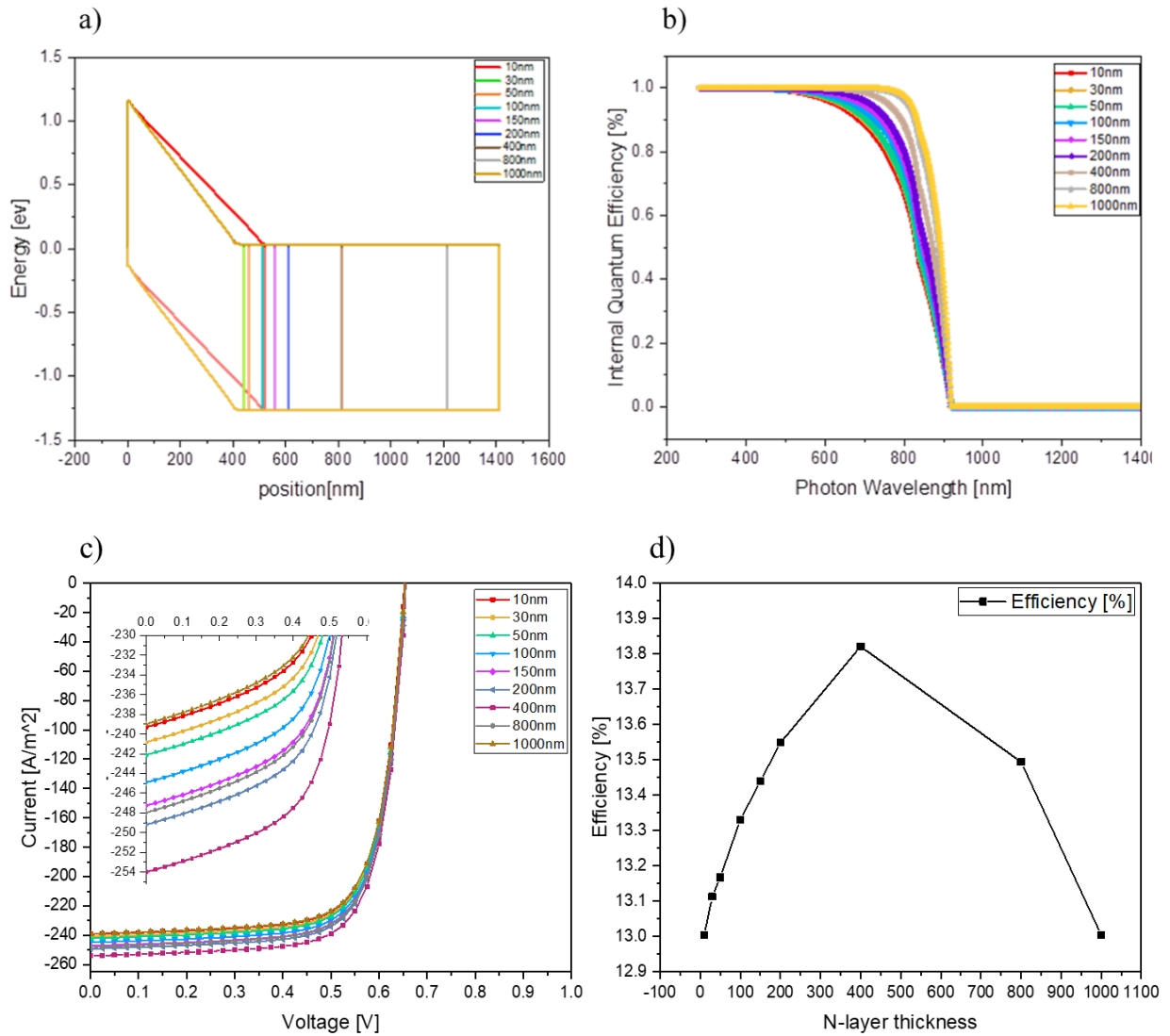


Figure 54: (a) Energy band diagrams, (b) IQE, (c) J-V curves, and (d) the efficiency vs. n-type thickness for p-i-n solar cells using different n-type thickness.

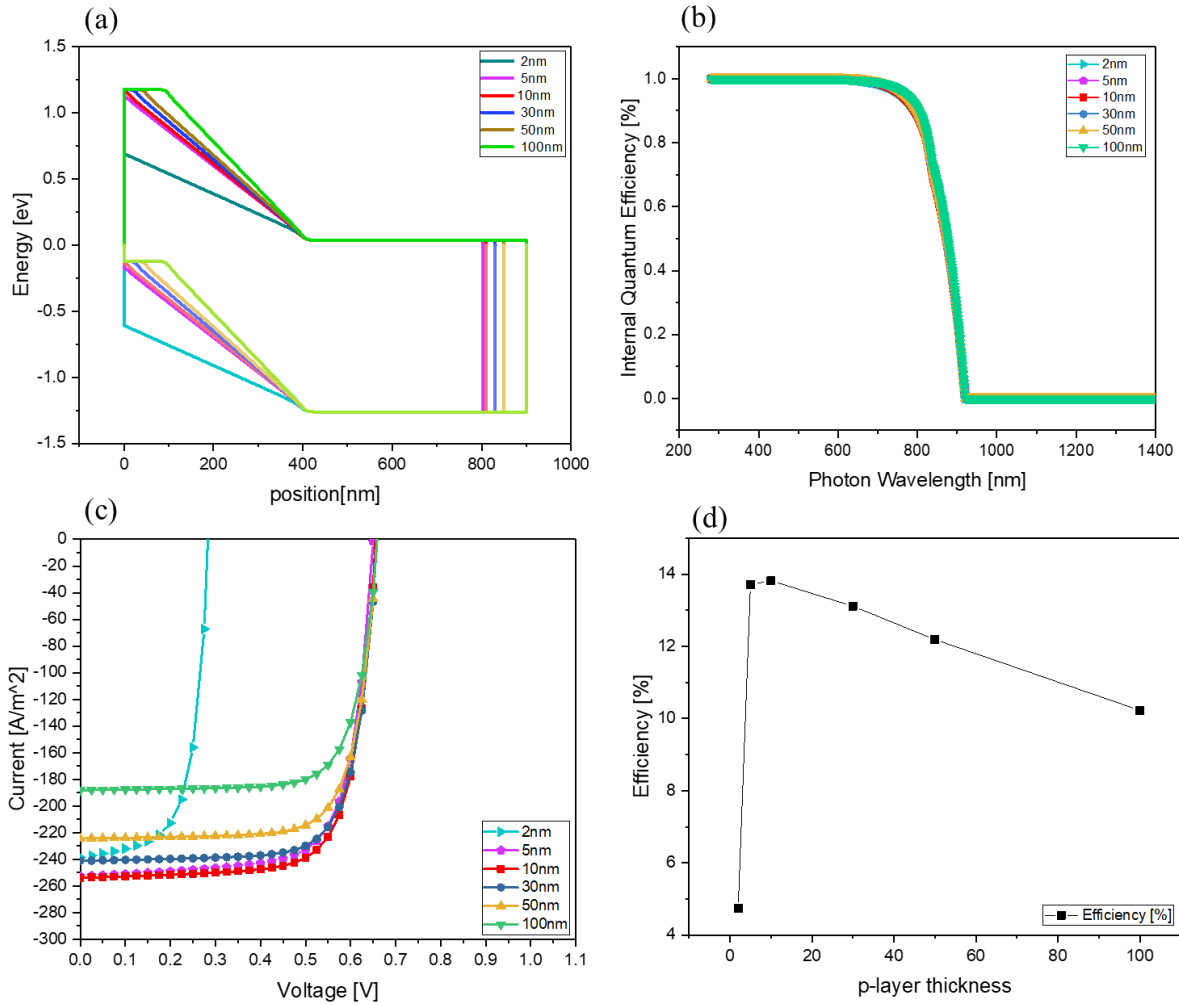


Figure 55: (a) Energy band diagram, (b) IQE, (c) J-V curves, and (d) the efficiency vs. different p-type thickness for p-i-n solar cells.

5.6.4 The effect of varying the doping concentration of p-layer

Here, the best thickness of the three regions was used and fixed at 10 nm for the p-type top region, 400 nm for the i-region, and 400 nm for the n-region, and the doping concentration of n-region was set at $5 \times 10^{17} \text{ cm}^{-3}$, all resulting from the previous experiments. Then, the doping concentration of the p-region was varied between 5×10^{17} , 5×10^{18} , 5×10^{19} , 5×10^{20} , and $5 \times 10^{22} \text{ cm}^{-3}$ (Figure 56).

The results of varying p-type doping are presented in Figure 56. Here, it is shown that varying the p-type doping concentration exhibited an insignificant effect on all of the parameters in the p-i-n InGaN solar cells due to the small thickness of the layer. As should be in a well-designed solar cell, most of the incident light passes through the p-region and is absorbed in the i-region. The efficiency rises slightly with the p-type doping concentration until $5 \times 10^{20} \text{ cm}^{-3}$ and then decreases, most likely due to increased scattering in the layer as the current can be seen to decrease slightly at this doping level in Figure 56c. The ideal doping concentration reached for the p-layer was $5 \times 10^{20} \text{ cm}^{-3}$ with 14.16% efficiency.

5.6.5 The effect of varying doping concentration of n-layer

Finally, in this simulation, the thickness was set at 10 nm p-type top region, 400 nm i-region, 400 nm n-region, and p-type doping was set at $5 \times 10^{20} \text{ cm}^{-3}$. The n-type doping was varied between 5×10^{15} , 5×10^{16} , 5×10^{17} , and $5 \times 10^{18} \text{ cm}^{-3}$.

In Figure 57, the n-type doping concentration shows only a slight impact on the J_{sc} in the p-i-n InGaN solar cells, even for the lowest concentration. The J_{sc} decreased as the n-type doping concentration increased, similar to before, due to the increased depletion region and, as a result, the reduced loss due to recombination in the bottom drift layer. The efficiency improved as the n-type doping concentration decreased reaching a maximum of 14.3% at $5 \times 10^{17} \text{ cm}^{-3}$.

In conclusion, by comparing the efficiencies at different doping levels and thicknesses of the p- and n-layers, the best design of the $\text{In}_{0.6}\text{Ga}_{0.4}\text{N}$ p-i-n junction solar cells can be obtained. From Figure 58, the optimal thickness of p-type emitter was found to be 10 nm with $5 \times 10^{20} \text{ cm}^{-3}$ doping concentration, and 400 nm for the n-type base with $5 \times 10^{17} \text{ cm}^{-3}$ doping concentration. The best thickness of the undoped i-region was 400 nm from Figure 59. In the p-i-n homojunction solar cells, the i-region can be used to maximize the depletion region and to

enhance the absorption. This structure can overcome some effects such as the leakage currents and the flat band which limit the simple p-n junction design.

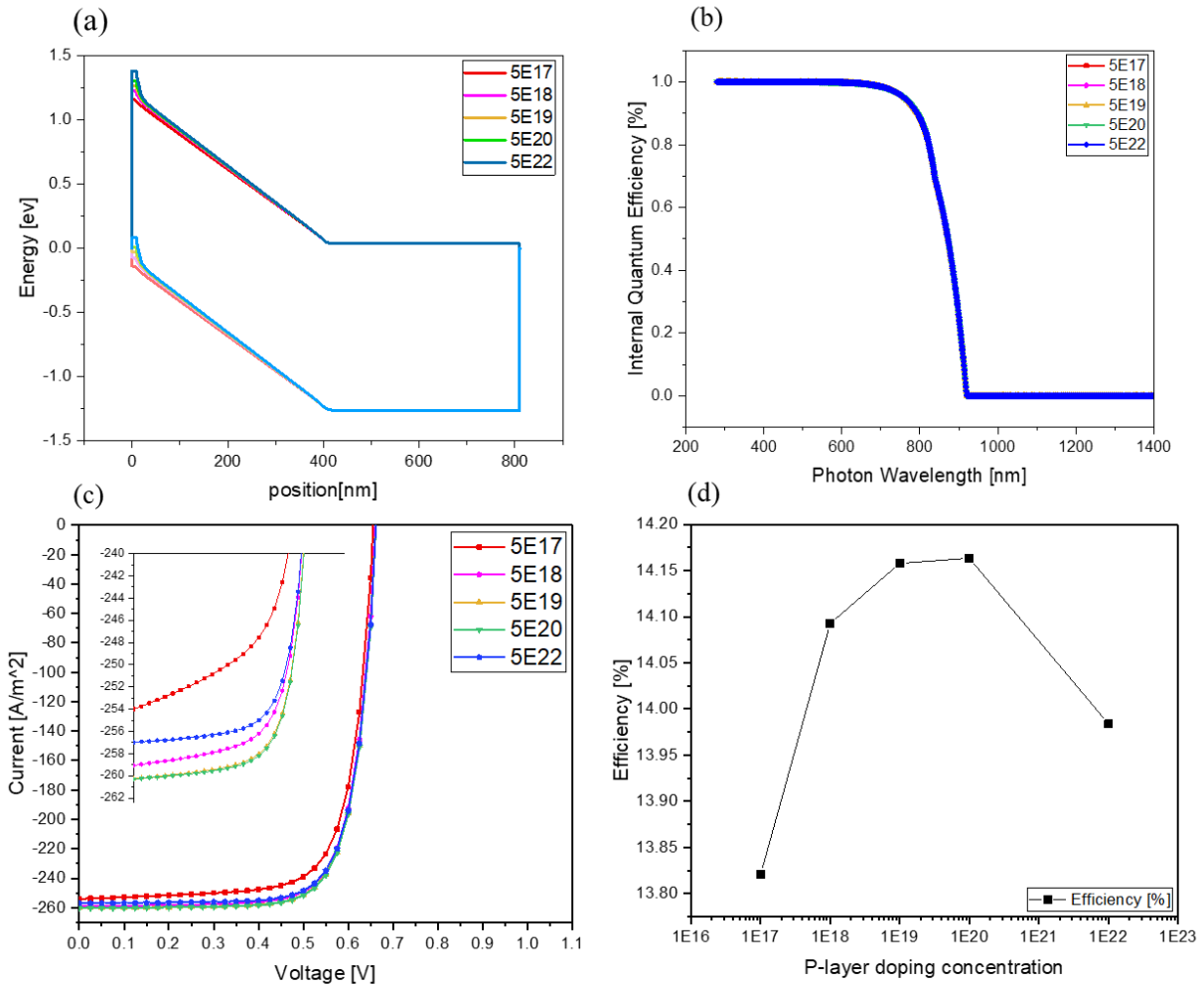


Figure 56: (a) Energy band diagrams, (b) IQE, (c) J-V curves, and (d) the efficiency vs. p-type doping for p-i-n solar cells.

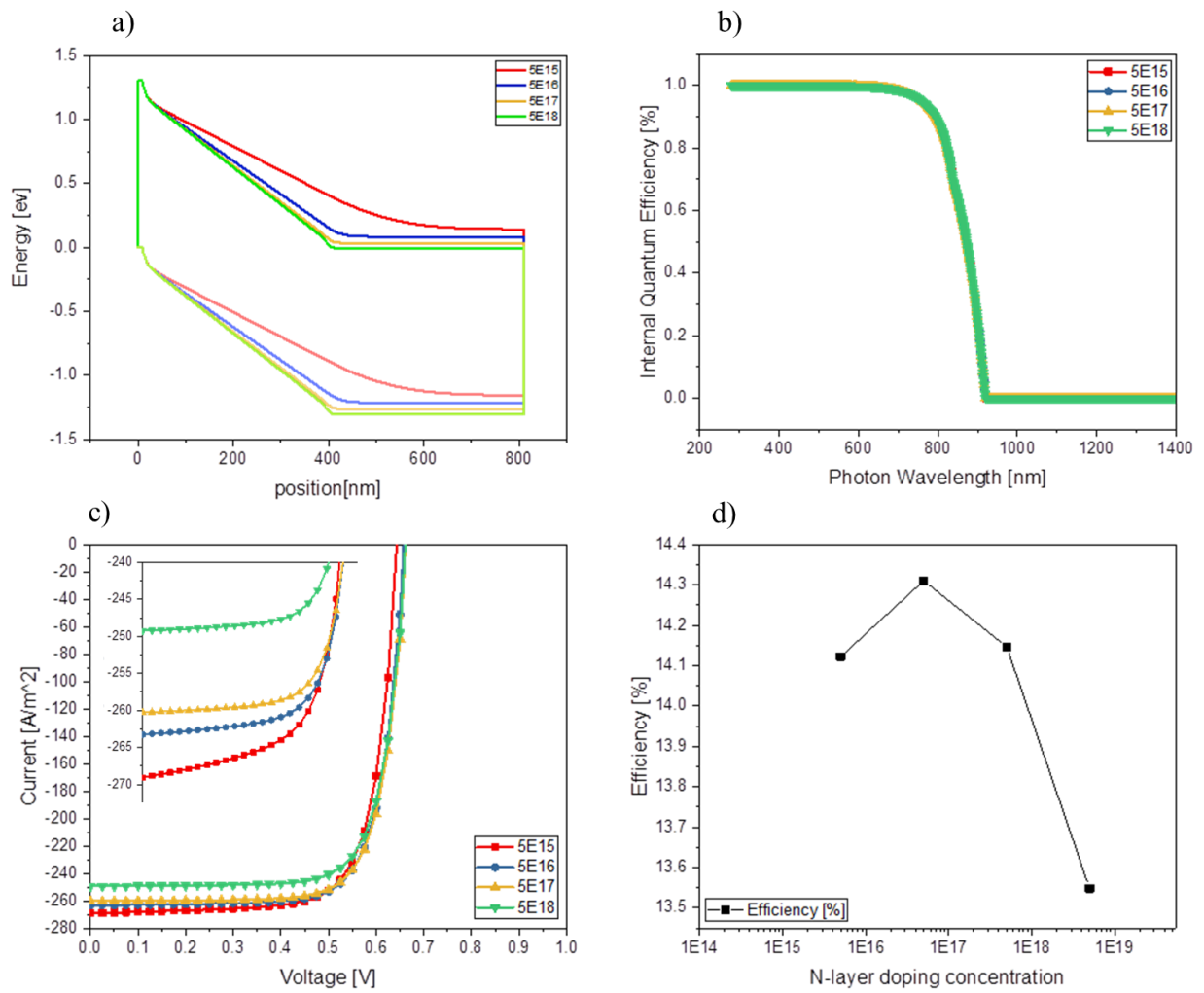


Figure 57: (a) Energy band diagrams, (b) IQE, (c) J-V curves, and (d) the efficiency vs. n-type doping for p-i-n solar cells.

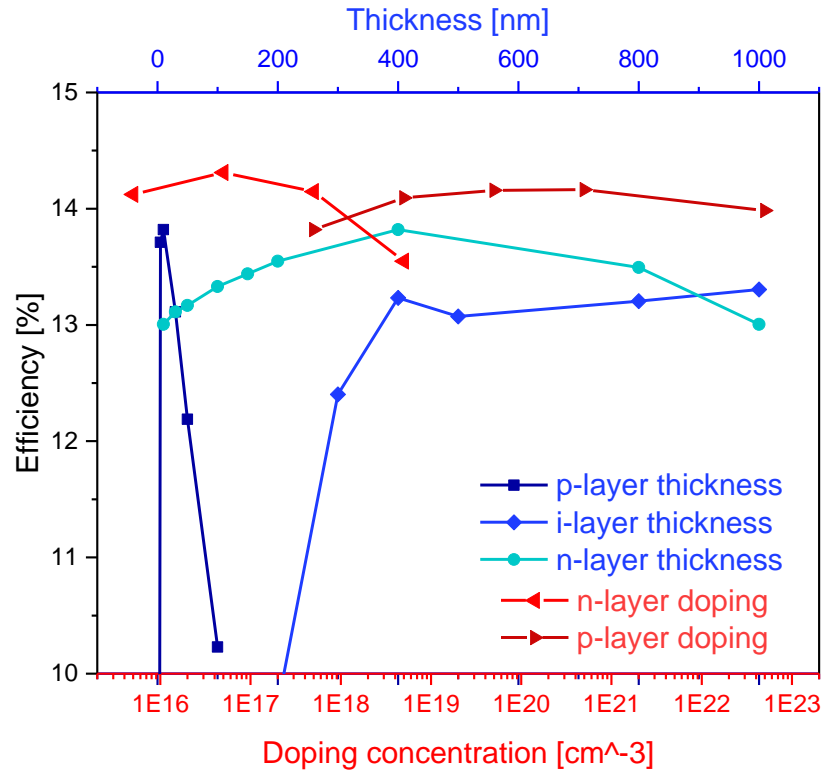


Figure 58: Efficiency versus thickness and doping concentration for p-i-n solar cells.

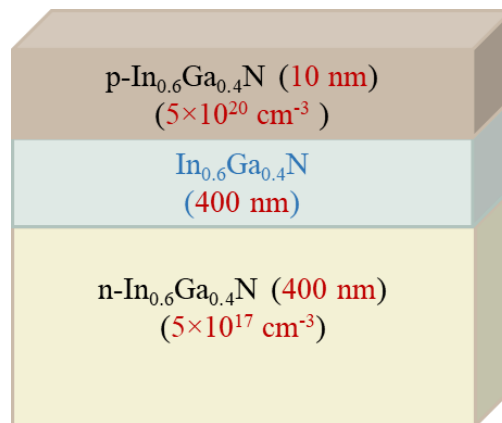


Figure 59: Optimal structure for p-i-n homojunction solar cells.

Chapter 6: Conclusions and Future Work

The comparison between Nextnano³ and PC1D successfully demonstrates that the modeling and simulating specifically for solar cells is acceptable. Therefore, the output results of the two simulators, as well as of the fundamental drift-diffusion equations, are acceptably similar. The simulation results of the simple p-n junction Si solar cell demonstrate the feasibility of using Nextnano³ software for solar cell simulation. Hence, the next objective was to use Nextnano³ software to simulate III-nitride-based solar cells.

Simulation of III-nitride solar cells was broken down into three main experiments. First, single-junction $\text{In}_x\text{Ga}_{1-x}\text{N}$ solar cells with various indium contents, where it was found that the $\text{In}_x\text{Ga}_{1-x}\text{N}$ single-junction solar cell with middle ranges of indium contents showed the highest efficiencies of the presented solar cells due to the combined electrical effects of middle ranged J_{sc} and V_{oc} . For single-junction devices with varying bandgap, an $\text{In}_{0.6}\text{Ga}_{0.4}\text{N}$ device with bandgap of 1.44 eV was found to be the optimum. The second main experiment was to enhance the $\text{In}_{0.6}\text{Ga}_{0.4}\text{N}$ single-junction solar cell performance. The best parameters were found to be 50 nm for the p-type emitter with $1 \times 10^{18} \text{ cm}^{-3}$ doping concentration, and 1000 nm for n-type base with $1 \times 10^{17} \text{ cm}^{-3}$ doping concentration. The efficiency reached with this structure was 15.2%. However, the strain from the use of a GaN substrate was not extensively understood. The final experiment was to simulate $\text{In}_{0.6}\text{Ga}_{0.4}\text{N}$ p-i-n solar cells to obtain the optimum structure parameters. The aim of this simulation was to maximize the conversion efficiency through the use of an intrinsic i-region between the p- and n-regions. The optimal thickness here for the p-type emitter was found to be 10 nm with $5 \times 10^{20} \text{ cm}^{-3}$ doping concentration, and for n-type base was found to be 400 nm with $5 \times 10^{17} \text{ cm}^{-3}$ doping concentration. The thickness of undoped i-region was 400 nm. The maximum efficiency of this design was 14.3%.

Ultimately, the 15.2% maximum efficiency of the p-n junction device was the maximum resulting from a thicker p-type layer. As such, there are still hidden relationships between the possible parameters of these structures which could be addressed using formal “design of experiments” techniques.

Future Work

The future work will be modeling and simulating of novel solar cell device structures based on InGaN/GaN multiple quantum wells (MQWs) and other novel nanostructured designs using Nextnano software package for which it is optimally designed.

References

- [1] A. J. W. I. Allison, N.L. Bindoff, R.A. Bindenschadler, P.M. Cox, N. de Noblet, M.H. England, J.E. Francis, N. Gruber, A.M. Haywood, D.J. Karoly, G. Kaser, C. Le Quéré, T.M. Lenton, M.E. Mann, B.I. McNeil, A.J. Pitman, S. Rahmstorf, E. Rignot, H.J. Schellnhuber, S.H, "The Copenhagen Diagnosis: Updating the World on the Latest Climate Science," Sydney, Australia, 2009.
- [2] J. Goldenberg and T. B. Johansson, "World Energy Assesment Overview 2004," pp. 14-16, 2004.
- [3] K. Tanabe, "A review of ultrahigh efficiency III-V semiconductor compound solar cells: Multijunction tandem, lower dimensional, photonic up/down conversion and plasmonic nanometallic structures," *Energies*, vol. 2, no. 3, pp. 504–530, 2009.
- [4] O. K. Jani, "Development of Wide-Band Gap InGaN Solar Cells for High-Efficiency Photovoltaics," Georgia Institute of Technology, pp. 10-25. 2008.
- [5] N. S. Lewis, G. Crabtree, A. J. Nozik, M. R. Wasielewski, and P. Alivisatos, "Basic Research Needs for Solar Energy Utilization," U.S. Department of Energy, Washington, DC, URL: www.er.doe.gov/bes/reports/abstracts.html#SEU, pp. 276, 2005.
- [6] E. Martinot, M. Lisa, R. Lyle, S. Paul, and L. Philippe, "Global Status Report 2006 Update," *Ren21*, pp. 20, 2006.
- [7] M. A. Green, Y. Hishikawa, W. Warta, E. D. Dunlop, D. H. Levi, J. H. Ebinger, and A. W. H. Baillie, "Solar cell efficiency tables (version 50)," *Prog. Photovoltaics Res. Appl.*, vol. 25, no. 7, pp. 668–676, 2017.
- [8] M. T. Kibria, A. Ahammed, S. M. Sony, and F. Hossain, "A Review : Comparative studies on different generation solar cells technology," *Int. Conf. Environ. Asp. Bangladesh*, pp. 51–53, 2014.
- [9] G. Conibeer, "Third-generation photovoltaics," *Materials Today*, vol. 10, no. 11. Elsevier Ltd, pp. 42–50, 2007.
- [10] M. A. Green, "Third generation photovoltaics: Ultra-high conversion efficiency at low cost," *Prog. Photovoltaics Res. Appl.*, vol. 9, no. 2, pp. 123–135, 2001.
- [11] R.R. King, D.C. Law, K.M. Edmondson, C.M. Fetzer, G.S. Kinsey, H. Yoon, R.A. Sherif, and N.H. Karam, "40% efficient metamorphic GaInP/GaInAs/Ge multijunction solar cells," *Appl. Phys. Lett.*, vol. 90, no. 18, pp. 90–93, 2007.
- [12] A. G. Bhuiyan, A. Hashimoto, and A. Yamamoto, "Indium nitride (InN): A review on growth, characterization, and properties," *J. Appl. Phys.*, vol. 94, no. 5, pp. 2779–2808, 2003.
- [13] J. Wu, "When group-III nitrides go infrared: New properties and perspectives," *J. Appl. Phys.*, vol. 106, no. 1, pp 13-29, 2009.
- [14] A. Trellakis, Z. Tobias, A. Till, B. Stefan, S. Kent, M. Richard, V. Peter, "The 3D nanometer device project nextnano: Concepts, methods, results," *J. Comput. Electron.*, vol. 5, no. 4, pp. 285–289, 2006.
- [15] D. A. Clugston and P. A. Basore, "PC1D version 5: 32-bit solar cell modeling on personal computers," in *Conference Record of the Twenty Sixth IEEE Photovoltaic Specialists*

- Conference - 1997, 1997, pp. 207–210.*
- [16] J. Nelson, "The Physics of Solar Cells", World Scientific Publishing Co Inc, pp. 153-165, 2003.
- [17] C. J. Neufeld, "Design , Fabrication and Characterization of III-N Based Solar Cells," University of California, pp. 22-38, 2011.
- [18] M. A. Green, *Solar cells: Operating principles, technology, and system applications*. Cliffs, NJ: Prentice-Hall, Englewood, pp. 25-39, 1982.
- [19] "Solar Spectral Irradiance: ASTM G-173." [Online]. Available: <http://rredc.nrel.gov/solar/spectra/am1.5/ASTMG173/ASTMG173.html>. [Accessed: 09-Nov-2017].
- [20] J. R. Lang, "Growth and Physics of III-N Based Solar Cells by Ammonia Molecular Beam Epitaxy," University of California, pp. 14-31, 2012.
- [21] N. Georgoulas, L. Magafas, and A. Thanailakis, "A study of a-SiC/c-Si(n) Isotype Heterojunctions," *Act. Passiv. Electron. components*, vol. 16, no. 1, pp. 55–64, 1993.
- [22] "Chapter 4: LED basics: Electrical properties." [Online]. Available: <https://www.ecse.rpi.edu/~schubert/Light-Emitting-Diodes-dot-org/chap04/chap04.htm>. [Accessed: 09-May-2017].
- [23] F. King, R.R., Bhusari, D., Boca, A., Larrabee, D., Liu, X.-Q., Hong, W. and N. H. C.M., Law, D.C. & Karam, "Band gap-voltage offset and energy production in next-generation multijunction solar cells," *Prog. Photovoltaics Res. Appl.*, vol. 19, no. 7, pp. 797–812, 2010.
- [24] M. A. Green, "Accuracy of analytical expressions for solar cell fill factors.," *Sol. Cells*, vol. 7, no. 3, pp. 332–349, 1982.
- [25] Green, *Solar cells: Operating principles, technology, and system applications*. pp. 85-98, 1982.
- [26] "Quantum Efficiency," *PV Education*. [Online]. Available: <http://www.pveducation.org/pvcdrom/quantum-efficiency>. [Accessed: 01-Jan-2017].
- [27] "Solar Cell Conversion-efficiency Limits," *Solar Cells*, <http://aerostudents.com/files/solarCells/CH5SolarCellConversionEfficiencyLimits.pdf>. [Accessed: 09-May-2017]. p. 5.1-5.12.
- [28] D. Boqun, "Modeling and Simulation of InAs / GaAs Quantum Dot Solar Cells in SILVACO TCAD," The George Washington University, pp.13-38, 2014.
- [29] J. Zhao, A. Wang, M. A. Green, and F. Ferrazza, "19.8% Efficient 'Honeycomb' Textured Multicrystalline and 24.4% Monocrystalline Silicon Solar Cells," *Appl. Phys. Lett.*, vol. 73, no. 14, pp. 1991–1993, 1998.
- [30] C. B. Honsberg, J. E. Cotter, K. R. McIntosh, S. C. Pritchard, B. S. Richards, and S. R. Wenham, "Design Strategies for Commercial Solar Cells Using the Buried Contact Technology," *IEEE Trans. Electron Devices*, vol. 46, no. 10, pp. 1984–1992, 1999.
- [31] E. D. Jackson, "Solar Energy Converter," US patent, 2,949,498, 1960.
- [32] A. Luque and A. Martí, "Increasing the Efficiency of Ideal Solar Cells by Photon Induced

- Transitions at Intermediate Levels,” *Phys. Rev. Lett.*, vol. 78, no. 26, pp. 5014–5017, 1997.
- [33] K. W. J. Barnham and G. Duggan, “A new Approach to High-Efficiency Multi-band-gap Solar Cells,” *J. Appl. Phys.*, vol. 67, no. 7, pp. 3490–3493, 1990.
- [34] K. W. J. Barnham, B. Braun, J. Nelson, M. Paxman, C. Button, J. S. Roberts, C. T. Foxon, “Short-circuit Current and Energy Efficiency Enhancement in a Low-Dimensional Structure Photovoltaic Device,” *Appl. Phys. Lett.*, vol. 59, no. 1, pp. 135–137, 1991.
- [35] A. Mukhtarova, “InGaN / GaN Multiple Quantum Wells for Photovoltaics,” Université Grenoble Alpes, pp.1-38, 2015.
- [36] J. Wu, W. Walukiewicz, K. M. Yu, Shan, W. Ager, J. W. Haller, E. E. Lu, H. Schaff, W. J. Metzger, K. Sarah, “Superior radiation resistance of In_{1-x}Ga_xN alloys: Full-solar-spectrum photovoltaic material system,” *J. Appl. Phys.*, vol. 94, no. 10, pp. 6477–6482, 2003.
- [37] A. G. Bhuiyan, K. Sugita, A. Hashimoto, and A. Yamamoto, “InGaN solar cells: Present state of the art and important challenges,” *IEEE J. Photovoltaics*, vol. 2, no. 3, pp. 276–293, 2012.
- [38] "Full-spectrum Solar Cell." [Online]. Available: <http://emat-solar.lbl.gov/?tmpl=%2Fsystem%2Fapp%2Ftemplates%2Fprint%2F&showPrintDialog=1>. [Accessed: 12-Dec-2017].
- [39] M. R. Krames, O. B. Shchekin, M. Regina, O. Z Gerd, H Ling, C. Gerard, M. George., “Status and future of high-power light-emitting diodes for solid-state lighting,” *IEEE/OSA J. Disp. Technol.*, vol. 3, no. 2, pp. 160–175, 2007.
- [40] J. Wu, W. Walukiewicz, K. M. Yu, J. W. Ager, E. E. Haller, H. Lu, W. J. Schaff, “Small band gap bowing in In_{1-x}Ga_xN alloys,” *Appl. Phys. Lett.*, vol. 80, no. 25, pp. 4741–4743, 2002.
- [41] K. Shen, T. Wang, D. Wu, and R. Horng, “High thermal stability of high indium content InGa_N films grown by pulsed laser deposition,” *Opt. Express*, vol. 20, no. 14, pp. 15149–56, 2012.
- [42] L. A. Vilbois, A. Cheknane, A. Bensaoula, C. Boney, and T. Benouaz, “Simulation of a solar cell based on InGa_N,” *Energy Procedia*, vol. 18, pp. 795–806, 2012.
- [43] C. J. Lu, L. A. Bendersky, H. Lu, and W. J. Schaff, “Threading dislocations in epitaxial In_N thin films grown on (0001) sapphire with a Ga_N buffer layer,” *Appl. Phys. Lett.*, vol. 83, no. 14, pp. 2817–2819, 2003.
- [44] D. Holec, Y. Zhang, D. V. S. Rao, M. J. Kappers, C. McAleese, and C. J. Humphreys, “Equilibrium critical thickness for misfit dislocations in III-nitrides,” *J. Appl. Phys.*, vol. 104, no. 12, 2008.
- [45] I. H. Kim, H. S. Park, Y. J. Park, and T. Kim, “Formation of V-shaped pits in InGa_N/Ga_N multiquantum wells and bulk InGa_N films,” *Appl. Phys. Lett.*, vol. 73, no. 12, pp. 1634–1636, 1998.
- [46] I. Ho and G. Stringfellow, “Solid phase immiscibility in GaIn_N,” *Appl. Phys. Lett.*, vol. 69, no.18, pp. 2701-2703, 1996.

- [47] K. W. J. Barnham and G. Duggan, "A new approach to high-efficiency multi-band-gap solar cells," *J. Appl. Phys.*, vol. 67, no. 7, pp. 3490–3493, 1990.
- [48] H. P. Maruska and J. J. Tietjen, "The preparation and properties of vapor-deposited single-crystal-line GaN," *Appl. Phys. Lett.*, vol. 15, no. 10, pp. 327–329, 1969.
- [49] P. Perlin, T. Suski, H. Teisseyre, M. Leszczynski, I. Grzegory, J. Jun, S. Porowski, P. Bogusławski, J. Bernholc, J. C. Chervin, A. Polian, T. D. Moustakas, "Towards the identification of the dominant donor in GaN," *Phys. Rev. Lett.*, vol. 75, no. 2, pp. 296–299, 1995.
- [50] D. Iida, M. Iwaya, S. Kamiyama, H. Amano, and I. Akasaki, "Activation energy of Mg in a $-plane Ga_{1-x}In_xN$ ($0 < x < 0.17$)," *Phys. Status Solidi*, vol. 246, no. 6, pp. 1188–1190, 2009.
- [51] S. Strite, "GaN, AlN, and InN: A review," *J. Vac. Sci. Technol. B Microelectron. Nanom. Struct.*, vol. 10, no. 4, p. 1237, 1992.
- [52] S. Yamasaki, S. Asami, N. Shibata, M. Koike, K. Manabe, T. Tanaka, H. Amano, I. Akasaki, "p-type conduction in Mg doped $Ga_{0.91}In_{0.09}N$ grown by metalorganic vapor phase epitaxy," *Appl. Phys. Lett.*, vol. 66, no. 9, pp. 1112–1113, 1995.
- [53] K. Kumakura, T. Makimoto, and N. Kobayashi, "High hole concentrations in Mg-doped InGaN grown by MOVPE," *J. Cryst. Growth*, vol. 221, no. 1–4, pp. 267–270, 2000.
- [54] H. K. Cho, T. Hossain, J. W. Bae, and I. Adesida, "Characterization of Pd/Ni/Au ohmic contacts on p-GaN," *Solid. State. Electron.*, vol. 49, no. 5, pp. 774–778, 2005.
- [55] J.-K. Ho, C.-S. Jong, C. C. Chiu, C.-N. Huang, C.-Y. Chen, and K.-K. Shih, "Low-resistance ohmic contacts to p-type GaN," *Appl. Phys. Lett.*, vol. 74, no. 9, pp. 1275–1277, 1999.
- [56] M. E. Lin, F. Y. Huang, and H. Morkoç, "Nonalloyed ohmic contacts on GaN using InN/GaN short-period superlattices," *Appl. Phys. Lett.*, vol. 64, no. 19, pp. 2557–2559, 1994.
- [57] S. Birner, T. Zibold, T. Andlauer, T. Kubis, M. Sabathil, A. Trellakis, P. Vogl, "nextnano : General Purpose 3-D Simulations," vol. 54, no. 9, pp. 2137–2142, 2007.
- [58] S. Birner, S. Hackenbuchner, and M. Sabathil, "Modeling of Semiconductor Nanostructures with nextnano³," *Acta Phys. Pol. A*, vol. 110, no. 2, pp. 111–124, 2006.
- [59] "Nextnano." [Online]. Available: <http://www.nextnano.de/products/products.php>. [Accessed: 13-Sep-2017].
- [60] P. Ellinghaus, "Simulation of GaN/AlGaIn heterostructures for a HEMT simulator," University of L'aquila, pp. 1-50, 2011.
- [61] T. Andlauer, "Optoelectronic and spin-related properties of semiconductor nanostructures in magnetic fields," Technical University of Munich, 2009.
- [62] T. Zibold, "Semiconductor based quantum information devices : Theory and simulations," Technical University of Munich, 2007.
- [63] H. Haug, A. Kimmerle, J. Greulich, A. Wolf, and E. Stensrud Marstein, "Implementation of Fermi–Dirac statistics and advanced models in PC1D for precise simulations of silicon solar cells," *Sol. Energy Mater. Sol. Cells*, vol. 131, pp. 30–36, 2014.

- [64] K. Wang and I. Perez-Wurfl, "A method to overcome the time step limitation of PC1D in transient excitation mode," *Energy Procedia*, vol. 55, pp. 155–160, 2014.
- [65] A. Deinega and S. John, "Finite difference discretization of semiconductor drift-diffusion equations for nanowire solar cells," *Comput. Phys. Commun.*, vol. 183, no. 10, pp. 2128–2135, 2012.
- [66] M. Mehta, "Modifying PC1D to Model Spontaneous & Piezoelectric Polarization in III-V Nitride Solar Cells," University of Delaware, pp. 16-33, 2008.
- [67] "Numerical modelling" [Online]. Available: http://minewiki.engineering.queensu.ca/mediawiki/index.php/Numerical_modelling. [Accessed: 13-August-2017].
- [68] U. Gangopadhyay, S. Roy, S. Garain, S. Jana, and S. Das, "Comparative simulation study between n- type and p- type Silicon Solar Cells and the variation of efficiency of n- type Solar Cell by the application of passivation layer with different thickness using AFORS HET and PC1D," *IOSR J. Eng.*, vol. 2, no. 8, pp. 41–48, 2012.
- [69] A. G. Bhuiyan, K. Sugita, A. Hashimoto, and A. Yamamoto, "InGaN Solar Cells : Present State of the Art and Important Challenges," *IEEE J. Photovoltaics*, vol. 2, no. 3, pp. 276–293, 2012.
- [70] S.-W. Feng, C.-M. Lai, C.-Y. Tsai, Y.-R. Su, and L.-W. Tu, "Modeling of InGaN p-n junction solar cells," *Opt. Mater. Express*, vol. 3, no. 10, p. 1777-17788, 2013.
- [71] A. Mesrane, F. Rahmoune, A. Mahrane, and A. Oulebsir, "Design and simulation of InGaN p-n junction solar cell," *Int. J. Photoenergy*, vol. 2015, 2015.

Appendix A: Nextnano³ Input

The code for the p-n In_{0.6}Ga_{0.4}N solar cell is presented below as an example of all simulations have done in this thesis. Some modifications to the tutorial code, provided by Dr. Stefan Birner, were made to support this thesis.

```
!-----!
%ImportReflectivity      = no                      !
%FunctionParser          = yes                      !
%Thickness_Contacts     = 1                       !
%Thickness_pLayer       = 200                      !
%Thickness_nLayer       = 1000                     !
%pLayer_right_boundary  = %Thickness_pLayer        !
%nLayer_right_boundary  = %pLayer_right_boundary + %Thickness_nLayer !
%BackContact_right_boundary = %nLayer_right_boundary + %Thickness_Contacts!
%ptypeDoping_pLayer     = 1.0                      !
%ntypeDoping_nLayer     = 0.1                      !
%AlloyContent_pLayer    = 0.60d0                  !
%AlloyContent_nLayer    = 0.60d0                  !
%GridSpacing_pLayer     = 10.0                    !
%GridSpacing_nLayer     = 10.0                    !
%GridNodes_pLayer = (%pLayer_right_boundary / %GridSpacing_pLayer ) - 1 !
%GridNodes_nLayer
= ((%nLayer_right_boundary-%pLayer_right_boundary)/%GridSpacing_nLayer)-1 !
%INT(GridNodes_pLayer)  = %GridNodes_pLayer        !
%INT(GridNodes_nLayer)  = %GridNodes_nLayer        !
!-----!

!-----!
$numeric-control                      !
simulation-dimension                = 1              !
varshni-parameters-on              = yes            !
newton-method                       = Newton-1      !
current-poisson-method              = block-iterative !
current-problem                     = integrate-current !
current-problem-iterations          = 100           !
current-problem-residual            = 1d-11        !
current-block-relaxation-Fermi     = 0.1d0        !
$end_numeric-control                !
!-----!

!***** OVERALL SIMULATION PARAMETERS *****!

!-----!
$import-data-on-material-grid        !
source-directory                    = d:\           !
import-generation                    = no           !
filename-generation = read_in_generation_rateID.in !
$end_import-data-on-material-grid    !
!-----!
```

```

!-----!
!-----!
$optical-absorption
destination-directory      = optics/
import-absorption-spectrum = yes
file-absorption-spectrum  = "C:\Users\Desktop\Abs_In0.6GaN.dat"
import-reflectivity-spectrum = no
!file-reflectivity-spectrum = "C:\Users\Desktop\R_In0.2GaN.dat"
import-solar-spectrum      = yes
file-solar-spectrum       = "..\Syntax\Solar cell files\solar
spectra\ASTMG173_AM15G.dat" ! G = global
number-of-suns            = 1.0d0
calculate-black-body-spectrum = no
$send_optical-absorption
!-----!

!-----!
$simulation-dimension
dimension = 1
orientation = 0 0 1
$send_simulation-dimension
!-----!

!-----!
$global-parameters
lattice-temperature = 300d0 ! Kelvin
$send_global-parameters
!-----!

!-----!
$simulation-flow-control
flow-scheme = 4
raw-potential-in = no
strain-calculation = homogeneous-strain
$send_simulation-flow-control
!-----!

!-----!
$domain-coordinates
domain-type = 0 0 1
z-coordinates = -%Thickness_Contacts %BackContact_right_boundary
growth-coordinate-axis = 0 0 1
pseudomorphic-on = GaN
$send_domain-coordinates
!-----!
!***** END OVERALL SIMULATION PARAMETERS *****!
!***** REGIONS AND CLUSTERS *****!
!-----!

$regions
region-number = 1 base-geometry = line region-priority = 1
z-coordinates = -%Thickness_Contacts 0d0
region-number = 2 base-geometry = line region-priority = 1
z-coordinates = 0d0 %pLayer_right_boundary
region-number = 3 base-geometry = line region-priority = 1
z-coordinates = %pLayer_right_boundary %nLayer_right_boundary
region-number = 4 base-geometry = line region-priority = 1
z-coordinates = %nLayer_right_boundary %BackContact_right_boundary
$send_regions
!-----!

```

```

!-----!
!-----!
$grid-specification
grid-type      =      0 0 1
z-grid-lines   = -%Thickness_Contacts 0d0 %pLayer_right_boundary
%nLayer_right_boundary %BackContact_right_boundary!
z-nodes        =      1 %INT(GridNodes_pLayer) %INT(GridNodes_nLayer) 1 !
z-grid-factors =      1d0      1d0      1d0      1d0
$send_grid-specification
!-----!

!-----!
$region-cluster
cluster-number = 1      region-numbers = 1
cluster-number = 2      region-numbers = 2
cluster-number = 3      region-numbers = 3
cluster-number = 4      region-numbers = 4 5
$send_region-cluster
!-----!
!***** END REGIONS AND CLUSTER *****!
!-----!
!***** MATERIALS AND ALLOY PROFILES *****!
!-----!
$material
material-number = 1
material-name   = GaN
cluster-numbers = 1
material-number = 2
material-name   = In(x)Ga(1-x)N
cluster-numbers = 2
alloy-function  = constant
material-number = 3
material-name   = In(x)Ga(1-x)N
cluster-numbers = 3
alloy-function  = constant
material-number = 4
material-name   = GaN
cluster-numbers = 4
$send_material
!-----!

!-----!
$alloy-function
material-number = 2
function-name   = constant
xalloy          = %AlloyContent_pLayer
material-number = 3
function-name   = constant
xalloy          = %AlloyContent_nLayer
$send_alloy-function
!-----!
!-----!
! Here the database entries for InGaN.
!-----!
!-----!

```

```

!-----!
$ternary-wz-default
ternary-type = In(x)Ga(1-x)N-wz-default
binary(x) = InN-wz-default
binary(1-x) = GaN-wz-default
apply-to-material-numbers = 2 3
bow-band-gaps = 1.4d0 1.84d0 0.69d0 ! E_g
bow-conduction-band-energies = 1.4d0 1.84d0 0.69d0 ! E_g
$end_ternary-wz-default
!-----!

!-----!
$binary-wz-default
binary-type = GaN-wz-default
apply-to-material-numbers = 1 4
conduction-bands = 3
conduction-band-masses = 0.202d0 0.206d0 !
1.430d0 0.330d0 !
2.170d0 0.280d0 !
conduction-band-degeneracies = 2 8 6 !
conduction-band-nonparabolicities = 0.600d0 0.200d0 0.300d0 ! [1/eV]
band-gaps = 3.510d0 7d0 7d0 ! [eV]
conduction-band-energies = 2.79967d0 6.190d0 6.490d0 !
valence-bands = 3 !
valence-band-masses = 1.6d0 1.6d0 1.1d0 !
0.15d0 0.15d0 1.1d0 !
1.1d0 1.1d0 0.15d0 !
valence-band-degeneracies = 2 2 2 !
valence-band-nonparabolicities = 0.015d0 2.103d0 0.500d0 ! [1/eV]
valence-band-energies = -0.726d0 ! [eV]
varshni-parameters = 0.909d-3 0.00d0 0.00d0 !alpha [eV/K]
830d0 0.00d0 0.00d0 ! [K]
static-dielectric-constants = 9.28d0 10.0 !
optical-dielectric-constants = 5.29d0 !
band-shift = 0d0 !
absolute-deformation-potentials-cbs = -6.8d0 -6.8d0 -8.6d0 ! [eV]
uniax-vb-deformation-potentials = -3.7d0 4.5d0 8.2d0 !
-4.1d0 -4.0d0 -5.5d0 ! [eV]
lattice-constants = 0.3189d0 0.5185d0 ! [nm] 300 K
lattice-constants-temp-coeff = 0d0 ! [nm/K]
elastic-constants = 390d0 145d0 106d0 !
398d0 105d0 !
piezo-electric-constants = 1.27d0 -0.35d0 -0.30d0 ! [C/m^2]
pyro-polarization = 0d0 -0.034d0 ! [C/m^2]
6x6kp-parameters = -7.21d0 -0.44d0 6.68d0 !
-3.46d0 -3.40d0 -4.90d0 !
0.010d0 0.00567d0 !
8x8kp-parameters = -3.221d0 -0.44d0 2.691d0 !
-1.466d0 -1.406d0 -2.080d0 !
0.0937d0 !
14.0d0 !
0.866d0 0.962d0 ! S1,S2
LO-phonon-energy = 0.09212d0 0.09113d0 ! [eV]
number-of-minima-of-cband = 1 4 3 !
$end_binary-wz-default
!-----!

```

```

!-----!
$mobility-model-constant                                     !
material-name                                               = In (x) Ga (1-x) N      !
n-mu-lattice-temp                                           = 100d0                    !
[cm^2/Vs]                                                    !
n-gamma-lattice-temp                                       = 1.0d0                    !
[---]                                                        !
p-mu-lattice-temp                                           = 100d0                    !
[cm^2/Vs]                                                    !
p-gamma-lattice-temp                                       = 1.0d0                    !
[---]                                                        !
$end_mobility-model-constant                                 !
!-----!

!$SRH-recombination                                       !
! material-name                                             = In (x) Ga (1-x) N      !
! number-of-parameters                                     = 4                        !
! n-N-ref                                                 = 1.0d19                  ! cm^-3
! n-tau                                                    = 1.0d-9                  ! s
! p-N-ref                                                 = 1.0d18                  ! cm^-3
! p-tau                                                    = 1.0d-9                  ! s
!$end_SRH-recombination                                     !
!-----!

!$Auger-recombination                                       !
! material-name                                             = In (x) Ga (1-x) N      !
! number-of-parameters                                     = 2                        !
! n-C                                                      = 1.0d-31                 !
! p-C                                                      = 1.0d-31                 ! cm^6/s
!$end_Auger-recombination                                   !
!-----!

!$direct-recombination                                       !
material-name                                               = In (x) Ga (1-x) N      !
number-of-parameters                                       = 1                        !
radiative constant                                         = 1.1d-8 ! [cm^3/s]
C-opt                                                       = 1.1d-8 ! [cm^3/s]
!$end_direct-recombination                                 !
!-----!
!***** END MATERIALS AND ALLOY PROFILES *****!
!-----!
!***** DOPING AND IMPURITIES *****!
!-----!

$doping-function                                             !
doping-function-number   = 1                                     !
impurity-number          = 1                                     !
doping-concentration     = %ptypeDoping_pLayer                 !
only-region              = 0d0 %pLayer_right_boundary         !
doping-function-number   = 2                                     !
impurity-number          = 2                                     !
doping-concentration     = %ntypeDoping_nLayer                 !
only-region              = %pLayer_right_boundary %nLayer_right_boundary!
position                  = 150d0                               !
!$end_doping-function                                         !

```

```

!-----!
!-----!
$impurity-parameters
impurity-number          = 1
impurity-type            = p-type
number-of-energy-levels  = 1
energy-levels-relative  = 0.01507d0
degeneracy-of-energy-levels = 4
impurity-number          = 2
impurity-type            = n-type
number-of-energy-levels  = 1
energy-levels-relative  = 0.01507d0
degeneracy-of-energy-levels = 2
$end_impurity-parameters
!-----!
!***** END DOPING AND IMPURITIES *****!
!-----!
!***** CURRENT *****!
!-----!
$poisson-boundary-conditions
poisson-cluster-number  = 1
region-cluster-number   = 1
applied-voltage         = 0.0d0
boundary-condition-type  = ohmic
contact-control         = voltage
poisson-cluster-number  = 2
region-cluster-number   = 4
applied-voltage         = 0.0d0
boundary-condition-type  = ohmic
contact-control         = voltage
$end_poisson-boundary-conditions
!-----!
!***** CURRENT CLUSTERS AND MODELS *****!
!-----!
$current-cluster
cluster-number          = 1
region-numbers          = 1
deactivate-cluster      = no
$end_current-cluster
!-----!
!-----!
$current-models
model-number            = 1
transport-model-name    = simple-drift-model
cluster-numbers         = 1
$end_current-models
!-----!
!-----!
$simple-drift-models
model-number            = 1
mobility-model          = mobility-model-constant
current-model-numbers  = 1
direct-recombination   = yes
SRH-recombination      = yes

```

```

!-----!
! from 0.0 [V] to 3.0 [V] !
!-----!
step-size           = 0.05d0 !
forward bias
number-of-steps    = 60      !
data-out-every-nth-step = 1 !
$send_voltage-sweep !
!-----!

!***** END CURRENT CLUSTERS AND MODELS *****!
!***** END CURRENT *****!
!***** OUTPUT *****!

!-----!
$global-settings
output-directory   = <name_of_input_file> !
debug-level        = 0                    !
number-of-parallel-threads = 1          !
$send_global-settings !
!-----!

!-----!
$output-bandstructure
destination-directory = band_strucl/ !
conduction-band-numbers = 1          !
valence-band-numbers  = 1 2 3       !
potential              = yes         !
electric-field         = yes         !
$send_output-bandstructure !
!-----!

!-----!
$output-raw-data
destination-directory = raw_data/ !
potential             = yes        !
fermi-levels         = yes        !
kp-eigenstates       = no         !
$send_output-raw-data !
!-----!

$output-densities
destination-directory = densities1/ !
electrons             = yes        !
holes                 = yes        !
charge-density        = yes        !
intrinsic-density     = yes        !
ionized-dopant-density = yes       !
piezo-electricity     = yes        !
pyro-electricity      = yes        !
interface-density     = yes        !
effective-density-of-states-Nc-Nv = yes !
integrated-density    = yes        !
$send_output-densities !
!-----!

```

```

!-----!
$output-current-data
destination-directory      = current/
current                    = yes
fermi-levels              = yes
mobility-out              = yes
IV-curve-out              = yes
recombination              = yes
$end_output-current-data
!-----!

!-----!
$output-material
destination-directory      = material_parameters/
doping-concentration       = 1Ddoping_concentration.dat
$end_output-material
!-----!

!***** END OUTPUT *****!

```

Appendix B: Description of Research for Popular Publication

Title: Simulating III-Nitride Solar Cells

By: Malak Refaei

A step toward a higher efficiency and a lower cost solar cell was taken by Dr. Morgan Ware's group at the University of Arkansas through modeling and simulation III-nitride solar cells using Nextnano³. Malak Refaei, a graduate student in the Microelectronics-Photonics program, was selected by Dr. Ware to lead this research.

Why do we need to use simulation? What is the benefit of using simulation? Why do researchers waste their time doing the simulation? In order to answer these questions, let us begin with the meaning of simulation. So, simulation is basically using a software program to create a device in an ideal environment or even in the worst environment. Therefore, the simulation could help to answer our questions and to understand the device. It also could provide a solution for current experimental issues.

The use of the simulation programs for solar cell devices has significantly increased in order to understand the behavior and operation of materials and systems without having to fabricate a device. Reducing the cost and development time have become a general requirement to design and investigate solar cell devices out of the vast selection of materials and structures. Solar cell simulation programs assist in the general study of the optical and electronic behavior and exploring the impact of different parameters on the solar cell's performance.

The III-nitride semiconductor material systems can achieve ultra-high efficiency solar cells. This novel material system can cover almost the entire solar spectrum efficiently more than the current materials used for solar cells such as Si and GaAs. Using III-nitride materials for solar cell devices has been a focus of many current researchers. One feature of the InGaN materials is that it has higher absorption coefficient. Thus most of the light can be absorbed in a small

thickness of a device. However, it has been a challenge to create optimal nanostructure solar cells based on III-nitride materials. Thus, through simulation, we can design an optimal solar cell using the III-nitride material system with lower cost.

Nextnano³ is a simulation tool which has been developed for semiconductor nanodevices. It has been widely applied to nanostructures and has a vast and customizable database of materials. Nextnano³ can be used for modeling and simulate nanostructure solar cells based on III-nitride materials. This programming tool could provide an improvement in understanding and simulation of III-nitride solar cells.

Appendix C: Executive Summary of Newly Created Intellectual Property

The principles of the method used for the theoretical investigations presented in this thesis are well known and applied by many other groups for simulating semiconductor band-structures at the nanoscale. However, the theoretical investigation of simulating InGaN solar cells is quite unique and have been published only in this project. The finding of this research is that Nextnano³ software was demonstrated for solar cell simulation based on InGaN materials. The methods used for the theoretical investigations of solar cell devices are not new as they are of interest in many other fields. Although the finding of this research is original, there is no new intellectual property.

Appendix D: Potential Patent and Commercialization Aspects of listed Intellectual Property Items

D.1 Patentability of Intellectual Property (Could Each Item be Patented)

There is no any intellectual property for patent consideration because only existing licensed codes in the software were used. This research focuses on evaluating the current codes in Nextnano³ to be utilized for solar cell simulation based on InGaN materials.

D.2 Commercialization Prospects (Should Each Item Be Patented)

The method used in this research is not appropriate for a patent since it was already commercialized.

D.3 Possible Prior Disclosure of IP

There is no prior disclosure of IP in this work.

Appendix E: Broader Impact of Research

E.1 Applicability of Research Methods to Other Problems

The theoretical methods used in the thesis are used for various fields and devices in order to study the behavior and properties of different materials. In fact, proving the possibility of using Nextnano³ for solar cells assists in simulating more complex nanostructure solar cells and can be applied to engineering, materials science, physics, biology, and other fields. Also, the adjusted code might be extended to other solar cell materials such as InGaAs, InGaP, etc. However, it requires more investigation in order to be used for more complex nanostructure.

E.2 Impact of Research Results on U.S. and Global Society

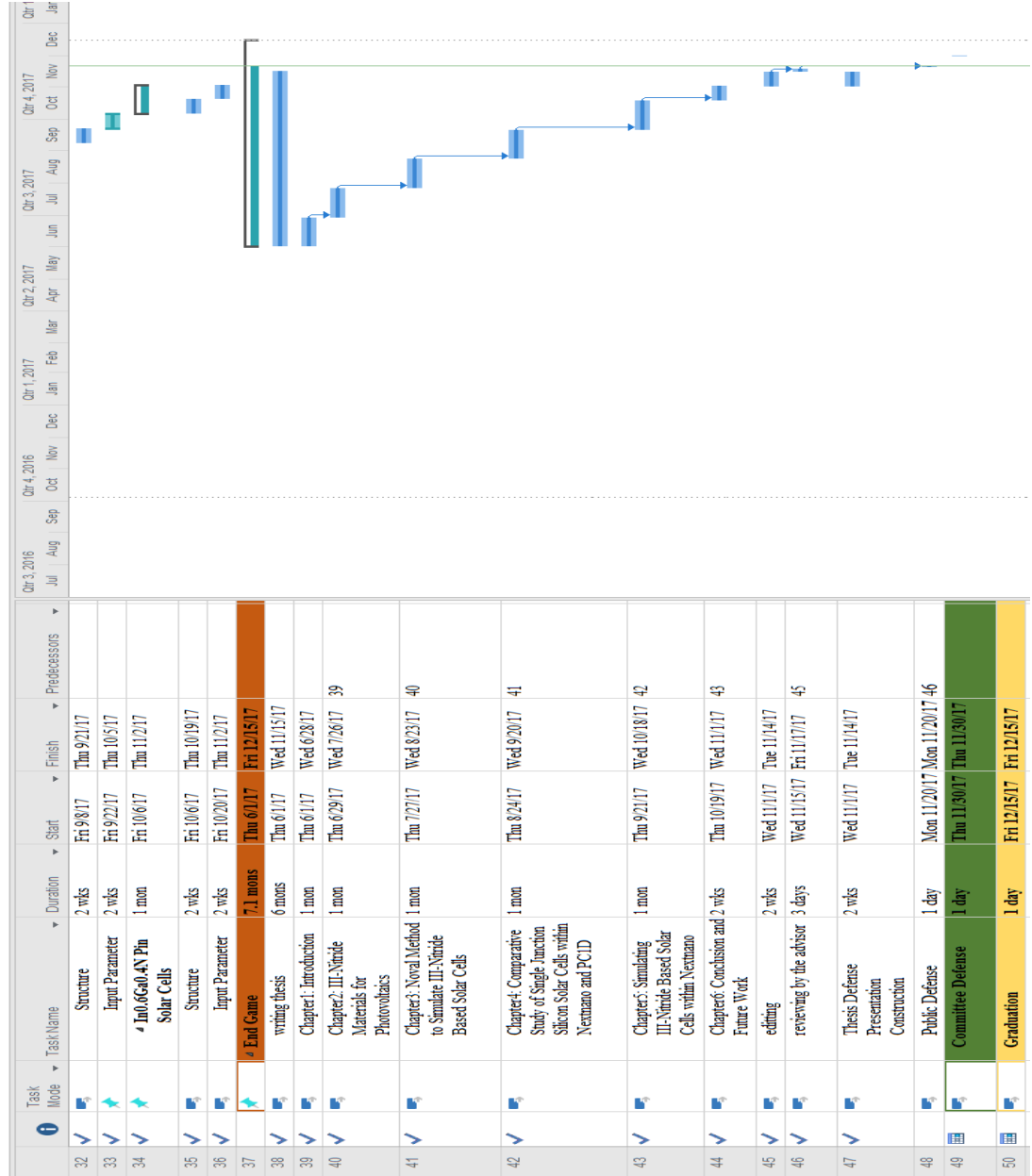
III-nitride solar cells have been considered as high-efficiency solar cells mainly due to its direct bandgap and high absorption coefficient. Nextnano³ can be used to simulate novel nanostructure solar cells based on III-nitride materials. The U.S. and the rest of the world can benefit from using Nextnano³ economically as well as environmentally. With the growing demand for energy along with the threat of global warming, the III-nitride solar cells, with higher absorption coefficient, would increase the possibility to have a sustainable source of energy using a small area.

E.3 Impact of Research Results on the Environment

This research proves that Nextnano3 can be used for solar cell simulation. This software can open the door for more research in solar cell nanostructures in order to design and model sufficient solar cells for the growing demand of energy without having any negative impact on the environment. Using solar cells simulation, Nextnano3 can assist in creating ultrahigh-efficiency solar cells in order to compete economically with current fossil fuels and thus reduce pollution.

Appendix F: Microsoft Project for MS MicroEP Degree Plan

Task Mode	TaskName	Duration	Start	Finish	Predecessors
1	Research group training	2 mons	Tue 8/2/16	Mon 9/26/16	
2	Nextnano	1 mon	Thu 8/4/16	Wed 8/31/16	
3	PCID	1 mon	Tue 8/30/16	Mon 9/26/16	
4	Literature Review	2 mons	Wed 10/5/16	Tue 11/29/16	
5	III-Nitride Materials for Photovoltaics	2 wks	Wed 10/5/16	Tue 10/18/16	
6	Basic Principles of Solar Cells	1 wk	Wed 10/5/16	Tue 10/11/16	
7	III-Nitride Materials System	1 wk	Wed 10/12/16	Tue 10/18/16	6
8	Novel Method to Simulate III-Nitride Based Solar Cells	2 wks	Wed 10/19/16	Tue 11/1/16	
9	Solving The Software Equations	1 wk	Wed 10/19/16	Tue 10/25/16	
10	Program Flow	1 wk	Tue 10/25/16	Mon 10/31/16	
11	Parameters of Nextnano	1 wk	Tue 10/25/16	Mon 10/31/16	
12	Comparative Study of Single Junction Silicon Solar Cells within Nextnano and PCID	1 mon	Tue 11/1/16	Mon 11/28/16	
13	PCID Simulation Tool	2 wks	Tue 11/1/16	Mon 11/14/16	
14	Differences between Nextnano and PCID	2 wks	Tue 11/15/16	Mon 11/28/16	13
15	PCID Simulation	4 mons	Mon 1/2/17	Fri 4/21/17	
16	Literature Review	1 mon	Mon 1/2/17	Fri 1/27/17	
17	Simulating of Single Junction Silicon Solar Cells	3 mons	Mon 1/30/17	Fri 4/21/17	
18	Silicon Solar Cell Structure	1 mon	Mon 1/30/17	Fri 2/24/17	
19	Input Parameter	1 mon	Mon 2/27/17	Fri 3/24/17	
20	Calculation of Si Solar Cell	1 mon	Mon 3/27/17	Fri 4/21/17	



Appendix G: Identification of All Software Used in Research and Thesis Generation

Computer #1:

Model Number: SVF14AC1QL

Serial Number: 4-465-345-31

Location: 1602 N Merion Way

Owner: Malak Refaei

Software #2:

Name: Nextnano software

license Key: 2B4CAE39A

Purchased by: Dr. Morgan Ware

Software #3:

Name: Microsoft Office 2013

Purchased by: Malak Refaei

Software #4:

Name: Microsoft Project 2010

Purchased by: MSDN Academy Alliance through Engineering

Software #5:

Name: Origin 2018

Purchased by: Malak Refaei

Appendix H: All Publications Published, Submitted, and Planned

There are no publications published or submitted for this work.